

NEUTRON DIFFRACTION STUDIES ON ABO_3 (A=La, Sr, B=Fe, Co, Ni,
Cu, Mn, Ti) PEROVSKITE USED IN SOLID OXIDE FUEL CELL (SOFC)
AND DOUBLE PEROVSKITE $\text{Ba}_2\text{YRu}_{0.85}\text{Cu}_{0.15}\text{O}_6$ SUPERCONDUCTOR

A Dissertation

presented to

the Faculty of the Graduate School

at the University of Missouri-Columbia

In Partial Fulfillment

of the Requirements for the Degree

Doctor of Philosophy

by

QINGSHENG CAI

Dr. William B. Yelon, Dissertation Supervisor

May. 2009

The undersigned, appointed by the dean of the Graduate School, have examined the
dissertation entitled

NEUTRON DIFFRACTION STUDIES ON ABO_3 (A=La, Sr, B=Fe, Co, Ni,
Cu, Mn, Ti) PEROVSKITE USED IN SOLID OXIDE FUEL CELL (SOFC)
AND DOUBLE PEROVSKITE $\text{Ba}_2\text{YRu}_{0.85}\text{Cu}_{0.15}\text{O}_6$ SUPERCONDUCTOR

Presented by Qingsheng Cai,

a candidate for the degree of Doctor of Philosophy of Physics

and hereby certify that, in their opinion, it is worthy of acceptance.

Professor William B. Yelon

Professor Stephen J. Lombardo

Professor Sashi Satpathy

Professor Wouter Montfrooij

Professor William J. James

ACKNOWLEDGMENTS

I would like to express my appreciation to all my committee members for their time and helpful comments. I am particularly grateful to my advisor, Dr. Yelon, for his support and guidance in helping my Ph.D. degree completion. I would like to thank Prof. William James, Prof. Harlan Anderson, Dr. Jinbo Yang, and Dr. XiaoDong Zhou, at Materials Research Center of Missouri University of Science and Technology, and Dr. Blackstead at University of Notre Dame, for their assistance in sample preparation and many helpful discussions. I would also like to thank Dr. Kaiser and Dr. Farmer for their support in MURR.

I am very glad I have many friendly and clever colleagues in our neutron diffraction group: Mingxin Chen, Zili Chu, Jagat Lamsal, and Mehmet Kahveci. I am especially appreciated to Mingxin Chen for his help at the beginning of my research. I wish to thank my friends and colleagues of the Department of Physics at University of Missouri-Columbia.

TABLE OF CONTENT

ACKNOWLEDGEMENTS.....	ii
LIST OF ILLUSTRATIONS.....	vi
LIST OF TABLES.....	x
ABSTRACT	xiii
Chapter 1 INTRODUCTION.....	1
Chapter 2 STRUCTURE OF SIMPLE AND DOUBLE PEROVSKITES.....	7
2.1 THE STRUCTURE OF SIMPLE PEROVSKITE ABO_3	7
2.2 THE STRUCTURE OF DOUBLE PEROVSKITE $A_2BB'O_6$	13
Chapter 3 THE PRINCIPLES OF SOFC AND NEUTRON SCATTERING.....	17
3.1 THE PRINCIPLE OF SOFCs	17
3.2 NEUTRON SCATTERING	20
3.3 RIETVELD METHOD	29
3.4 MURR PSD DIFFRACTOMETER	33
Chapter 4 NEUTRON DIFFRACTION STUDIES ON $ABO_{3-\delta}$ (A=La, Sr; B=Fe, Co, Ni, Cu, Ti, Mn) PEROVSKITE MATERIALS USED IN SOFCs	42
4.1 $La_{1-x}Fe_xO_{3-\delta}$ (x=0.2 AND 0.4)	42
4.1.1 INTRODUCTION	42
4.1.2 EXPERIMENTAL.....	44
4.1.3 RESULTS AND DISCUSSION	45
a) $La_{0.6}Sr_{0.4}FeO_{3-\delta}$ (L6SF)	45
b) $La_{0.8}Sr_{0.2}FeO_{3-\delta}$ (L8SF)	63

4.1.4 CONCLUSIONS	70
4.2 $\text{LaFe}_{1-x}\text{M}_x\text{O}_3$ (M=Ni, Mn, AND Cu)	71
4.2.1 INTRODUCTION	71
4.2.2 EXPERIMENTAL	71
4.2.3 RESULTS AND DISCUSSION	72
a) $\text{LaFe}_{1-x}\text{Ni}_x\text{O}_3$ (x=0, 0.2, 0.4, 0.5, 0.8)	72
b) $\text{LaFe}_{1-x}\text{Mn}_x\text{O}_3$	82
c) $\text{LaFe}_{1-x}\text{Cu}_x\text{O}_3$ (x≤0.5)	89
4.2.4 CONCLUSIONS	97
4.3 $\text{La}_{1-x}\text{Sr}_x\text{Fe}_y\text{Co}_{1-y}\text{O}_{3-\delta}$ (LSCF) AND $\text{La}_{0.2}\text{Sr}_{0.8}\text{Fe}_{0.55}\text{Ti}_{0.45}\text{O}_3$ (LSFT)	98
4.3.1 INTRODUCTION	98
4.3.2 EXPERIMENTAL	99
4.3.3 RESULTS AND DISCUSSION	100
a) $\text{La}_{0.6}\text{Sr}_{0.4}\text{Fe}_{0.8}\text{Co}_{0.2}\text{O}_3$ (L6SFC)	100
b) $\text{La}_{0.8}\text{Sr}_{0.2}\text{Fe}_{0.8}\text{Co}_{0.2}\text{O}_3$ (L8SFC)	103
c) $\text{La}_{0.2}\text{Sr}_{0.8}\text{Fe}_{0.55}\text{Ti}_{0.45}\text{O}_3$ (LSFT)	104
4.3.4 CONCLUSIONS	112
Chapter 5 NEUTRON DIFFRACTION STUDY OF THE DOUBLE PEROVSKITE	
$\text{Ba}_2\text{YRu}_{0.85}\text{Cu}_{0.15}\text{O}_6$ SUPERCONDUCTOR	113
5.1 INTRODUCTION	113
5.2 EXPERIMENTAL	115
5.3 RESULTS AND DISCUSSION	116
a) $\text{Ba}_2\text{YRu}_{0.85}\text{Cu}_{0.15}\text{O}_6$	116

b) $\text{Ba}_2\text{YRuO}_6 + 5 \text{ wt\% Y123}$	124
5.4 CONCLUSIONS	126
Chapter 6 SUMMARY	127
REFERENCES	131
VITA	138

LIST OF ILLUSTRATIONS

Figure	Page
2.1: The ideal perovskite structure with the B atom at the body center (a) or the A atom at the body center (b).....	8
2.2: The results of the tilt with the c axis only.....	10
2.3: Schematic diagram illustrating all the possible senses of tilts. Each set of three symbols refers to one octahedron.....	12
3.1: The operating principle of a solid oxide fuel cell.....	18
3.2: Planar (a) and Tubular (b) design of solid oxide fuel cells.....	19
3.3: A neutron scattered by a single fixed nucleus.....	22
3.4: Debye-Scherrer cone for Bragg scattering from a powder.....	25
3.5a: The MURR PSD Double Focusing Powder Diffractometer	36
3.5b: Conventional Constant Wavelength Diffractometer.....	37
3.6: Position sensitive proportional counters.....	38
3.7: Schematic diagram of the neutron diffraction furnace.....	41
4.1: Neutron diffraction pattern for L6SF refined with model 1 and model 3. The red dots are the observed intensity, the black line is the calculated intensity, and the blue curve is the difference between the observed and the calculated intensity.....	47
4.2: The neutron diffraction patterns of L6SF for unquenched, 900°C, 1100°C, 1200°C, and 1500°C quenched specimens. The black dots are the observed intensity, the solid red line is the calculated intensity, and their difference (green) is under them. The upper tic marks show Bragg positions for the nuclear phase, and the lower ones are for the magnetic phase.....	48
4.3: Lattice parameters of L6SF vs. quenching condition.....	50
4.4: The changes of oxygen vacancy concentration, magnetic moment, and unit cell volume with the quench temperature for the L6SF samples.	52

4.5: Magnetic moment and unit cell volume at room temperature vs. oxygen vacancy concentration for L6SF.	53
4.6: Oxygen vacancy concentration vs. saturation moment for L6SF	54
4.7: The neutron diffraction profile of L6SF 1500°C air quenched sample heated at 394°C without air filling.....	58
4.8: Temperature variation of lattice parameters a and c of the L6SF slowly cooled and 1500°C quenched samples.....	58
4.9: The unit cell volume of L6SF samples quenched from 1500°C and slowly cooled at high temperature with/without air flowing.....	60
4.10: The neutron diffraction pattern at room temperature of L8SF sample quenched from 800°C.....	64
4.11: The neutron diffraction patterns of L8SF at 190°C, 292°C, and 394°C. The magnetic ordering disappears at 292°C, and the structural phase transition occurs below 394°C.....	66
4.12: Lattice parameters of L8SF vs. temperature	68
4.13: The unit cell volume per formula unit of L8SF, as a function of temperature.....	69
4.14: The neutron diffraction patterns of $\text{LaFe}_{1-x}\text{Ni}_x\text{O}_3$ at room temperature.....	73
4.15: Dependence of lattice parameters with composition for $\text{LaFe}_{1-x}\text{Ni}_x\text{O}_3$. For the orthorhombic phase, $a_o = a/\sqrt{2}$, $b_o = b/\sqrt{2}$, and $c_o = c/2$; for the rhombohedral phase, $a_R = a/\sqrt{2}$, and $c_R = c/2\sqrt{3}$	76
4.16: Dependence of the unit cell volume per formula unit with composition, for $\text{LaFe}_{1-x}\text{Ni}_x\text{O}_3$	77
4.17: The average magnetic moment at B sites vs. Ni content for the $\text{LaFe}_{1-x}\text{Ni}_x\text{O}_3$ series.....	78
4.18: The neutron diffraction patterns of $\text{LaFe}_{0.4}\text{Ni}_{0.6}\text{O}_3$ samples sintered at 1100°C and 1400°C. The peaks indicated by the arrows are the NiO peaks.....	81
4.19: The oxygen stoichiometry deviation and unit cell volume in $\text{LaFe}_{0.4}\text{Ni}_{0.6}\text{O}_3$ vs. sintering temperature.	82

4.20:	Four typical neutron diffraction patterns from the $\text{LaFe}_{1-x}\text{Mn}_x\text{O}_3$ series, at room temperature.....	84
4.21:	Total oxygen as a function of Mn content in $\text{LaFe}_{1-x}\text{Mn}_x\text{O}_3$	86
4.22:	The unit volume per formula of $\text{LaFe}_{1-x}\text{Mn}_x\text{O}_{3+\delta}$ vs. Mn content.....	87
4.23:	The magnetic moments at B sites at room temperature and 16K as a function of Mn fraction in $\text{LaFe}_{1-x}\text{Mn}_x\text{O}_3$	89
4.24:	Three typical neutron diffraction patterns for the $\text{LaFe}_{1-x}\text{Cu}_x\text{O}_3$ ($x=0.01, 0.3, 0.5$) series.....	91
4.25:	The unit cell volume of $\text{LaFe}_{1-x}\text{Cu}_x\text{O}_3$ ($x \leq 0.3$) vs. Cu content.....	93
4.26:	The magnetic moment of $\text{LaFe}_{1-x}\text{Cu}_x\text{O}_3$ at room temperature and 16K vs. Cu content.....	94
4.27:	The neutron diffraction patterns of $\text{LaFe}_{0.9}\text{Cu}_{0.1}\text{O}_3$ at high temperature.....	95
4.28:	The root of the intensity of the magnetic peak (\sqrt{I}) in $\text{LaFe}_{0.9}\text{Cu}_{0.1}\text{O}_3$ vs. temperature.....	96
4.29:	Lattice parameter a^* and c^* of L6SF8C vs. the quenching temperature.	101
4.30:	The oxygen vacancies, magnetic moment, and unit cell volume of L6SF8C vs. the quenching temperature.....	102
4.31:	Neutron data for the 1200°C slowly cooled LSFT sample fitted by the cubic (a) and rhombohedral (b) structure. For the cubic model, a number of small peaks indicated by arrows are not fitted. For the rhombohedral model, all peaks are fitted well.....	105
4.32:	The oxygen vacancy and the unit cell volume per formula as a function of the LSFT sample treatment conditions.....	107
4.33:	The oxygen occupancy and lattice parameter a of LSFT vs. temperature with air filling.....	111
4.34:	The oxygen occupancy and lattice parameter a of LSFT vs. temperature with N_2 filling.....	111
5.1:	The neutron diffraction profiles of $\text{Ba}_2\text{YRu}_{0.85}\text{Cu}_{0.15}\text{O}_6$ at a), room temperature and b), 16K.....	118

5.2:	a) Crystal structure of $\text{Ba}_2\text{YRu}_{0.85}\text{Cu}_{0.15}\text{O}_6$; b) Magnetic structure of $\text{Ba}_2\text{YRu}_{0.85}\text{Cu}_{0.15}\text{O}_6$	119
5.3:	Low angle neutron diffraction data for $\text{Ba}_2\text{YRu}_{0.85}\text{Cu}_{0.15}\text{O}_6$ as a function of temperature from 16K to 95K.....	123
5.4:	Comparison of neutron diffraction profiles of the $\text{Ba}_2\text{YRu}_{0.85}\text{Cu}_{0.15}\text{O}_6$ sample and the empty holder.....	123
5.5:	The neutron diffraction profiles of the mixture of Ba_2YRuO_6 and 5% by weight of Y123 at different heat treatment steps.....	125

LIST OF TABLES

Table	Page
2.1: the 10 distinct possible tilts.....	9
2.2: complete list of possible simple tilt systems.....	14
2.3: Space group for all possible simple tilt systems both with and without 1:1 cation ordering. The space group (no ordering) of system (5), (7), (17), and (18) are different than the ones in table 2.2, since there are slight distortions of the octahedra in order to retain the connectivity of the octahedra.....	16
4.1: The goodness-of-fit (χ^2) of the 10 quenched and unquenched specimens fitted with the three models.....	47
4.2: L6SF refinement with constraints: fraction of O1 ≤ 0.5 . The fraction of O2 is the same as O3, and the sum of fractions of O2 and O3 ≤ 1.0 . Uncertainties in parenthesis are on the least significant digits.....	49
4.3: The magnetic moment of L6SF at different quenching temperature. The mol% of Fe ³⁺ is calculated from the oxygen vacancy concentration.....	55
4.4: L6SF sample quenched in air from 1500°C, measured as a function of temperature and without air filling. The RT ⁽¹⁾ is a measurement at room temperature before the sample was heated, and the RT ⁽²⁾ is the measurement after the sample was slowly cooled to room temperature. The measurements at room temperature were run with the specimen outside the furnace.....	61
4.5: L6SF sample quenched in air from 1500°C, measured as a function of temperature and with air filling. The RT is the measurement outside the furnace after the sample was slowly cooled to room temperature.	62
4.6: L6SF slowly cooled sample measured as a function of temperature. The room temperature measurement is outside the furnace.	62
4.7: Refinement results for L8SF samples quenched in air from 800°C to 1500°C. The A and B sites are fully occupied, and the ratio of La/Sr is fixed as 0.8/0.2.....	64
4.8: Refinement results for L8SF at high temperature with air filling.....	67

4.9: Tolerance factor t for $\text{LaFe}_{1-x}\text{Ni}_x\text{O}_3$	74
4.10: The results obtained from the Rietveld refinement of the neutron diffraction data of $\text{LaFe}_{1-x}\text{Ni}_x\text{O}_{3+\delta}$ at room temperature. The A and B sites are fully occupied and the ratio of Fe/Ni is fixed at the synthesis ratio.....	75
4.11: The results obtained from the Rietveld refinement of the neutron diffraction data of $\text{LaFe}_{0.4}\text{Ni}_{0.6}\text{O}_{3-\delta}$ at room temperature. The A site and B sites are fully occupied and the ratio of Fe/Ni is fixed as 0.4/0.6 if there is no second phase.....	80
4.12: Refinements result for $\text{LaFe}_{1-x}\text{Mn}_x\text{O}_3$ at room temperature.....	83
4.13: The tolerance factor t for $\text{LaFe}_{1-x}\text{Mn}_x\text{O}_{3+\delta}$	86
4.14: The tolerance factor t of $\text{LaFe}_{1-x}\text{Cu}_x\text{O}_3$ ($x \leq 0.5$).....	90
4.15: Refinement results for $\text{LaFe}_{1-x}\text{Cu}_x\text{O}_3$. All samples are orthorhombic structure with space group Pbnm.....	92
4.16: The intensity of the magnetic peak (1 0 1) at different temperatures.....	96
4.17: L6SF8C refinement with constraints: fraction of O1 ≤ 0.5 . Fraction of O2 is same as O3, and the sum of the fractions of O2 and O3 ≤ 1.0	100
4.18: Refinement results for L8SF8C quenched samples. Space group is $R\bar{3}c$, and oxygen is at 18e sites.....	104
4.19: Refinement results for LSFT ($\text{La}_{0.2}\text{Sr}_{0.8}\text{Fe}_{0.55}\text{Ti}_{0.45}\text{O}_3$) samples measured at room temperature. The space group is $R\bar{3}c$ for the unquenched and 1200°C slowly cooled samples, and the space group is $\text{Pm}\bar{3}m$ for the quenched samples. The Fe and Ti ions occupy the 6b sites (in the $R\bar{3}c$ space group) or the 1b sites (in the $\text{Pm}\bar{3}m$ space group) randomly; the ratios of La/Sr and of Fe/Ti are fixed as 0.2/0.8 and 0.55/0.45 respectively.....	106
4.20: Refinement results for LSFT 1400°C bar sample at high temperature with air filling. Sample is cubic structure with space group $\text{Pm}\bar{3}m$, La/Sr is at 1a site, Fe/Ti is at 1b site, and O is at 3d sites. The ratio of La/Sr is fixed as 0.2/0.8, and the ratio of Fe/Ti is fixed as 0.55/0.45. The anisotropic thermal parameters are constrained as $b_{22}=b_{33}$, and $b_{12}=b_{13}=b_{23}=0$. b_{11} and b_{22} are timed by 10^4	109

4.21: Refinement results for LSFT 1400°C bar sample at high temperature with N ₂ filling. Sample is cubic structure with space group $Pm\bar{3}m$, La/Sr is at 1a site, Fe/Ti is at 1b site, and O is at 3d sites. The ratio of La/Sr is fixed as 0.2/0.8, and the ratio of Fe/Ti is fixed as 0.55/0.45. The anisotropic thermal parameters are constrained as $b_{22}=b_{33}$, and $b_{12}=b_{13}=b_{23}=0$. b_{11} and b_{22} are fixed by 10^4	109
5.1: Structural parameters of Ba ₂ YRu _{0.85} Cu _{0.15} O ₆ at room temperature. The unit cell is cubic with lattice parameter $a=8.32859(16)$ Å, and the space group is $Fm\bar{3}m$	119
6.1: The properties of perovskite candidates used in SOFCs. σ is the conductivity, δ is the oxygen vacancy concentration, and TEC is the thermal expansion coefficient.....	128

NEUTRON DIFFRACTION STUDIES ON ABO_3 (A=La, Sr, B=Fe, Co, Ni, Cu, Mn, Ti) PEROVSKITE USED IN SOLID OXIDE FUEL CELL (SOFC) AND DOUBLE PEROVSKITE $Ba_2YRu_{0.85}Cu_{0.15}O_6$ SUPERCONDUCTOR

Qingsheng Cai

Dr. William B. Yelon, Dissertation Supervisor

ABSTRACT

ABO_3 (A=La, Sr, B=Fe, Co, Ni, Cu, Mn, Ti) perovskites are of great interest due to their mixed electronic and oxygen ion conductivity. They are candidates for the electrodes of SOFCs. The mixed conductivity can be enhanced through the substitution of La^{3+} by Sr^{2+} at A sites, and the substitution of Fe^{3+} by other transition metal ions at B sites. The charge imbalance and overall charge neutrality can be maintained by the presence of charged oxygen vacancies and mixed valence state ions at the B sites. These point defects are the origin of the mixed electronic and oxygen ion conductivity. This study investigates the effects of substitutions at A sites and/or B sites on the crystal and magnetic structure, oxygen vacancies, and the thermal expansion coefficients at different temperatures and gaseous environment. The oxygen vacancy concentration can relax the perovskite distortion and has a close relationship with the magnetic properties.

$La_{0.6}Sr_{0.4}FeO_{3-\delta}$, $La_{0.6}Sr_{0.4}Fe_{0.8}Co_{0.2}O_{3-\delta}$, and $La_{0.8}Sr_{0.2}Fe_{0.8}Co_{0.2}O_{3-\delta}$ can be good candidates for the cathodes of SOFCs at intermediate temperature.

The double perovskite $Ba_2YRu_{0.85}Cu_{0.15}O_6$ superconductor and a mixture of 5wt% $YBa_2Cu_3O_{7-\delta}$ and undoped Ba_2YRuO_6 were investigated with the aid of neutron

diffraction. The 1:1 B site ordering is observed and long range antiferromagnetic ordering of the Ru sublattice with a type I magnetic structure appears when the temperature is below 38K. An incommensurate antiferromagnetic ordering of Cu is observed in the temperature range 38K-85K. This ordering is not seen in undoped material. The decomposition of Cu-doped Ba_2YRuO_6 into undoped Ba_2YRuO_6 and $\text{YBa}_2\text{Cu}_3\text{O}_{7-\delta}$ is not seen. $\text{YBa}_2\text{Cu}_3\text{O}_{7-\delta}$ is not stable at the temperature used to prepare the Cu-doped Ba_2YRuO_6 superconductor. These results confirm the presence of superconductivity without CuO_2 planes.

Chapter 1 INTRODUCTION

This work focuses on the structures, determined by neutron diffraction, of two classes of materials based on the perovskite structure. The first class contains materials being considered for application to Solid Oxide Fuel Cells (SOFC) and oxygen transport membranes. The second class contains a new family of high T_c superconductors (HTSC) based on the cubic double perovskite structure, without CuO_2 planes.

The ABO_3 perovskite encompasses a large variety of compounds. Most of the metallic ions in the periodic table can be incorporated into the perovskite structure; the large cation A can be an alkali, alkaline earth, or rare earth ion, and the small B cation can typically be a transition metal ion. Since a wide variety of ions can be accommodated in the perovskite structure, perovskite compounds have a lot of important and interesting physical properties; such as ferroelectricity, dielectric, magnetoresistive, ionic and electronic conductivity.

A three-dimensional framework made up of BO_6 octahedra characterizes the ABO_3 perovskite crystal structure. The interstices of this framework are sites for the large A cations, and the small B cations are at the centers of the octahedra. Every two neighboring BO_6 octahedra share a common O atom. The perovskite structure is often stable with both divalent (Sr, Ba, Ca, etc.) and trivalent (e.g. lanthanide) A site occupation, and the charge imbalance and overall charge neutrality will be maintained by the formation of electrons, holes and/or charged oxygen vacancies. These point defects can take part in the electronic and/or oxygen ion conductivity, and this gives the material scientist an opportunity to alter the transport properties of a given oxide.

When perovskite materials that contain transition metal ions at the B sites are heated to sufficiently high temperature, they can equilibrate with the ambient oxygen by oxygen exchange. If the oxygen activities at the two sides of the perovskite are different, the oxygen ions can be transported from the high oxygen activity side to the low one. Therefore perovskites can be used as oxygen separation membranes or electrodes of SOFCs.

Strontium-doped lanthanum manganate is most commonly used as the cathode of SOFCs operated at high temperature. LaMnO_3 is a p-type perovskite. At high temperature, it can have oxygen excess, stoichiometry, or oxygen deficiency, depending on the oxygen partial pressure.⁽¹⁻³⁾ For example, at 1200°C, the oxygen content of LaMnO_3 ranges from 3.079 to 2.947 under oxygen partial pressures of 1 to $10^{-11.6}$ atmospheres.⁽¹⁾ In addition to oxygen nonstoichiometry, LaMnO_3 can also have La deficiency or excess. LaMnO_3 with La excess may contain La_2O_3 as a second phase, and therefore LaMnO_3 with La deficiency is recommended for use in SOFCs.

The electrical conductivity of LaMnO_3 can be increased by substituting lower-valence ions on the A sites. Strontium-doped LaMnO_3 is currently the preferred cathode material in SOFCs because of its high electronic conductivity in oxidizing atmospheres.⁽⁴⁾ Strontium doping enhances the electronic conductivity of LaMnO_3 by increasing the Mn^{4+} content by the substitution of La^{3+} by Sr^{2+} .⁽⁵⁾

The thermal expansion coefficient (TEC) of LaMnO_3 is $11.2 \times 10^{-6}/^\circ\text{C}$;⁽⁶⁾ doping LaMnO_3 with Sr increases its thermal expansion coefficient.⁽⁶⁻⁷⁾ For example, the TEC of $\text{La}_{0.79}\text{Sr}_{0.2}\text{MnO}_3$ is $12.4 \times 10^{-6}/^\circ\text{C}$, and the TEC of 10 mol% YSZ (10% $\text{Y}_2\text{O}_3/\text{ZrO}_2$), which is used as the solid electrolyte of SOFCs, is about $10 \times 10^{-6}/^\circ\text{C}$.⁽⁸⁾ Thus, the TECs of Sr-

doped LaMnO_3 (LSM) cathodes are higher than that of the YSZ electrolyte. There may be cracking problems due to this mismatch.

The chemical compatibility of the LaMnO_3 cathode with the YSZ electrolyte is another concern in the fabrication and operation of the SOFC. Manganese is known to be a mobile species at high temperature and can easily diffuse into the electrolyte. The reaction between LaMnO_3 and YSZ has been studied at SOFC operating and fabrication temperatures.⁽⁹⁾ There is no significant reaction between LaMnO_3 and ZrO_2 at temperatures below 1200°C . Above 1200°C , the LaMnO_3 reacts with ZrO_2 to produce $\text{La}_2\text{Zr}_2\text{O}_7$.⁽¹⁰⁾ For the high Sr-doped manganate ($x \geq 0.3$), SrZrO_3 is the reaction product.⁽¹¹⁾

The SOFCs which use LSM as the cathode, YSZ as the electrolyte, Ni+YSZ as the anode, and Sr-doped lanthanum chromate as the interconnect operate successfully in the $900\text{--}1000^\circ\text{C}$ range. A 100 kw tubular SOFC, built by Siemens-Westinghouse, operated very successfully in the Netherlands for a period of two years without any measurable performance degradation,⁽¹²⁾ but high cost has curtailed its commercialization. In recent years, work has focused on SOFCs that can operate at an intermediate temperature (IT) range ($600\text{--}800^\circ\text{C}$). In this temperature range, the metal alloy, such as stainless steel, which is cheap and easily fabricated, can be used as the interconnect, and the reliability of SOFCs is thus improved. The goals of the Solid State Energy Conversion Alliance (SECA) program are to lower the operating temperatures into the $600\text{--}800^\circ\text{C}$ range and to deliver electrical energy at $\$400/\text{kw}$ or lower before the year 2010.⁽¹³⁾

In order for a SOFC to be operated in the IT range, the electrode kinetics have to be at least as fast as those occurring at high temperature. LSM, the current cathode material,

is not suitable for use below 800°C due to its very low oxygen vacancy concentration.

Therefore, research has to be done to find new materials for use as the cathode of SOFCs operating in the IT range.

In general, most cathodes have relied on the B-site cation, and doping on both A-sites and B-sites to improve electrical conductivity and catalytic performance. One approach to finding a new cathode material is to replace the Mn by other transition metals, such as Fe, Co, and Ni etc..

The B-site ordering can occur if the B-B' ions are sufficiently different in size and/or valence, but their average radius should be compatible with perovskite formation for a given A-site ion. The new structure is called a “double” perovskite with the formula $A_2BB'O_6$. This provides more flexibility in adjusting the physical properties of the perovskites.

In 1997, M. K. Wu et al reported the discovery of a new class of high temperature superconductors with the double perovskite formula $AE_2Y(Ru_{1-x}Cu_x)O_6$ ($0.05 < x < 0.2$), where AE is an alkaline earth, either Ba or Sr. ⁽¹⁴⁻¹⁵⁾ The superconductivity onset temperature T_c is around 30K for Sr samples and 85K for Ba samples. However, these samples contain all of the necessary elements to form $YBa_2Cu_3O_{7-\delta}$ or $YSr_2Cu_3O_{7-\delta}$ (Y123 phases), and these possible superconducting impurities could, hypothetically, be the origin of the observed superconductivity in these samples. So Wu's discovery was dismissed. In 2000, H. A. Blackstead confirmed the superconductivity in $Sr_2Y(Ru_{1-x}Cu_x)O_6$ ($x=0.1$), ⁽¹⁶⁾ and he found that the possible impurity phase Y123 couldn't account for the observed superconductivity. First, the maximum Y123 phase content would be 3.33 mole% only if all the Cu were incorporated in the Y123 phase, and

this content is much lower than that required for bulk percolation (about 16%). Second, the samples were sintered at 1390 °C in O₂ (for the Sr samples) or 1450 °C in a mixture of 30% Ar and 70% O₂ (for the Ba samples). At such high temperatures, the Y123 phase, if present, would have decomposed. The following slow cooling might lead to the formation of some Y123, but this is quite unlikely. H.A. Blackstead treated a batch of Y123 using the same procedure for the preparation of the O6 sample, and the XRD data showed no characteristic lines of the Y123 phase. If a small amount of Y123 survived the extreme high temperature involved in the synthesis and “coated” the O6 grains to exhibit bulk superconductivity, then the same should be true for Ba₂GdRu_{1-x}Cu_xO₆, which should be superconducting if the O6 grains were “coated” by the Gd123 superconductor. However, the Ba₂GdRu_{1-x}Cu_xO₆ sample is not a superconductor.⁽¹⁷⁾

The parent compounds of the double perovskite superconductors are antiferromagnetic insulators, the same as the high temperature superconducting cuprates. But the double perovskite superconductors are quite different from the cuprate superconductors. First, there are only two kinds of layers in the double perovskite structure, the SrO or BaO plane and the Y(Ru, Cu)O₄ plane. The content of Cu is small, and the Cu ion is far too small to substitute for Y, so, there are no CuO₂ planes in the double perovskite structure. The CuO₂ plane is the common plane in all cuprate superconductors, and it is widely believed that the Cooper pairs are located in these planes. Second, the Y(Ru, Cu)O₄ planes have been found by neutron scattering to be ferromagnetically aligned in-plane, with antiferromagnetic stacking of adjacent planes, and this magnetic ordering coexists with the superconducting ordering. The coexistence of magnetism and superconductivity in O6 is quite surprising since magnetic ordering in

the CuO_2 plane of the cuprate superconductor is thought to be incompatible with superconductivity.

The power of neutron diffraction is exploited to study materials at different temperatures, and sample gas environment. The MURR-PSD diffractometer with high resolution and high neutron throughput is an important component of this work, enabling fast data collection and low background scattering. Combined with the Rietveld method, the oxygen nonstoichiometry, the electron or hole concentration and TECs of the compounds used for the SOFCs can be found. These results are important for understanding the transport properties of these materials. Since the neutron has a magnetic moment, and its scattering is not dominated by the heavy atoms, it can probe the magnetic structure of the double perovskite superconductor directly, and find any second phase contamination in the specimen.

In chapter 2, the structures of the simple and double perovskite are discussed. In chapter 3, the operating principle of SOFCs, neutron scattering, Rietveld method, and the MURR-PSD instrument are introduced. The studies on the simple perovskite used for SOFCs and the double perovskite superconductor are given in chapters 4 and 5. A summary is given in chapter 6.

Chapter 2 STRUCTURES OF SIMPLE AND DOUBLE PEROVSKITES

There are three kinds of distortions in the perovskite structure: 1) tilting of the anion octahedra. 2) displacements of the cations, and 3) distortions of the octahedra. The distortion 2 is the direct origin of the ferroelectricity of certain perovskites, and the distortion 3 is usually associated with distortion 2. In this chapter, only distortion 1 is discussed. It is the most important distortion in establishing the overall space-group symmetry of the particular perovskite.

2.1 THE STRUCTURE OF THE SIMPLE PEROVSKITE ABO_3

The ideal structure of the simple perovskite ABO_3 (where A is a large cation, B is a small cation) is cubic with $\text{Pm}\bar{3}\text{m}$ symmetry. Figure 2.1 shows the ideal structure with the A or B cation at the center of the cube. The small B cation has 6 neighboring O atoms and the large A cation has 12 neighboring O atoms. The bond length of B-O is much smaller than that of A-O, so the interaction between B and O is strong, and the BO_6 octahedron behaves as a rigid body. Every two neighboring BO_6 octahedra share a common O atom; the large A cations occupy the interstices of these octahedra.

In the ideal cubic structure, the bond length of B-O and A-O has a relation as follows:

$$L_{\text{A-O}} = \sqrt{2}L_{\text{B-O}} \quad (2.1)$$

However, the relative sizes of cation A and B are not always matched well, so that sometimes the octahedron BO_6 has to rotate and tilt as a whole to fit this size mismatch.

This rotation and tilting will distort the perovskite structure. In order to describe this distortion, a tolerance factor is introduced as follows: ⁽¹⁸⁾

$$t = \frac{r_A + r_O}{\sqrt{2}(r_B + r_O)} \quad (2.2)$$

Where r_i ($i=A, B$, and O) is the ionic radius of each element. The structure is cubic when t is close to 1, and transforms to rhombohedral when t is between 0.96 and 1, and then to the orthorhombic structure when t is smaller than 0.96.

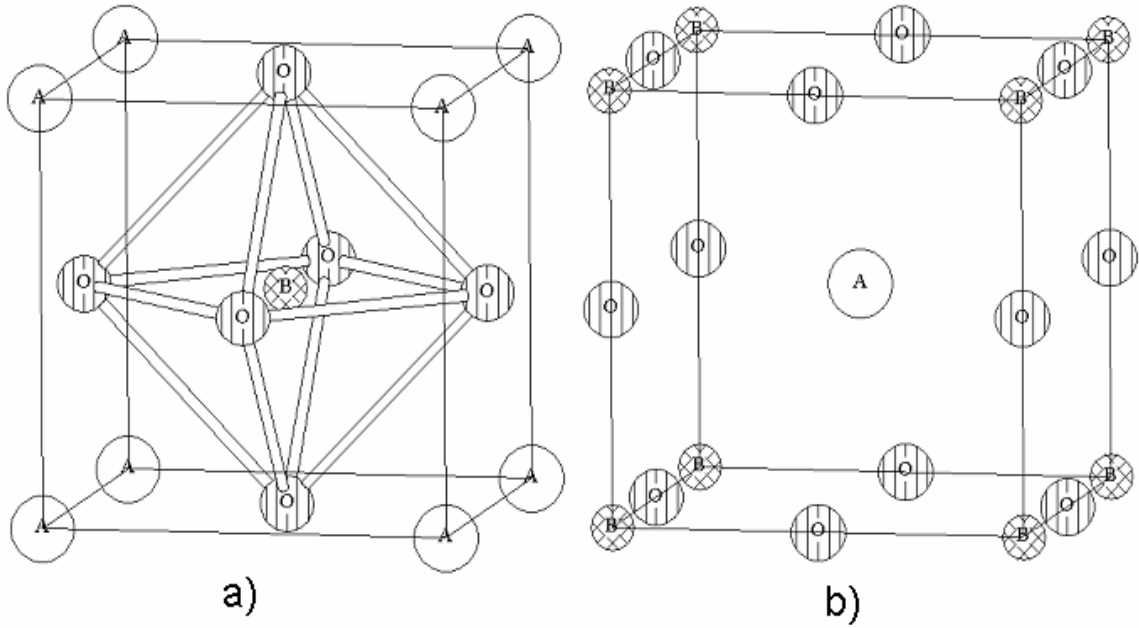


Figure 2.1: The ideal perovskite structure with the B atom at the body center (a) or the A atom at the body center (b).

The oxygen influence is not considered in the distortion described above, but oxygen vacancies influence the distortion. Typically the presence of oxygen vacancies can reduce the distortion since they relax the strain in the structure.

TILT SYSTEM

A. M. Glazer investigated the tilt-distortion of the perovskite structure in 1972 and 1975.⁽¹⁹⁻²⁰⁾ The distortion can be classified by a sequence of tilts about the three tetrad axes, the rotation angles are constrained to be less than 15° in order to neglect the dependence of the result on the sequence of operations. The angles of tilts are indicated by a set of three letters which refer in the order [100], [010], and [001], such as abc, which denotes three unequal tilts. The equality of tilts is denoted by repeating the appropriate letter, for example, aac means equal tilts about the [100] and [010] with a different tilt about [001].

The tilt of one octahedron will affect the tilts of the surrounding octahedra since the neighboring octahedra must have a common O atom. The surrounding octahedra in the directions perpendicular to the tilt axis have to tilt opposite about that axis, but the octahedra along the axis have the freedom to have either the same or opposite sense of tilt. Two superscripts + and – are used to show whether the successive octahedra along the axis have the same or opposite tilt. The superscript 0 is used to show no tilt about the axis. Assuming no repeat period consists of more than two octahedra, the 10 distinct possibilities are shown in Table 2.1.

Table 2.1: the 10 distinct possible tilts.⁽¹⁹⁾

$a^+b^+c^+$	$a^+b^+c^-$	$a^+b^-c^-$	$a^-b^-c^-$	3 tilts
$a^0b^+c^+$	$a^0b^+c^-$	$a^0b^-c^-$		2 tilts
$a^0b^0c^+$	$a^0b^0c^-$			1 tilt
$a^0b^0c^0$				no tilts

The tilts of the octahedra affect the crystal structure of perovskite. The most important consequence of the tiltings is the doubling of the unit cell along some directions. Figure 2.2 shows the results of one tilting with the c axis. It is easy to see that the unit cell is doubled along the two directions perpendicular to the axis of tilting. If the sense of tilting is -, the unit cell should be doubled along this axis too. The tilt of the octahedra has several effects on the unit cell, such as the unit cell lengths, unit cell angles, and the lattice type.

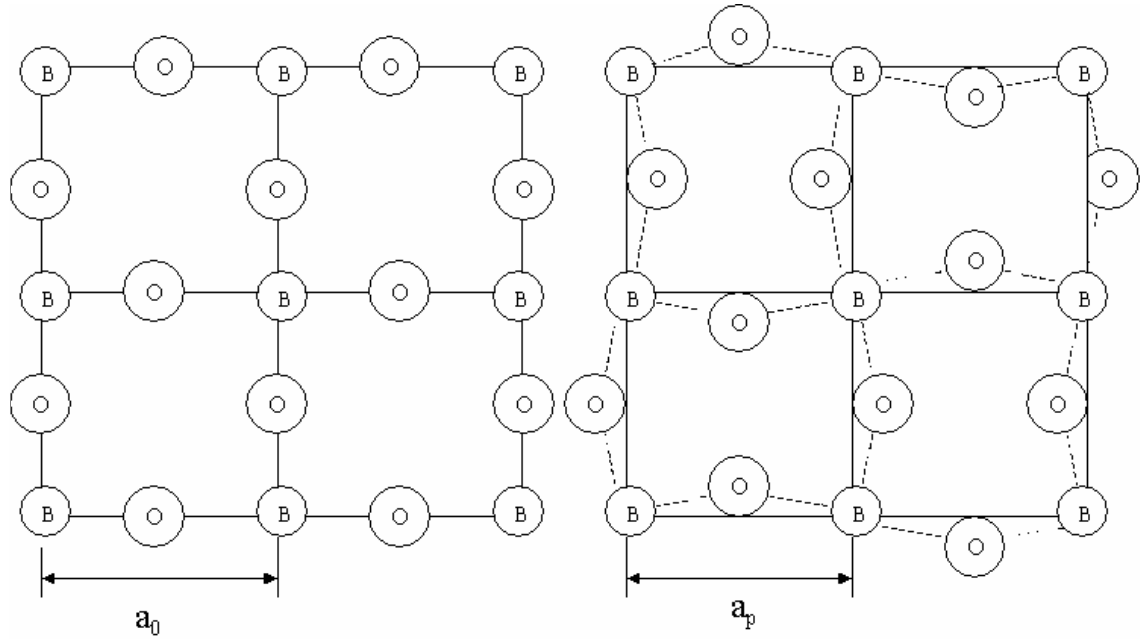


Figure 2.2: The results of the tilt with the c axis only.

a) UNIT CELL LENGTHS

In the Figure 2.2, we can find that the B-B distance becomes shorter if the B-O bond length remains the same as before, and hence reduces the unit cell lengths. If θ_1 , θ_2 ,

and θ_3 are the angles of tilt about the pseudocubic [100], [010], and [001] directions, then the new axial lengths are give by⁽¹⁹⁾

$$\begin{aligned} a_p &= a_0 \cos \theta_2 \cos \theta_3 \\ b_p &= a_0 \cos \theta_1 \cos \theta_3 \\ c_p &= a_0 \cos \theta_1 \cos \theta_2 \end{aligned} \quad (2.3)$$

Where the a_p , b_p , and c_p are the pseudocubic cell lengths, and a_0 is the cell length of the aristotype.

It is easy to see that equality of any two tilt-angles means equality of the cell axes coincident with the tilt axes. For example, $a_p=b_p$ if θ_1 and θ_2 are equal.

b) LATTICE TYPE

Figure 2.3 shows the 10 distinct tilts listed in Table 2.1, each set of three symbols refers to one octahedron. It can be seen that each tilt gives a self-consistent structure, there are no missing signs and each structure has a regular repeat. The lattice-centering conditions can be obtained merely by inspection. For example, $a^+b^+c^+$ is body-centered since the translation operation $(\frac{1}{2} \ \frac{1}{2} \ \frac{1}{2})$ exists, and $a^-b^-c^-$ is all face-centered since all of the translation operations $(\frac{1}{2} \ \frac{1}{2} \ 0)$, $(\frac{1}{2} \ 0 \ \frac{1}{2})$, and $(0 \ \frac{1}{2} \ \frac{1}{2})$ are present.

c) UNIT-CELL ANGLES

In order to find the interaxial angles, attention must be paid to the superscript of the tilt axis, there is a mirror plane perpendicular to the axis if the superscript of this tilt axis is 0 or +, and there is no mirror plane perpendicular to the axis if the superscript of this tilt axis is -. For example, we check the $a^+b^+c^-$ case in Figure 2.3, the $+++$, $---$, $++-$, and $+-$ are the images of $+++$, $++-$, $---$, and $+-$ respectively, so there is a mirror plane

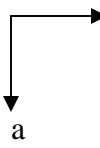
	First Layer			Second Layer			Symbol	Lattice
	+++	-+-	+++	--+	+--	--+	$a^+b^+c^+$	I
	+- -	--+	+- -	-+-	+++	-+-		
	+++	-+-	+++	--+	+--	--+		
	+++	-+-	+++	-- -	+ - +	-- -	$a^+b^+c^-$	P
	+- -	--+	+- -	- + +	+++	- + +		
	+++	-+-	+++	-- -	+ - +	-- -		
	+++	-- -	+++	-- -	+++	-- -	$a^+b^-c^-$	A
	+- -	- + +	+- -	- + +	+ - -	- + +		
	+++	-- -	+++	-- -	+++	-- -		
	+++	-- -	+++	-- -	+++	-- -	$a^-b^-c^-$	F
	0++	0+-	0++	0-+	0--	0-+	$a^0b^+c^+$	I
	0--	0-+	0--	0+-	0++	0+-		
	0++	0+-	0++	0-+	0--	0-+		
	0++	0+-	0++	0--	0-+	0--	$a^0b^+c^-$	B
	0--	0-+	0--	0++	0+-	0++		
	0++	0+-	0++	0--	0-+	0--		
	0++	0--	0++	0--	0++	0--	$a^0b^-c^-$	F
	0--	0++	0--	0++	0--	0++		
	0++	0--	0++	0--	0++	0--		
	00+	00-	00+	00+	00-	00+	$a^0a^0c^+$	C
	00-	00+	00-	00-	00+	00-		
	00+	00-	00+	00+	00-	00+		
	00+	00-	00+	00-	00+	00-	$a^0a^0c^-$	F
	00-	00+	00-	00+	00-	00+		
	00+	00-	00+	00-	00+	00-		
	000	000	000	000	000	000	$a^0a^0a^0$	P
	000	000	000	000	000	000		
	000	000	000	000	000	000		

Figure 2.3: Schematic diagram illustrating all the possible senses of tilts. Each set of three symbols refers to one octahedron.⁽¹⁹⁾

perpendicular to a axis. But the --- is not an image of +++, so there is no mirror plane perpendicular to c axis.

After finding the mirror planes perpendicular to the axis, it is easy to find the angles between the axes. Any axis with superscript 0 or + is perpendicular to the other axes, and any two axes with – superscript mean that the relevant cell axes are inclined to each other.

The space group of the tilt systems can be determined by drawing a plan of the structure and then filling in the symmetry elements. Table 2.2 gives the space groups of the all tilt systems; the space group marked with an asterisk refers to the axes defined by the matrix given below.

2.2 THE STRUCTURE OF DOUBLE PEROVSKITE $A_2BB'O_6$

The simple perovskite ABO_3 has a large family. Most of the metallic ions can be incorporated into the perovskite structure. In order to optimize electronic or catalytic properties for specific applications, the method of partial substitution of the A or B site cations is widely used. Substitution of cation B' for B leads, in general, to the solution $AB_{1-x}B'_xO_3$, where the B and B' cations occupy the original cation site of the simple structure randomly if B and B' have similar sizes. But if $x \approx 0.5$ and B and B' are sufficiently different in size, the B site cation will be ordered, and the formula is written as $A_2BB'O_6$ and the compounds are called double perovskites. There are two types of B site cation ordering reported by Anderson et al, ⁽²¹⁾ one is rock-salt ordering, i.e., the cations of B and B' order into alternate octahedra, the other one is a layered ordering of cations of B and B'. Most double perovskites have rock salt ordering. In this discussion, only the rock salt ordering is considered.

Table 2.2: complete list of possible simple tilt systems⁽²⁰⁾

Serial number	Symbol	Lattice centring	Multiple cell	Relative pseudocubic subcell parameters	Space group	
Three-tilt systems						
(1)	$a^+b^+c^+$	I	$2a_p \times 2b_p \times 2c_p$	$a_p \neq b_p \neq c_p$	Immm (No. 71)	
(2)	$a^+b^+b^+$	I		$a_p \neq b_p = c_p$	Immm (No. 71)	
(3)	$a^+a^+a^+$	I		$a_p = b_p = c_p$	Im3 (No. 204)	
(4)	$a^+b^+c^-$	P		$a_p \neq b_p \neq c_p$	Pmmn (No. 59)	
(5)	$a^+a^+c^-$	P		$a_p = b_p \neq c_p$	Pmmn (No. 59)	
(6)	$a^+b^+b^-$	P		$a_p \neq b_p = c_p$	Pmmn (No. 59)	
(7)	$a^+a^+a^-$	P		$a_p = b_p = c_p$	Pmmn (No. 59)	
(8)	$a^+b^-c^-$	A		$a_p \neq b_p \neq c_p$	$\alpha \neq 90^\circ$	A2 ₁ /m11 (No. 11)
(9)	$a^+a^-c^-$	A		$a_p = b_p \neq c_p$	$\alpha \neq 90^\circ$	A2 ₁ /m11 (No. 11)
(10)	$a^+b^-b^-$	A		$a_p \neq b_p = c_p$	$\alpha \neq 90^\circ$	Pmnb (No. 62) *
(11)	$a^+a^-a^-$	A		$a_p = b_p = c_p$	$\alpha \neq 90^\circ$	Pmnb (No. 62) *
(12)	$a^-b^-c^-$	F		$a_p \neq b_p \neq c_p$	$\alpha \neq \beta \neq \gamma \neq 90^\circ$	F $\bar{1}$ (No. 2)
(13)	$a^-b^-b^-$	F		$a_p \neq b_p = c_p$	$\alpha \neq \beta \neq \gamma \neq 90^\circ$	I2/a (No. 15) *
(14)	$a^-a^-a^-$	F		$a_p = b_p = c_p$	$\alpha \neq \beta \neq \gamma \neq 90^\circ$	R $\bar{3}c$ (no. 167)
Two-tilt systems						
(15)	$a^0b^+c^+$	I	$2a_p \times 2b_p \times 2c_p$	$a_p < b_p \neq c_p$	Immm (No. 71)	
(16)	$a^0b^+b^+$	I		$a_p < b_p = c_p$	I4/mmm (No. 139)	
(17)	$a^0b^+c^-$	B		$a_p < b_p \neq c_p$	Bmmb (No. 63)	
(18)	$a^0b^+b^-$	B		$a_p < b_p = c_p$	Bmmb (No. 63)	
(19)	$a^0b^-c^-$	F		$a_p < b_p \neq c_p$	$\alpha \neq 90^\circ$	F2/m11 (No. 12)
(20)	$a^0b^-b^-$	F		$a_p < b_p = c_p$	$\alpha \neq 90^\circ$	Imcm (No. 74) *
One-tilt systems						
(21)	$a^0a^0c^+$	C	$2a_p \times 2b_p \times 2c_p$	$a_p = b_p < c_p$	C4/mmb (No. 127)	
(22)	$a^0a^0c^-$	F		$a_p = b_p < c_p$	F4/mmc (No. 140)	
Zero-tilt system						
(23)	$a^0a^0c^0$	P	$a_p \times b_p \times c_p$	$a_p = b_p = c_p$	Pm $\bar{3}m$ (No. 221)	

* These space-group symbols refer to axes chosen according to the matrix transformation

$$\begin{pmatrix} 1 & 0 & 0 \\ 0 & \frac{1}{2} & -\frac{1}{2} \\ 0 & \frac{1}{2} & \frac{1}{2} \end{pmatrix}$$

In the cubic structure, the unit cell will be doubled along all directions due to B site ordering. The lattice changes from simple cubic (space group $\text{Pm}\bar{3}\text{m}$) to face-centered cubic (space group $\text{Fm}\bar{3}\text{m}$). In addition to the B site ordering, tilting of octahedra can be present. In order to figure out the crystal structure of a double perovskite, we have to consider the combined effect of cation ordering and octahedral tilting.

The B site cation ordering will always result in a loss of symmetry, either space-group symmetry elements or translational symmetry. The symmetry operations that relate neighboring octahedral sites will be destroyed since the octahedral cation sites are no longer equivalent. In 1997, Woodward⁽²²⁾ examined all of the 23 tilt systems proposed by Glazer for simple ABO_3 perovskites, and checked the symmetry elements which would be destroyed in the $\text{A}_2\text{BB}'\text{O}_6$ double perovskite by the B site ordering. His results are given in table 2.3. The space groups for the simple tilt systems proposed by Glazer are given also. For each tilt system, the space group describing the double perovskite is a maximal nonisomorphic subgroup of the space group describing the simple perovskite, and all the space groups of double perovskites are subgroups of $\text{Fm}\bar{3}\text{m}$.

Table 2.3: Space group for all possible simple tilt systems both with and without 1:1 cation ordering. The space group (no ordering) of system (5), (7), (17), and (18) are different than the ones in table 2.2, since there are slight distortions of the octahedra in order to retain the connectivity of the octahedra.⁽²²⁾

Tilt system number	Tilt system Symbol	Space group (no ordering)	Space group (1:1 ordering)
Three-tilt systems			
(1)	$a^+b^+c^+$	Immm (#71)	Pnnn (#48)
(2)	$a^+b^+b^+$	Immm (#71)	Pnnn (#48)
(3)	$a^+a^+a^+$	$Im\bar{3}$ (#204)	$Pn\bar{3}$ (#201)
(4)	$a^+b^+c^-$	Pmmn (#59-2)	P2/c (#13)
(5)	$a^+a^+c^-$	$P4_2/nmc$ (#137-2)	$P4_2/n$ (#86)
(6)	$a^+b^+b^-$	Pmmn (#59-2)	P2/c (#13)
(7)	$a^+a^+a^-$	$P4_2/nmc$ (#137-2)	$P4_2/n$ (#86)
(8)	$a^+b^-c^-$	$P2_1/m$ (#11-1)	$P\bar{1}$ (#2)
(9)	$a^+a^-c^-$	$P2_1/m$ (#11-1)	$P\bar{1}$ (#2)
(10)	$a^+b^-b^-$	Pnma (#62)	$P2_1/n$ (#14-2)
(11)	$a^+a^-a^-$	Pnma (#62)	$P2_1/n$ (#14-2)
(12)	$a^-b^-c^-$	$F\bar{1}$ (#2)	$F\bar{1}$ (#2)
(13)	$a^-b^-b^-$	I2/a (#15-3)	$F\bar{1}$ (#2)
(14)	$a^-a^-a^-$	$R\bar{3}c$ (#167-2)	$R\bar{3}$ (#148-2)
Two-tilt systems			
(15)	$a^0b^+c^+$	Immm (#71)	Pnnn (#48)
(16)	$a^0b^+b^+$	I4/mmm (#139)	$P4_2/nm$ (#134)
(17)	$a^0b^+c^-$	Cmcm (#63)	C2/c (#15-1)
(18)	$a^0b^+b^-$	Cmcm (#63)	C2/c (#15-1)
(19)	$a^0b^-c^-$	I2/m (#12-3)	$I\bar{1}$ (#2)
(20)	$a^0b^-b^-$	Imma (#74)	I2/m (#12-3)
One-tilt systems			
(21)	$a^0a^0c^+$	$P4/mbm$ (#127)	$P4/mnc$ (#128)
(22)	$a^0a^0c^-$	$I4/mcm$ (#140)	$I4/m$ (#87)
Zero-tilt system			
(23)	$a^0a^0c^0$	$Pm\bar{3}m$ (No. 221)	$Fm\bar{3}m$ (#225)

Chapter 3: THE PRINCIPLE OF SOFC AND NEUTRON SCATTERING

3.1 THE PRINCIPLE OF SOFCs

In 1839, William Robert Grove first proposed the concept of the fuel cell,⁽²³⁾ which can convert chemical energy into electrical energy directly without combustion.

Compared to conventional methods of power generation, fuel cells have several advantages: higher energy conversion efficiency, much lower production of pollutants, potentially better reliability and durability (since there are no moving parts in the fuel cell), and a variety of fuel sources.

A fuel cell can be classified by its electrolyte; the SOFC is a fuel cell using solid oxides as its electrolyte. The first SOFC was operated at 1000 °C by Baur and Preis in 1937.⁽²⁴⁾ The SOFCs have several additional advantages over other types of fuel cells, such as use of nonprecious materials and no liquids involved in the fuel cell. The use of solid electrolytes eliminates material corrosion and electrolyte management problems, and because all the components are solid, SOFCs can be fabricated in very thin layers. Cell components can be configured into unique shapes. SOFCs are operated at high temperature (>600 °C), the high temperature promotes rapid reaction kinetics, and the reforming of hydrocarbon fuels within the fuel cell is possible.

A single cell has three components: anode, electrolyte, and cathode. The fuel (such as H₂, CO) flows to the anode side, and the oxidant (such as air or O₂) flows to the cathode side. The operation principle is illustrated in Figure 3.1. Oxygen at the cathode side reacts with the incoming electrons from the external circuit to form the oxygen ions, which migrate to the anode side through the whole cell. Then, the oxygen ions combine

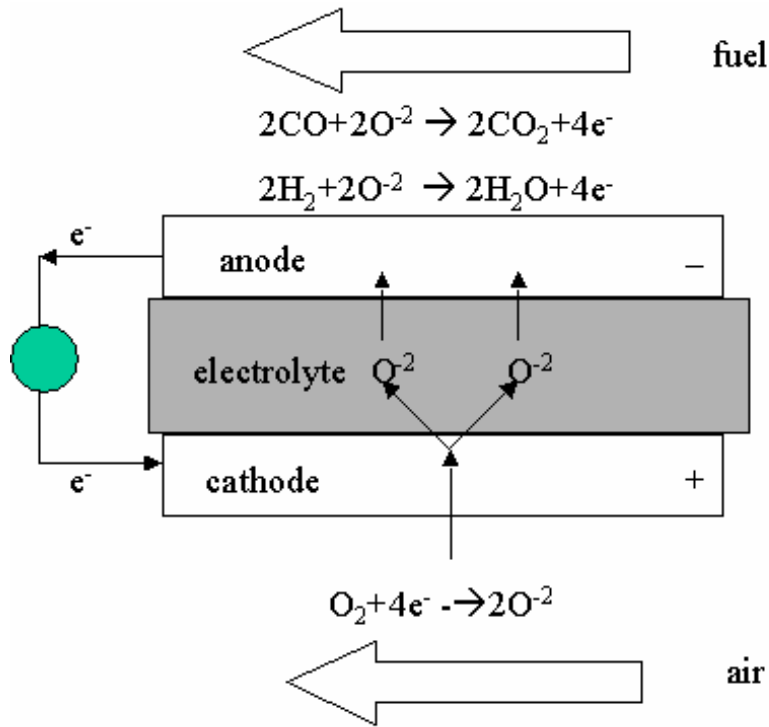


Figure 3.1: The operating principle of a solid oxide fuel cell.

with the fuel (H_2 , CO) to form H_2O or CO_2 , and liberate the electrons, which flow from the anode to the cathode through the external circuit. Therefore, the anode and cathode should serve a triple role as a catalyst, an electrical conductor, and an oxygen ion conductor. In addition, the anode and cathode must have chemical stability in the oxidizing (for cathode) or reducing (for anode) environment, chemical compatibility with the electrolyte and similar thermal expansion coefficients as the electrolyte, to avoid separation or cracking during fabrication and operation. The electrolyte should be dense to prevent gas mixing, serve as an oxygen ion conductor to let O^{2-} transport from the air side to the fuel side, and electrically insulating to force the electron flow to the external circuit. The open circuit voltage (EMF) can be determined from the chemical potential of oxygen (i.e. oxygen activity) and is expressed by the Nernst Equation ⁽²⁵⁾ as follows:

$$EMF = \Gamma \frac{RT}{4F} \ln \left(\frac{(P_{O_2})_a}{(P_{O_2})_b} \right) \quad (3.1)$$

Where Γ : transference number (ion conductivity/total conductivity)

T: operation temperature.

F: Faraday constant.

$(P_{O_2})_a$ and $(P_{O_2})_b$: the oxygen activity on the cathode side and on the anode side.

The EMF of a single cell is about 1.10 V if air is used as the oxidant, so the cells should be stacked together for application. A new component called interconnect is used to connect the anode and cathode of two fuel cells. There are two basic geometries for the SOFC stacking: planar and tubular. Figure 3.2 shows the arrangements of the electrodes in the planar and tubular geometries.

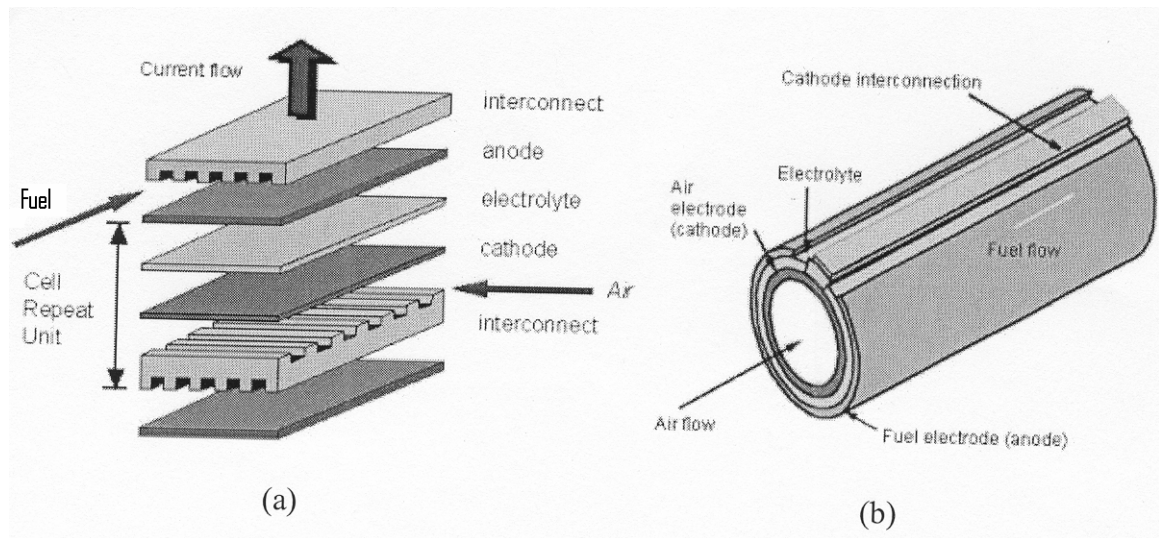


Figure 3.2: Planar (a) and Tubular (b) design of solid oxide fuel cells.

3.2 NEUTRON SCATTERING

Neutrons are particles with mass m , no charge, and spin $\frac{1}{2}$. Their magnetic dipole moment is $\mu_n = -1.9134\mu_N$, where μ_N is the nuclear magneton. The wave vector \vec{K} and the momentum of the neutron \vec{P} are related as follows:

$$\vec{P} = \hbar \vec{K} \quad (3.2)$$

So the de Broglie wavelength of the neutron is

$$\lambda = \frac{h}{p} = \frac{9.045}{\sqrt{E}} \quad (3.3)$$

Where E is the energy of the neutron in units of meV.

The wavelength of a thermal neutron (5-100 meV) is in the range of 4.045-0.9045 Å, which is of the order of interatomic distances in solids and liquids. Thus, thermal neutron scattering is a valuable tool for investigating many important features of matter, particularly condensed matter, due to the following advantages:

- 1) The wavelength of the thermal neutron is of the order of interatomic distances in solids and liquids. Thus, interference effects occur, and information on the structure of the scattering system will be given.
- 2) Neutrons are scattered by the nuclear force. The form factor is flat since the nuclear force is a short-range force. The cross sections vary from isotope to isotope in a more or less random manner, and therefore, the neutron scattering is not dominated by the heavy atoms, as are x-rays.
- 3) The energy of a thermal neutron is of the same order as that of many excitations in condensed matter: the energy change is often a large fraction of its initial

energy when the neutron is inelastically scattered by the creation or annihilation of an excitation.

- 4) The neutron has a magnetic moment: it can be scattered by the magnetic field generated by the unpaired electrons in magnetic atoms. The elastic magnetic scattering gives information about the magnetic moment and magnetic ordering of magnetic atoms; inelastic magnetic scattering gives the energies of magnetic excitations.
- 5) Compared with x-rays, the absorption of neutrons is quite small for most nuclei, except for B, Cd, Sm, Eu and Gd. Therefore, neutron scattering is a bulk probe and is not dominated by the surface.

NUCLEAR SCATTERING

Neutrons have no charge; there are no Coulomb barriers to be overcome when neutrons are close to the nucleus. Neutrons interact with the nucleus via nuclear forces, and the nuclear forces are very short range, only 10^{-14} - 10^{-15} m, which is much smaller than the wavelength of thermal neutrons. In this circumstance, the scattered wave is spherically symmetric, so the form factor of neutron is flat. Figure 3.3 shows the scattering of neutrons by a single fixed nucleus, the scattering is elastic since there is no kinetic energy exchange between the neutron and the fixed nucleus, and we can use only one parameter b , the scattering length, to describe the wave function of the elastically scattered neutron.

The scattering length b is complex; the imaginary part corresponds to absorption. For most nuclei, the imaginary part is small, and the scattering length is independent of the energy of neutron.

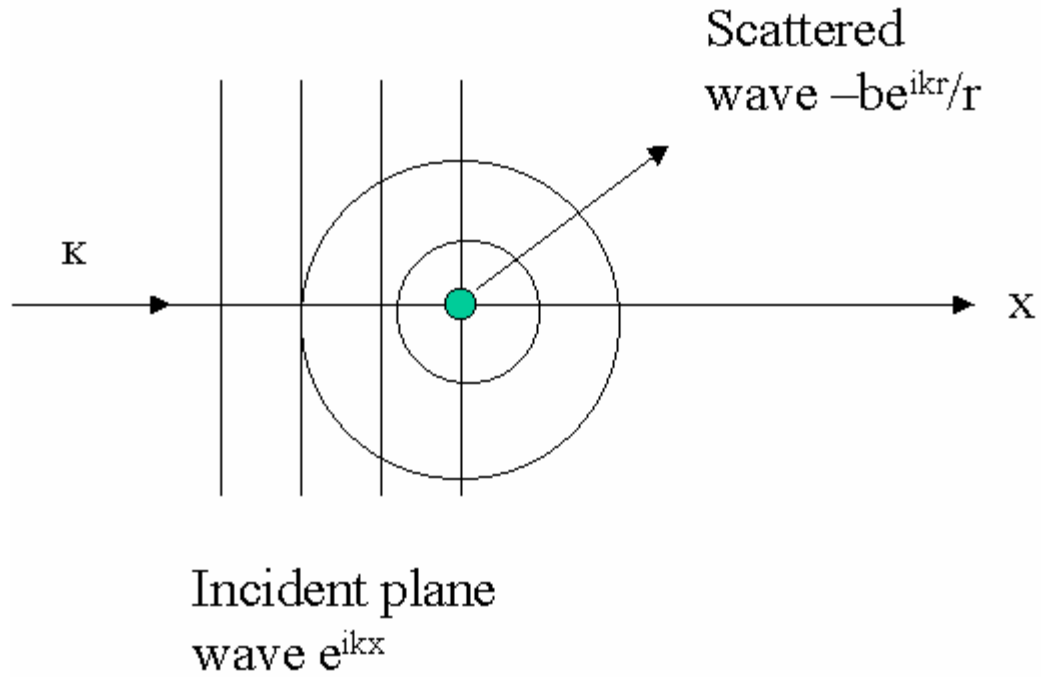


Figure 3.3: A neutron scattered by a single fixed nucleus.

The value of the scattering length depends on the particular nucleus and the spin state of the nucleus-neutron system. For nuclei with spins $I \neq 0$, there are two scattering lengths b_+ and b_- corresponding to the nucleus-neutron system whose spin is either $I+1/2$ or $I-1/2$. For nuclei without spin, there is one value of the scattering length only.

Consider a scattering system consisting of a single element. The scattering length b may vary from one nucleus to another due to the presence of isotopes or nuclear spin or both. Let i be the index of the isotope and the spin of nucleus-neutron system, b_i and f_i are the scattering length and relative frequency. Then the average value of b and b^2 are ⁽²⁶⁾

$$\bar{b} = \sum_i f_i b_i \quad (3.4)$$

$$\overline{b^2} = \sum_i f_i b_i^2 \quad (3.5)$$

Then the coherent and incoherent scattering cross-section can be defined as ⁽²⁶⁾

$$\sigma_{coh} = 4\pi \overline{b}^2, \text{ and } \sigma_{inc} = 4\pi \{\overline{b^2} - \overline{b}^2\} \quad (3.6)$$

The interaction between neutrons and nuclei can be described by the Fermi pseudopotential function as follows: ⁽²⁶⁾

$$V(\vec{r}) = \frac{2\pi\hbar}{m} b \delta(\vec{r}) \quad (3.7)$$

Where \vec{r} is the displacement of the nuclei, m is the mass of the neutron, b is the scattering length, and $\delta(\vec{r})$ is a three-dimensional Dirac delta function.

In general, neutrons will be scattered by a collection of nuclei. Using the definition of a partial differential cross-section, Fermi's golden rule, and the Fermi pseudopotential, the partial differential cross-section can be expressed as follows: ⁽²⁶⁾

$$\frac{d^2\sigma}{d\Omega dE'} = \frac{k'}{k} \frac{1}{2\pi\hbar} \sum_{jj'} b_j b_{j'} \int_{-\infty}^{\infty} \langle \exp\{-i\vec{q} \cdot \vec{R}_{j'}(0)\} \exp\{i\vec{q} \cdot \vec{R}_j(t)\} \rangle \times \exp(-i\omega t) dt \quad (3.8)$$

where j, j': index of the jth, j'th nucleus

$\vec{R}_j, \vec{R}_{j'}$: displacement of the jth and j'th nucleus

$\vec{q} = \vec{k} - \vec{k}'$ is the scattering vector.

\vec{k} is the wave vector of incoming neutrons.

\vec{k}' is the wave vector of scattered neutrons.

$b_j, b_{j'}$ are the scattering length of the jth, j'th nucleus.

If the scattering system consists of a single element, the expression (3.8) can be divided into two parts, the coherent and incoherent part, as follows:⁽²⁶⁾

$$\frac{d^2\sigma}{d\Omega dE'} = \frac{\sigma_{coh}}{4\pi} \frac{k'}{k} \frac{1}{2\pi\hbar} \sum_{jj'} \int \langle j', j \rangle \exp(-i\omega t) dt + \frac{\sigma_{inc}}{4\pi} \frac{k'}{k} \frac{1}{2\pi\hbar} \sum_j \int \langle j, j \rangle \exp(-i\omega t) dt \quad (3.9)$$

$$\text{where } \langle j', j \rangle = \langle \exp\{-i\vec{q} \bullet \vec{R}_{j'}(0)\} \exp\{i\vec{q} \bullet \vec{R}_j(t)\} \rangle \quad (3.10)$$

The first term is the coherent part, which depends on the correlation between the positions of the same nucleus at different times, and the correlation between the positions of different nuclei at different times. It gives interference effects, and thus gives information about the structure of materials. The second term is the incoherent part, which depends on the correlation between the positions of the same nucleus at different times only, and the neutron interacts with each nucleus in the scattering system independently, and thus no interference effects will be seen in the incoherent scattering.

NUCLEAR SCATTERING BY CRYSTALS

In crystals, atoms are distributed periodically in three dimensions. Equation (3.9) can be simplified further. In this paper, we consider the elastic scattering only. Since there is no energy transfer, the coherent and incoherent differential cross-sections are as follows:⁽²⁶⁾

$$\left(\frac{d\sigma}{d\Omega}\right)_{coh,el} = N \frac{(2\pi)^3}{v_0} \sum_{\vec{\tau}} \delta(\vec{q} - \vec{\tau}) \left| F_N(\vec{q}) \right|^2 \quad (3.11)$$

$$\left(\frac{d\sigma}{d\Omega}\right)_{inc,el} = N \sum_i \{ \overline{b_i^2} - (\overline{b_i})^2 \} \exp(-2W_i) \quad (3.12)$$

$$\text{Where } F_N(\vec{q}) = \sum_i \overline{b_i} \exp(i\vec{q} \bullet \vec{r}_i) \exp(-W_i) \quad (3.13)$$

N is the number of unit cells in the crystal. τ is the reciprocal lattice vector, and W_i is the Debye-Waller factor.

The δ term in eq. (3.11) tells us that the scattering occurs only when the scattering vector \vec{q} is equal to one of the reciprocal lattice vectors. This condition is the same as Bragg's law. The elastic coherent scattering will happen in some directions, but for the incoherent term, there is no such constraint, incoherent scattering will be seen in all directions.

For the study of crystal structures, the best results can be gotten by using single crystals, but single crystal samples with suitable size are not always available, and a polycrystalline sample is easy to get. Neutron powder diffraction is widely used for crystal structure refinement. Figure 3.4 shows the constant wavelength powder diffraction process.

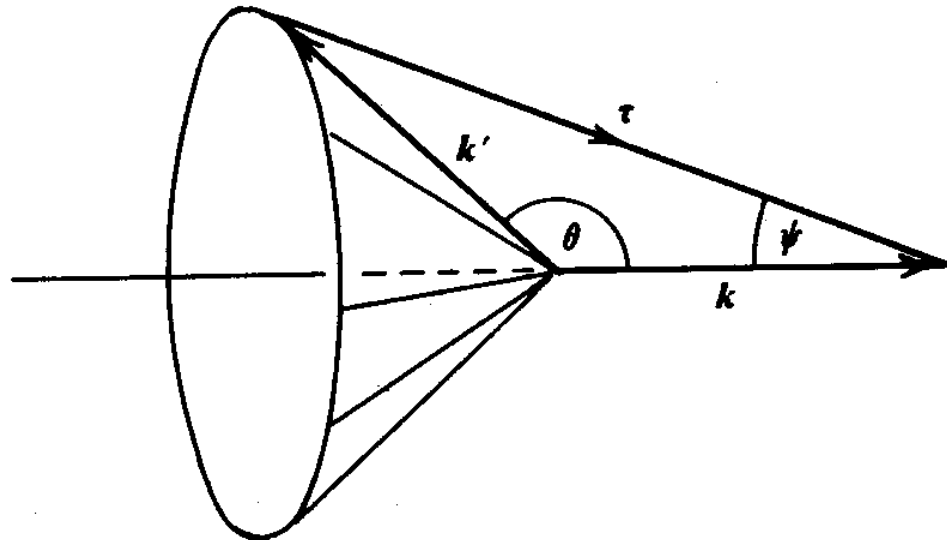


Figure 3.4: Debye-Scherrer cone for Bragg scattering from a powder. ⁽²⁶⁾

In Figure 3.4, a monochromatic neutron beam with wave vector $\vec{K} = \text{constant}$ is incident on a powder sample, i. e. a sample of a very large number of small single crystals with random orientation. For any specified value of $|\tau| < 2K$, the wave vector \vec{K}' of the scattered neutron will lie on a cone, which is called a Debye-Scherrer cone. Only the small crystals whose τ vectors lie on the cone with the axis along \vec{K} and the semi-angle $\Psi = \frac{1}{2}\pi - \frac{1}{2}\theta$, can contribute to the scattering, and the total cross-section for each cone is: ⁽²⁶⁾

$$\sigma_{tot.\tau}(cone) = \frac{V}{v_0^2} \times \frac{\lambda^3}{4 \sin \frac{1}{2}\theta} \times \sum_{\tau} |F_N(\vec{\tau})|^2 \quad (3.14)$$

where V is the total volume of sample, and v_0 is the volume of the unit cell.

If the detector is at a distance r from the sample and has an effective diameter d , the counting rate is: ⁽²⁶⁾

$$P = \Phi \times \frac{d}{2\pi r \sin \theta} \sigma_{tot.\tau}(cone) \quad (3.15)$$

MAGNETIC SCATTERING

In addition to the nuclear force between the neutron and nuclei, there is another interaction between the neutrons and magnetic atoms. Since the neutron has a magnetic moment, the neutron will experience a magnetic force when it passes close to the magnetic field produced by the magnetic atoms. Thus, magnetic scattering will occur. The magnetic moment of an atom or ion is normally dominated by the unpaired electrons in the partially filled electronic shell. The most common magnetic ions are the 3d transition metal ions and the rare earth ions. The unpaired electrons of the 3d transition metal ions are in the outer shell; they are sensitive to the crystal field. The contribution to

the magnetic moment from the orbital angular momentum is usually insignificant due to orbital quenching. However, for rare earth ions, both the spin and orbital angular momentum can give contributions to the magnetic moment, because the unpaired 4f electrons are not in the outer shell, and the affect of the crystal field is unimportant.

The magnetic moments of the magnetic atoms can be ordered or disordered. When the magnetic moments are disordered, such as in paramagnetic materials, the directions of the magnetic moments are random, and the magnetic scattering of the neutron is totally incoherent, the differential cross section is: ⁽²⁷⁾

$$d\sigma_m = \frac{2}{3} S(S+1) \left(\frac{e^2 \gamma}{mc^2} \right)^2 f^2 \quad (3.16)$$

where m is the mass of the electron, S is the spin of the atom, γ is 1.9134, f is the magnetic form factor, it behaves like a x-ray form factor, but falls off even more rapidly with increasing angle, because the magnetic scattering is mainly from the unpaired electrons in the outer shell, while x-rays probe all electron orbitals.

When the magnetic moments are ordered, the magnetic moments of neighboring atoms are parallel (for ferromagnets), antiparallel (for antiferromagnets) or in other arrangement, such as canted antiferromagnets (weak ferromagnets), spirals, cones, or spin density waves. These moments give rise to Bragg diffraction in the same manner as the nuclear interaction. So, the magnetic scattering is coherent, and the coherent differential magnetic cross section is given by: ⁽²⁷⁾

$$d\sigma_m = q^2 S^2 \left(\frac{e^2 \gamma}{mc^2} \right)^2 f^2 \quad (3.17)$$

where \vec{q} , the magnetic interaction vector, is defined as: ⁽²⁷⁾

$$\vec{q} = \vec{\varepsilon}(\vec{\varepsilon} \bullet \vec{k}) - \vec{k} \quad (3.18)$$

in eq. (3.18), $\vec{\varepsilon}$ is the unit vector of scattering vector, \vec{k} is the unit vector of the spin direction of atom. The magnitude of \vec{q} is $\sin\alpha$, where α is the angle between $\vec{\varepsilon}$ and \vec{k} . Equation (3.18) clearly shows that, for a fixed reflection, only the component of the magnetic moment perpendicular to the scattering vector gives a contribution to magnetic scattering.

The magnetic scattering length p is more often used and is defined as: ⁽²⁷⁾

$$p = \frac{e^2 \gamma}{mc^2} Sf = 0.54 Sf \times 10^{-12} \text{ cm} \quad (3.19)$$

The total differential cross section, including both nuclear and magnetic scattering, can be given as: ⁽²⁷⁾

$$d\sigma = b^2 + 2bp\vec{\lambda} \bullet \vec{q} + p^2 q^2 \quad (3.20)$$

Where $\vec{\lambda}$ is the unit vector in the direction of neutron spin. For an unpolarized neutron beam, the second term in equation (3.20) averages to zero, such that the nuclear and magnetic scattering add up independently.

There are two basic magnetic orders: ferromagnetic and anti-ferromagnetic order. For ferromagnetic materials, the magnetic moments located at the magnetic atom sites point in the same direction. In this case the magnetic unit cell is the same as the nuclear one, the magnetic Bragg peaks are coincident with the corresponding nuclear Bragg peaks. For anti-ferromagnetic materials, the magnetic moments have an antiparallel arrangement, which usually split one magnetic atom site in the nuclear unit cell into two different sites in the magnetic unit cell, the periodicity of the magnetic lattice is often

different from the nuclear one, and the distance between the periodic planes in the magnetic unit cell is different from that of the spacing between corresponding planes in the nuclear unit cell. As a result of Bragg's law, the magnetic Bragg peaks will fall between their nuclear counterparts, the magnetic peaks may not be coincident with the nuclear peaks.

3.3 RIETVELD METHOD

Data reduction was a must in crystallography in order to be able to handle a relatively complex structure in the early days (before 1970). Integrated intensities from powder diffraction patterns were therefore the smallest data set one could work with. This method works well to solve the crystal structures of samples with high symmetry, since many peaks are well resolved and integrated intensities can easily be obtained for further refinement. However, with more complex compounds and of lower symmetry, the overlap of peaks is too severe to separate them, and we cannot find enough integrated intensities from non-overlapping reflections to determine all the parameters of the crystal structure.

In 1969, Rietveld ⁽²⁸⁾ presented a new method for analysis of data from powder samples. Instead of using the integrated intensities, The Rietveld method uses the individual intensities at each step, y_i , as data. In this method, a powder diffraction pattern of a polycrystalline material is thought of as a collection of individual reflection profiles, each of which has a profile function, a peak height, a peak position, a breadth, and an integrated area which is proportional to the Bragg intensity. This intensity is proportional to the square of the absolute value of the structure factor. By adjusting the parameters of the model, a best fit between the observed intensity and calculated intensity can be

obtained. The Rietveld method can extract more detailed crystal structure information from powder diffraction data since all the information of the data are used, and there is no effort made in advance to allocate observed intensities to particular Bragg peaks. The refinements are robust and it has been found that the Rietveld method can do multiphase refinement including magnetic scattering, which is treated as a separate phase.

MATHEMATICS OF RIETVELD METHOD

In general, the powder data are digitized, the diffraction pattern is recorded as a numerical intensity value, y_i , at each of several hundred or thousand steps i . The steps can be either in scattering angle, 2θ (for constant wave length case), or some energy parameter such as velocity (for time-of-flight case). The aim of the Rietveld method is to find the minimum of the residual, S_y , which is defined as:

$$S_y = \sum_i \omega_i (y_i - y_{ci})^2 \quad (3.21)$$

where $\omega_i = 1/y_i$

y_i = observed intensity at the i th step

y_{ci} = calculated intensity at the i th step and the sum is over all data points.

The calculated intensities y_{ci} are determined from the square of the structure factor $|F_K|^2$ value calculated from the structure model by summing the calculated contributions from neighboring Bragg reflections plus the background:

$$y_{ci} = s \sum_K L_K |F_K|^2 \Phi(2\theta - 2\theta_K) P_K A + y_{bi} \quad (3.22)$$

where:

s is the scale factor.

K represents the Miller indices, h, k, l for a Bragg reflection.

L_K contains the Lorentz, polarization, and multiplicity factors.

ϕ is the reflection profile function.

P_K is the preferred orientation function.

A is the absorption factor.

F_K is the structure factor for the K^{th} Bragg reflection.

Y_{bi} is the background intensity at the i^{th} step.

In equation (3.22), the structure factor, F_K , is given by:

$$F_K = \sum_j N_j b_j \exp[i2\pi(hx_j + ky_j + lz_j)] \exp[-W_j] \quad (3.23)$$

where:

N_j is the occupancy of the j th atom.

b_j is the scattering length of the j th atom.

h, k, l are the Miller indices.

x_j, y_j , and z_j are the position parameters of the j th atom in the unit cell.

W_j is the Debye-Waller factor, $W_j = 8\pi^2 \overline{u_s^2} \sin^2 \theta / \lambda^2$.

$\overline{u_s^2}$ is the root-mean-square thermal displacement of the j^{th} atom parallel to the diffraction vector.

Each of the different experimental techniques for collecting data has its own most appropriate peak shape function. For the constant wavelength case, Gaussian or pseudo-Voigt functions are adequate representations of the peak shape. Caglioti et al ⁽²⁹⁾ modeled the Gaussian dependence of the full-width-at-half-maximum (FWHM) as a function of θ :

$$H^2 = U \tan^2 \theta + V \tan \theta + W \quad (3.24)$$

Where U, V, and W may be the refinable parameters. For a fixed instrument and ideal sample (no strain or particle size broadening), U, V, and W are determined by the instrument design.

The Caglioti model works well for the low and medium resolution neutron powder diffractometers, but for high resolution neutron powder diffractometers, the instrumental profiles are so narrow that the intrinsic diffraction profile from specimen defects such as microstrain and small crystallite size is now a significant part and it may not have the Caglioti et al. dependence on angle. The observed profile is the convolution of the instrumental profile with the intrinsic diffraction profile.

Preferred orientation arises when there is a strong tendency for the crystallites in a specimen to be oriented more one way, or one set of ways than all others. If this occurs, the reflection intensities will be systematically distorted. The preferred orientation function P_K in equation (3.19) is used to model this phenomenon. Dollase⁽³⁰⁾ gave the preferred orientation function as following:

$$P_K = (G_1^2 \cos^2 \alpha_k + (1/G_1) \sin^2 \alpha_k)^{-3/2} \quad (3.25)$$

Where G_1 is a refinable parameter, and α_K is the angle between hkl and the fibre axis direction.

For constant wavelength data, an absorption correction is indistinguishable from the thermal motion effects, and should not be refined, but may be determined by the sample size, density and isotopic composition.

The background intensity y_{bi} can be obtained from (i) an operator-supplied table of background intensities, or (ii) linear interpolation between operator-selected points in the

pattern, or (iii) a specified background function. A fifth order polynomial background function works well for the data obtained by the PSD of MURR

$$y_{bi} = \sum_{m=0}^5 B_m [(2\theta_i / BKPOS) - 1]^m \quad (3.26)$$

Where BKPOS is the operator-specifiable origin.

The Rietveld method is a least squares minimization procedures, which leads to the calculation of the normal matrix with element M_{jk} given by:

$$M_{jk} = -\sum_i 2\omega_i [(y_i - y_{ci}) \frac{\partial^2 y_{ci}}{\partial x_j \partial x_k} - (\frac{\partial y_{ci}}{\partial x_j})(\frac{\partial y_{ci}}{\partial x_k})] \quad (3.27)$$

in practice, M_{jk} is approximated by ignoring the first term. Because the residual S_y is non-linear, the solution must be found with an iterative procedure in which the shifts, Δx_k , are

$$\Delta x_k = \sum M_{jk}^{-1} \frac{\partial S_y}{\partial x_k} \quad (3.28)$$

The calculated shifts are applied to the initial parameters to produce an improved model, and this whole procedure is then repeated until the cycle number is equal to the design number or the refinement has converged.

3.4 MURR PSD DIFFRACTOMETER

The University of Missouri Research Reactor (MURR) is a pool-type reactor with a Be reflector and a secondary graphite reflector. It has a compact core containing 8 fuel elements. The core is immersed in the light water, which can transport the heat produced by the chain reaction and slow down the fast neutrons. The reactor has a flux trap and 6 beam tubes with neutron flux from 0.5 to 1.2×10^{14} neutrons/cm²sec. The beam tubes are radially placed around the core. Various filters, such as sapphire and Si, are added in the

tube to improve the ratio of the thermal to fast neutrons at the sample position. This modification is helpful to reduce the background, and the low background is very important for the neutron scattering measurements. The powder diffractometer is located at beam port D, which is located 14 inches below the core center line and is approximately tangential to the core. This setting has a lower neutron flux, but it has less fast neutron and gamma rays. This is a real benefit for powder diffraction studies.

The reactor operates at 10MW, 152 hours a week, 52 weeks a year. The large power and extensive operation schedule give us a great opportunity to do neutron scattering measurements. The activity of the reactor is focused on services, (such as production of isotopes, transmutation doping of Si, gemstone coloring), research, (such as nuclear analysis, radiopharmaceutical, and neutron materials science) and education/training.

A schematic diagram of the general layout of the powder diffractometer at MURR is shown in Figure 3.5a, this design is quite different from a conventional diffractometer (Figure 3.5b). For the conventional diffractometer, the constant wavelength neutrons are chosen by the flat mosaic crystal, and the directions of the incoming and scattering wave vectors are chosen by the two Soller collimators, so the scattering vector $Q=2k\sin\theta_m$ is constant since k and θ_m are all fixed. However, for the MURR diffractometer, the monochromatic neutron beam is selected by a double focusing, bent perfect Si crystal monochromator. The wave length of the neutron beam is changed a little bit from side to side due to the rotation of the diffracting planes, but the small difference of the wavelengths is compensated by the small change of the scattering angle, and the scattering vector $Q=2k\sin\theta_m$ can be close to constant. Thus the resolution of the MURR

diffractometer can be as good as the conventional diffractometer with a higher neutron flux at the sample position.

Compared to the flat mosaic crystal monochromator, the double focusing, bent perfect Si crystal monochromator can focus many more neutrons on the sample due to the higher reflectivity, the beam condensation from asymmetric cutting, and the absence of the Soller collimators. A further advantage is the low background due to the low scattering power of the silicon monochromator for fast neutrons and its low incoherent scattering.

The other difference between the two diffractometers is the detector. Instead of using a multi-detector system with individual Soller collimators, the MURR diffractometer uses position sensitive detectors (PSD), which are located 160 cm away from the sample position, span 20° (2θ), and are placed in a moveable neutron shield assembly. The detectors can be moved in steps to cover the whole scattering angle, which is usually 5° - 105° (2θ).

The position sensitive detectors are five linear position sensitive proportional counters, one of which is shown in Figure 3.6 schematically. It is a 1 inch diameter, 24 inch long stainless steel tube, the outer wall is the cathode, and a spring-tensioned wire with $8k\Omega$ resistance connected between the two ends of the tube is the anode. Inside, the tube is filled with 8 atmospheres of helium-3 and 4 atmospheres of argon with 5% CO_2 .

The neutron has no charge; it cannot be detected directly. Helium-3 has a large neutron absorption cross section. The thermal neutron absorption in helium-3 produces two charged particles, a proton and a triton via the following reaction:



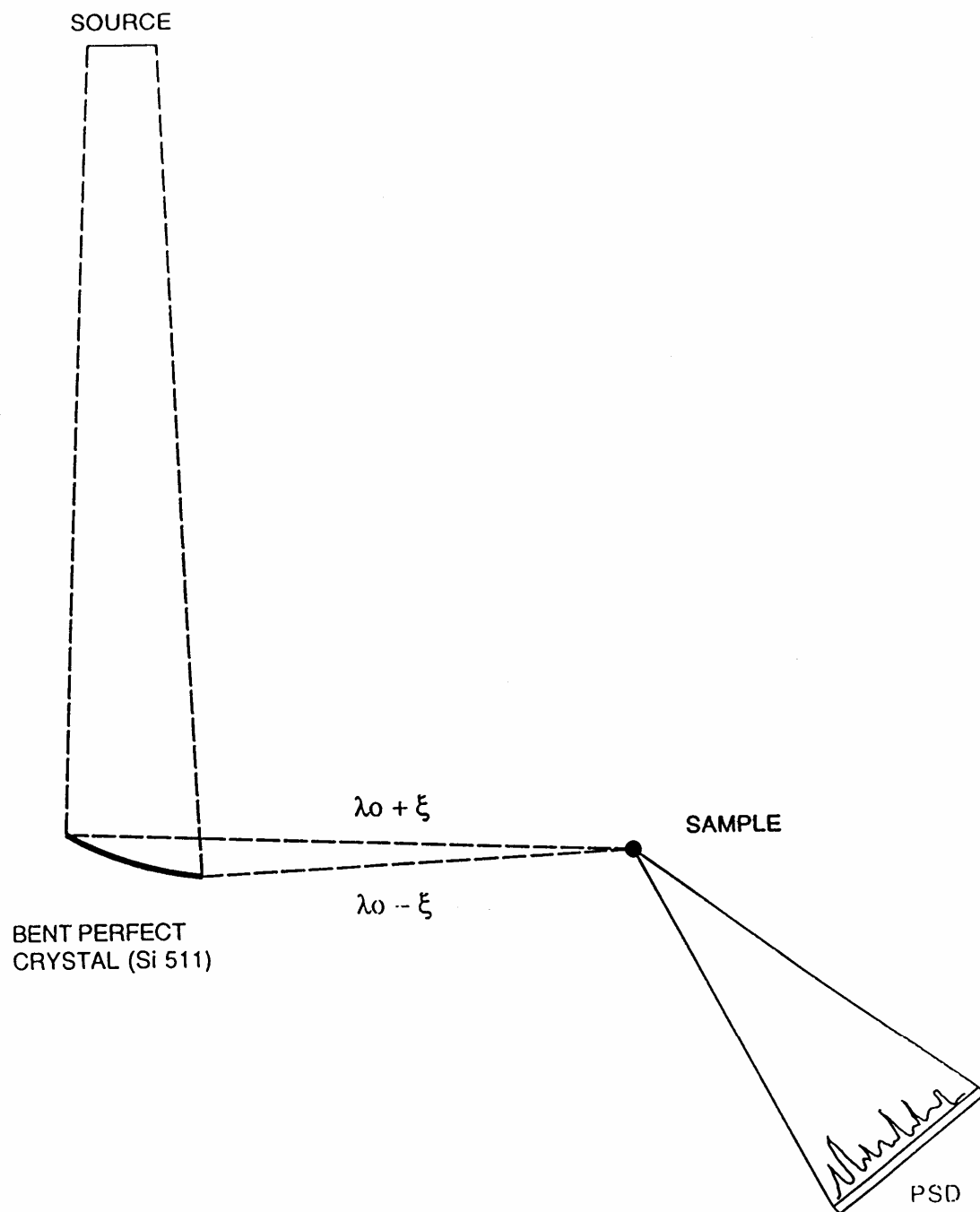


Figure 3.5a: The MURR PSD Double Focusing Powder Diffractometer.

Constant Wavelength Diffractometer

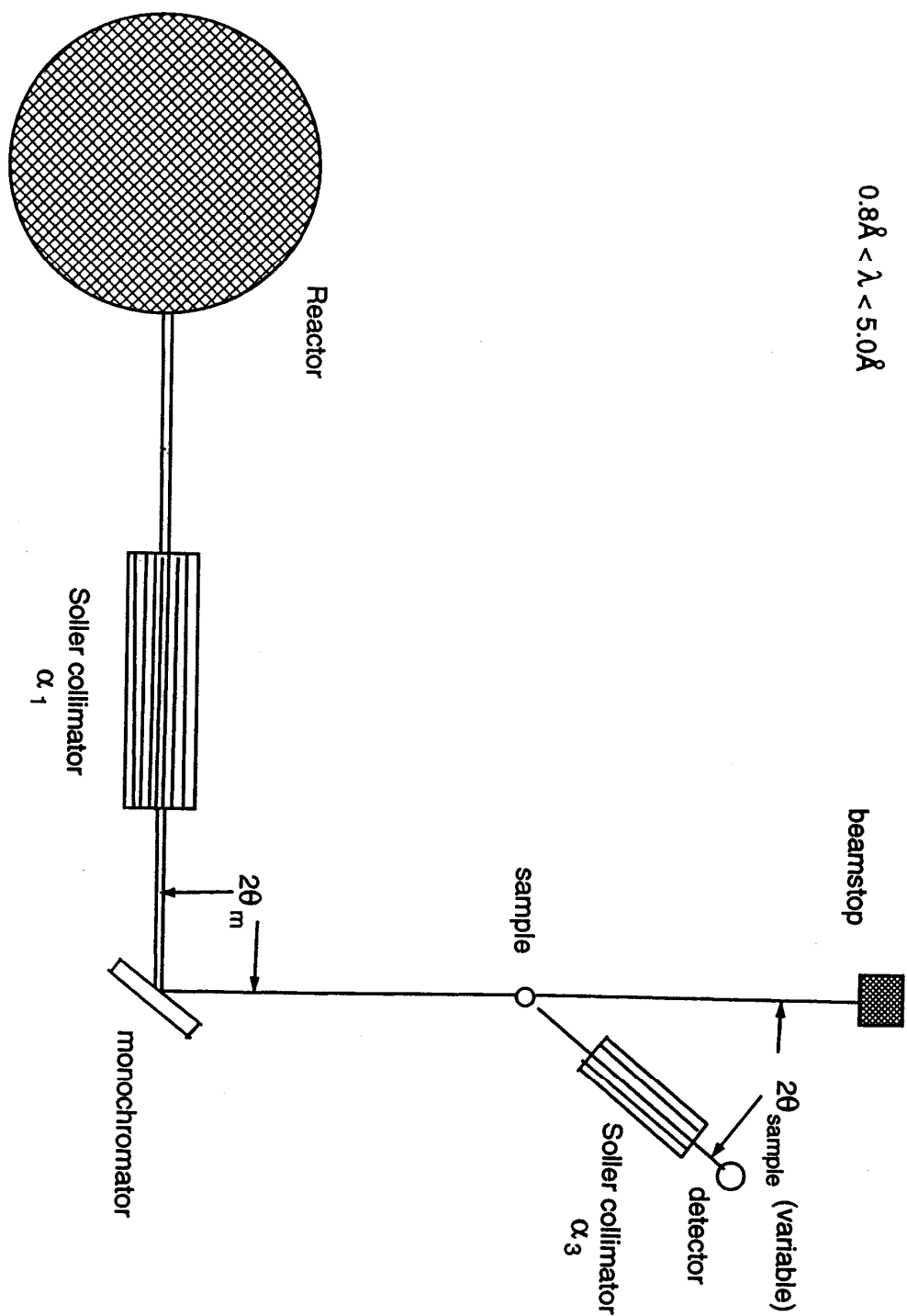


Figure 3.5b: Conventional Constant Wavelength Diffractometer.

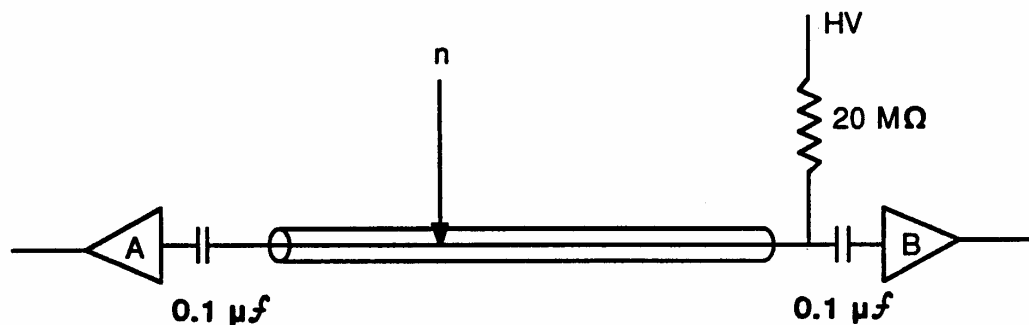


Figure 3.6: Position sensitive proportional counters.

After the reaction occurs, the two charged particles will be stopped by the argon gas, limiting the neutron to its local position, and creating electrons from the ionization of the fill gas. These electrons are accelerated to the anode by the applied electrical field and produce further ionization by electron impact. The small amount of CO₂ quenches the neutron induced discharge and limits the duration of the electronic pulse resulting from each neutron capture. The end result is the deposition of a negative charge onto the anode. The charge transports to the two ends of the anode to produce two pulses. The neutron event position can be determined by comparing the amplitudes of the two pulses.

For the MURR diffractometer, the sample size plays a role in the resolution of the diffractometer. A small size sample holder is used in our neutron scattering study; the sample holder is a thin wall vandum container, 3mm in diameter and 3 inch in height. Vandum has a very low coherent scattering cross section, accordingly its Bragg peaks will not appear in the scattering diagram.

It is advantageous to do the neutron scattering study with a small amount of sample (around 1 gram), first, a large amount of sample is not always available due to the cost; second, large size samples will not work if the sample contains large neutron absorption elements, like Sm, B, and Eu etc.

In order to reduce the background scattering from the sample environment, an oscillating radial collimator (ORC) is installed in front of the detectors. This collimator focus at the sample position, only neutrons scattered by the sample are allowed to pass through the collimator, and the neutrons scattered by the sample environment will be stopped. The oscillating movement will average the shadow of the collimator blades at every channel, and give a flat background. The transmission loss of ORC is lower than of the Soller collimators used in the conventional diffractometer.

The resolution of the MURR diffractometer is determined by the four factors. 1) monochromator lateral extension, 2) monochromator thickness, 3) sample size, 4) detector resolution. The four contributions are balanced at about 90° (2θ) to get the optimized performance. The peak shapes are Gaussian, and the Caglioti formula works well to model the dependance of the Full-Width-at-Half Maximum (FWHM) as a function of θ , so that the standard refinement code can be used without modifications.

In order to study magnetic structures and other properties at low temperature, a closed cycle refrigerator is used. The temperature range is 10K-300K. The sample is loaded in a cylindrical aluminum can filled with helium gas, to facilitate thermal conduction, and sealed by indium wires. The size of the aluminum can is 3 inches in diameter, the neutrons scattered by the wall of the aluminum can are stopped by the ORC, and the aluminum Bragg peaks will not appear in the neutron diagram.

A furnace (Figure 3.7) was built for the in-situ neutron diffraction studies. The sample is loaded inside a 2-inch quartz tube, which has an inlet and outlet for the gas input and output; the gas environments can be air, N₂, and He, etc.. There is a heater outside the tube, and the sample can be heated up to 900 °C. With the help of this furnace, we can do in-situ neutron diffraction studies to find the oxygen absorption and desorption at different temperatures and oxygen activity. Since the neutrons have to pass through the heater and quartz tube, the background in the low angle range is high, and the neutron intensity is reduced by about 40%. A new, well designed, furnace will be available in the near future. The tube will be of stainless steel, and two heaters will be used; one above the sample and the other below the sample, such that the shortcomings of the old furnace are overcome.

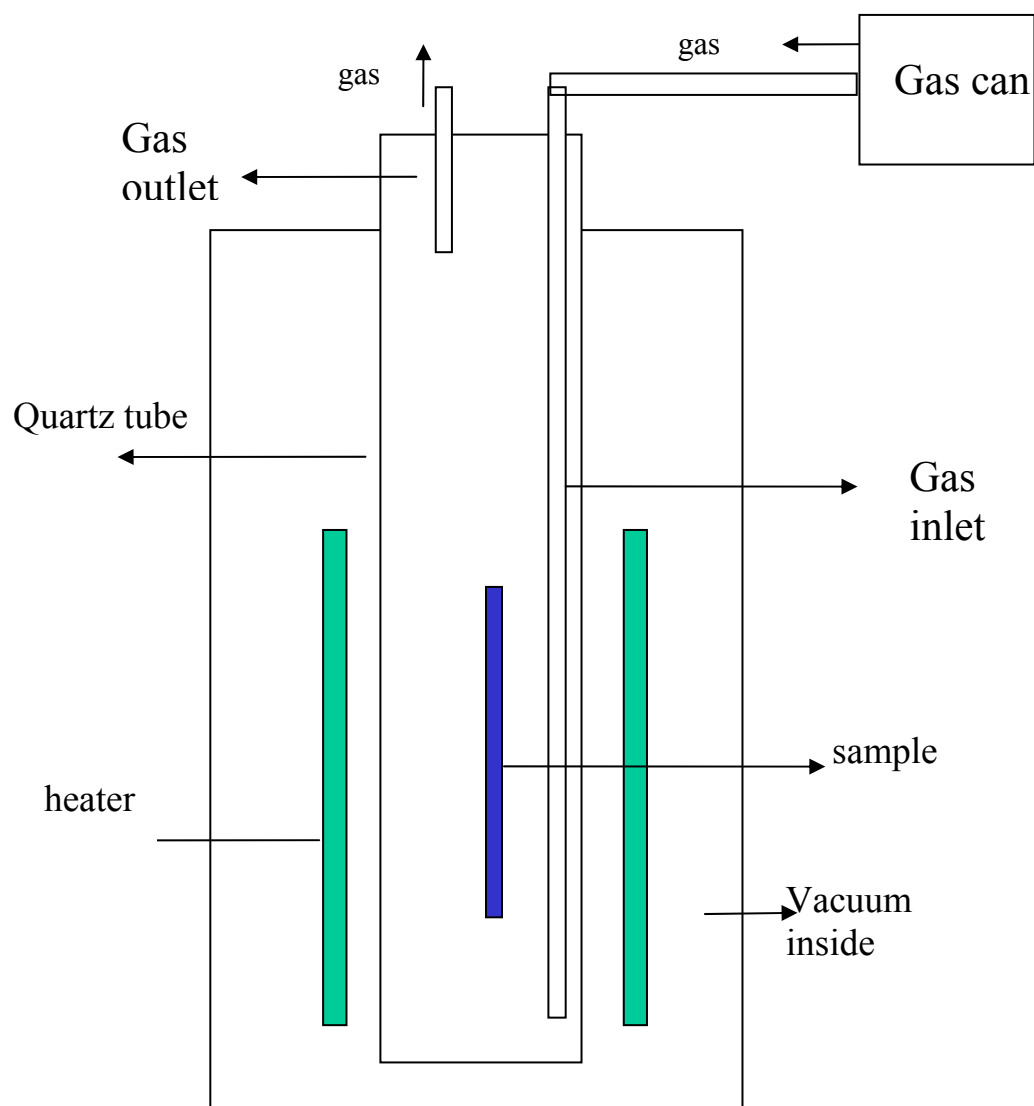


Figure 3.7: Schematic diagram of the neutron diffraction furnace.

Chapter 4 NEUTRON DIFFRACTION STUDIES ON $\text{ABO}_{3-\delta}$ (A=La, Sr; B=Fe, Co, Ni, Cu, Ti, Mn) PEROVSKITE MATERIALS USED IN SOFCs

In this chapter, we will report on neutron diffraction studies on the perovskite materials used in SOFCs. There are four perovskite series, 1) $\text{La}_{1-x}\text{Sr}_x\text{FeO}_{3-\delta}$ (LSF, $x=0.2$ and 0.4); 2) $\text{La}_{1-x}\text{Sr}_x\text{Fe}_{0.8}\text{Co}_{0.2}\text{O}_{3-\delta}$ (LSFC, $x=0.2$ and 0.4); 3) $\text{La}_{0.2}\text{Sr}_{0.8}\text{Fe}_{0.45}\text{Ti}_{0.55}\text{O}_{3-\delta}$ (LSFT); and 4) $\text{LaFe}_{1-x}\text{M}_x\text{O}_{3-\delta}$ (M=Mn, Cu, and Ni). The neutron diffraction studies were carried out at room temperature, low temperature and high temperature, in various gas environments, at the powder diffractometer at MURR.

4.1 $\text{La}_{1-x}\text{Sr}_x\text{FeO}_{3-\delta}$ ($x=0.2$ AND 0.4)

4.1.1 INTRODUCTION

The strontium-doped lanthanum ferrite $\text{La}_{1-x}\text{Sr}_x\text{FeO}_{3-\delta}$ has been intensively studied since it has good mixed conductivity at high temperature, and, thus, can be used as an oxygen membrane and is a candidate for the cathode of the SOFC. Undoped LaFeO_3 has a low electrical conductivity and oxygen vacancy concentration, but the electrical conductivity and oxygen vacancy concentration are increased by the substitution of La by Sr. M. V. Patrakeev et al.⁽³¹⁾ studied the electron / hole and ion transport in LSF in the oxygen partial pressure range of 10^{-19} -0.5 atm and temperatures between 750-950°C, and found that the electronic and ionic conductivity increase with Sr content and attain maximal values at $x=0.5$. The conductivity can be explained by electron hopping between Fe^{3+} and Fe^{4+} in the high P_{O_2} range and between Fe^{3+} and the Fe^{2+} in the low P_{O_2} range.

The LSF material is stable when the $P_{O_2} > 10^{-16}$ atm at 950°C; oxygen vacancies will appear at 600-800°C in air. The reaction between LSF (low Sr content) and YSZ is not significant for temperatures below 1200°C⁽³²⁾, and the TEC of $La_{0.8}Sr_{0.2}FeO_3$ in the 300-900°C range is $12.6 \times 10^{-6}/^{\circ}C$ ⁽³³⁾, close to the TEC of the YSZ⁽⁸⁾. LSF has shown excellent cathode performance at 750°C⁽³⁴⁾.

Mizusaki et al^(35, 36) studied the nonstoichiometry of oxygen and the defect structure of LSF at different oxygen partial pressures and temperatures. The major defects in LSF are oxygen vacancy $V_o^{\bullet\bullet}$, the substituted Sr_{La}' , the Fe^{2+} (Fe_{Fe}') and the Fe^{4+} (Fe_{Fe}^{\bullet}). These defects are not independent, they are constrained by the electroneutrality condition, which is expressed as follows:

$$[Sr_{La}'] + [Fe_{Fe}'] = 2[V_o^{\bullet\bullet}] + [Fe_{Fe}^{\bullet}] \quad (4.1)$$

where [] indicates the concentration of each species in number of moles for one mole of $La_{1-x}Sr_xFeO_{3-\delta}$. The value of $[Sr_{La}']$ is given by the nominal A-site composition x, and the oxygen vacancy concentration $[V_o^{\bullet\bullet}]$ is δ . The equation (4.1) can be expressed as:

$$x + [Fe_{Fe}'] = 2\delta + [Fe_{Fe}^{\bullet}] \quad (4.2)$$

In an oxidizing atmosphere, $[Fe_{Fe}^{\bullet}] \gg [Fe_{Fe}']$ holds, and equation (4.2) is simplified to:

$$x \cong 2\delta + [Fe_{Fe}^{\bullet}] \quad (4.3)$$

It is important to measure the oxygen vacancy concentration in LSF. It is well known that neutron powder diffraction coupled with Rietveld refinement can be used to

determine the oxygen vacancy concentration in many oxides, since the sensitivity of neutron scattering to oxygen is comparable to other atoms. However, the precision of such a determination is unknown, especially at low vacancy content. In addition, neutron diffraction is a very sensitive direct probe of the magnetic moment, and LSF exhibits magnetic ordering. If the magnetic moment of Fe is sensitive to the oxygen vacancy concentration, it can be used as an indirect probe of the oxygen vacancy concentration.

4.1.2 EXPERIMENTAL

The liquid-mixing method ⁽³⁷⁾ was used to synthesize fine LSF powder. An aqueous solution of Fe nitrate was first prepared and thermogravimetrically standardized. The lanthanum carbonate, and strontium carbonate were added to form a clear solution. Citric acid and ethylene glycol were added to the nitrate solution and then heated slowly to form a polymeric precursor, which was heated to 250°C to form an amorphous resin. This resin was calcined at 800°C for 8 hours. Bar shape specimens were prepared by uniaxial-pressing at 40 Mpa, followed by cold isostatic pressing at 310 Mpa. Bars were sintered on LSF substrates of the same composition at 1300°C with a heating rate of 3°C/min and a soak time of 4 hours. Specimens were rapidly quenched to room temperature after being annealed in air at temperatures ranging between 700-1500°C for 24 hours. We assume the oxygen nonstoichiometry of the quenched samples is the same as before quenching.

The neutron diffraction measurements were carried out at MURR at room temperature, low temperature (10K) and high temperature (up to 900°C) with or without air filling. The Rietveld method was used to refine the data by using the FULLPROF code, in which the magnetic ordering was modeled by a separate phase.

4.1.3 RESULTS AND DISCUSSION

a) $\text{La}_{0.6}\text{Sr}_{0.4}\text{FeO}_{3-\delta}$ (L6SF)

There are 10 samples slowly cooled (unquenched) or quenched in air from temperatures between 700°C-1500°C. All of them have been studied by neutron diffraction at room temperature and low temperature (10K). In order to study the oxygen stoichiometry change in air at high temperature, in-situ neutron diffraction studies were carried out at high temperature (up to 800°C) for the samples unquenched and quenched at 1500°C in air.

CRYSTALLOGRAPHIC STRUCTURE

The crystal structure of L6SF is rhombohedral with space group $R\bar{3}c$ when δ is zero⁽³⁸⁾. However, the structure can be affected by oxygen vacancies. In order to fit the data of quenched samples, three models are used, as follows:

Model 1: The first model is a rhombohedral structure with space group $R\bar{3}c$. The lattice parameters (hexagonal setting) are $a = b \approx \sqrt{2}a_p$, $c \approx 2\sqrt{3}a_p$, $\alpha=\beta=90^\circ$, and $\gamma=120^\circ$, where a_p is the lattice parameter of the basic cubic perovskite cell. In this model, the large cations $\text{La}^{3+}/\text{Sr}^{2+}$ occupy the 6a sites, the small cations $\text{Fe}^{3+}/\text{Fe}^{4+}$ occupy the 6b sites, and the oxygen ions occupy the 18e sites. The magnetic structure is modeled as having antiferromagnetic ordering with the moments in the hexagonal plane, which reverse between the positions (0, 0, 0) and (0, 0, 1/2). The magnetic model has the symmetry $R\bar{3}$, and the magnetic moments on the two sites are constrained to be equal.

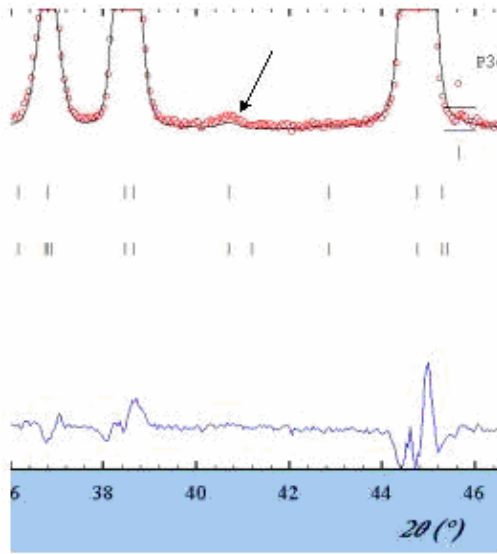
Model 2: This model is almost the same as model 1, but the oxygen occupies the 36f site rather than 18e site. The magnetic model is the same as employed in model 1. The occupancy of the 36f site is constrained to no more than half fully occupied.

Model 3: This model is a rhombohedral structure with space group $P\bar{3}c1$, and its unit cell is the same as model 1. $P\bar{3}c1$ is a subgroup of $R\bar{3}c$. In this model, the large cation site (6a) is split into two sites, 2a and 4d; the small cation site is split into 2b and 4d sites; and the oxygen site, 36f, is split into 3 12g sites. Two of them lie in crystallographically similar environments (they are close to each other), while the third one is in a different site. Because there is a high correlation between the occupancies of each of these oxygen sites, unconstrained refinement of the occupancy of each site leads to a small over-population of one site, reasonable total occupancy, and a large statistical uncertainty on the total occupancy. If, however, we constrained the occupancy of each site to be less than or equal to 0.5, and the two similar oxygen sites are constrained to have equal occupation, the statistical uncertainty on the total occupancy is dramatically reduced, to approximately 0.5%. The magnetic model is the same as employed for model 1.

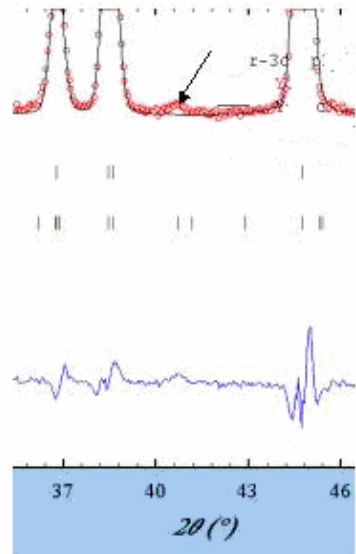
The goodness-of-fit (χ^2) of the 10 quenched and the unquenched specimen fitted with the three models are listed in Table 4.1. According to this table, model 1 works well for the unquenched and low temperature quenched samples only. For the high temperature quenched samples, the χ^2 is much larger than for the other two models. All three models give almost the same lattice parameters, unit cell volume, and magnetic moment, but the total oxygen occupancy is quite different. Model 3 gives the best fit and a more reasonable dependence of the vacancy concentration on the heat treatment. In

Table 4.1: The goodness-of-fit (χ^2) of the 10 quenched and unquenched specimens fit with the three models.

χ^2	No quench	700°C	800°C	900°C	1000°C	1100°C	1200°C	1300°C	1400°C	1500°C
Model 1	4.16	4.16	3.62	3.59	5.78	7.70	10.6	13.6	14.0	14.2
Model 2	4.12	4.07	3.47	3.28	4.62	5.45	6.89	6.43	7.18	6.47
Model 3	4.03	3.91	3.25	3.01	4.01	4.64	6.35	6.34	7.04	6.33



Refinement with $P3c1$ space group for the L6SF 1000°C air-quenched sample



Refinement with $R3c$ space group for the L6SF 1000°C air-quenched sample

Figure 4.1: Neutron diffraction pattern of L6SF for refined with model 1 and model 3. The red dots are the observed intensity, the black line is the calculated intensity, and the blue curve is the difference between the observed and the calculated intensity.

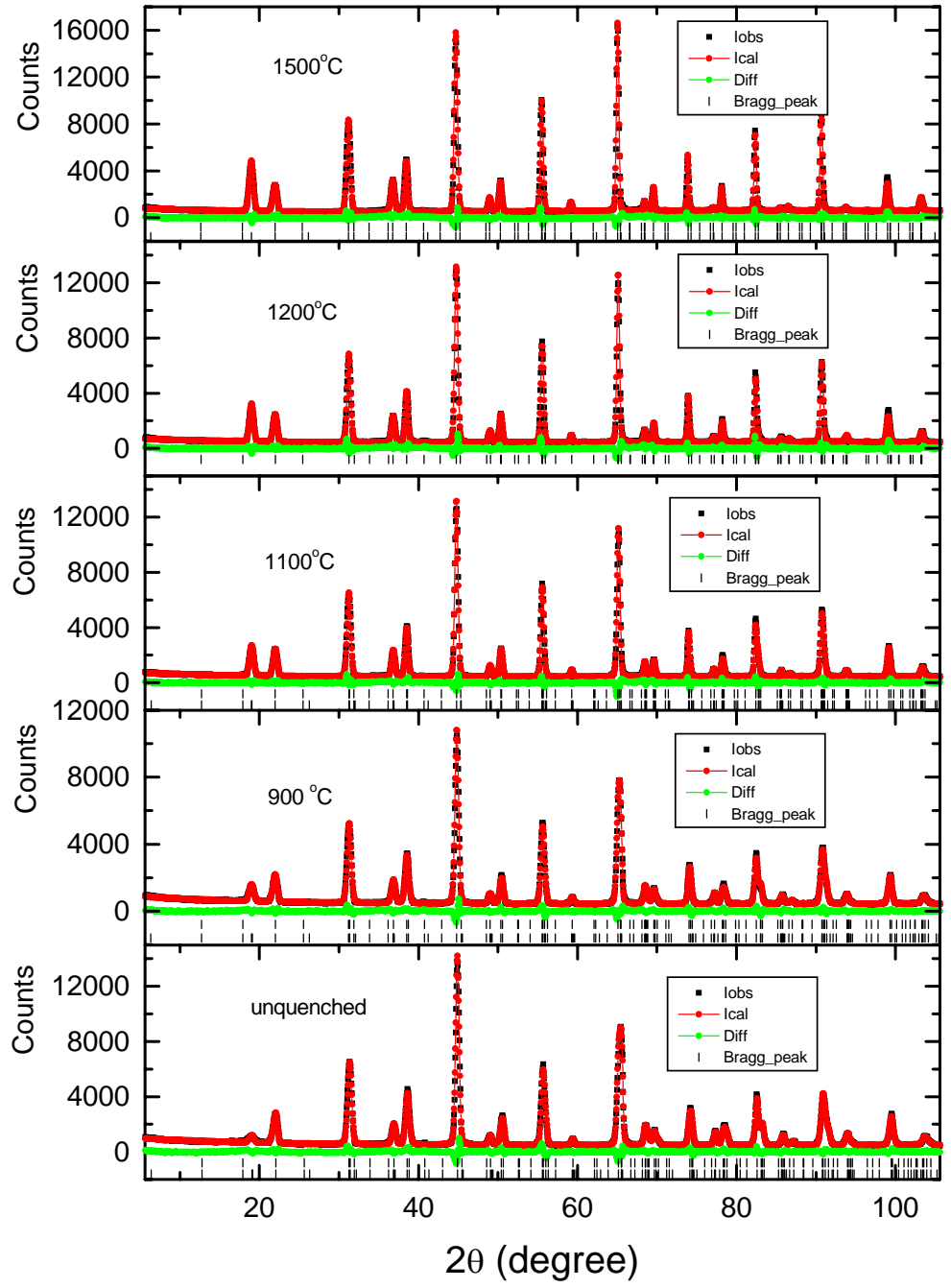


Figure 4.2: The neutron diffraction patterns of L6SF for unquenched, 900°C, 1100°C, 1200°C, and 1500°C quenched specimens. The black dots are the observed intensity, the solid red line is the calculated intensity, and their difference (green) is under them. The upper tic marks show Bragg positions for the nuclear phase, and the lower ones are for the magnetic phase.

addition, it matches a peak at about 41° , which is not fitted in the $R\bar{3}c$ symmetry (Figure 4.1). The results presented in this dissertation are those refined with model 3.

Some of the room temperature neutron diffraction patterns are illustrated in Figure 4.2. The first peak at low angle is a pure magnetic peak; its intensity increases with the quenching temperature, and some of the split peaks merge into one peak when the quench temperature is high.

Table 4.2 shows the crystal structure parameters at various quenching temperatures.

The maximum uncertainty on the total oxygen occupancy is about 0.018, which is larger

Table 4.2: L6SF refinement with constraints: fraction of O1 ≤ 0.5 . The fraction of O2 is the same as O3, and the sum of fractions of O2 and O3 ≤ 1.0 . Uncertainties in parenthesis are on the least significant digits.

Quench Temperature	a (Å)	c (Å)	Vol. (Å ³)	Total O	Mag.(RT) (μ_B)	δ
No Quench	5.52818(17)	13.44049(56)	355.72(2)	2.992(12)	1.31(3)	0.008(12)
700°C	5.52942(15)	13.44457(52)	355.99(2)	2.980(12)	1.42(2)	0.020(12)
800°C	5.52946(15)	13.44860(51)	356.10(2)	2.964(12)	1.67(2)	0.036(12)
900°C	5.53072(16)	13.46527(58)	356.71(2)	2.962(12)	2.07(2)	0.038(12)
1000°C	5.53352(17)	13.48996(65)	357.72(2)	2.936(16)	2.44(2)	0.064(16)
1100°C	5.53456(16)	13.50656(62)	358.30(2)	2.920(14)	2.72(2)	0.080(14)
1200°C	5.53091(41)	13.55839(190)	359.20(6)	2.872(18)	2.98(2)	0.128(18)
1200°C/24h	5.53026(40)	13.55285(191)	358.97(6)	2.856(14)	3.07(2)	0.144(14)
1300°C	5.53098(25)	13.55746(110)	359.18(4)	2.830(16)	3.26(2)	0.170(16)
1400°C	5.53510(29)	13.55662(126)	359.69(4)	2.818(16)	3.39(2)	0.182(16)
1500°C	5.53455(25)	13.55276(108)	359.52(4)	2.804(14)	3.44(2)	0.196(14)

than the oxygen vacancy concentration of the unquenched sample. It is difficult to measure the oxygen vacancy (δ) accurately by the direct crystallographic refinement when δ is small.

Figure 4.3 shows the change of lattice parameters a^* and c^* with the quenching temperature, in which a^* represents $a/\sqrt{2}$ and c^* represents $c/2\sqrt{3}$. The symmetry of L6SF quenched to room temperature from 700 to 1100°C remains rhombohedral, but the rhombohedral distortion becomes small when the quenching temperature is high. When the quenching temperature $T \geq 1200^\circ\text{C}$, the unit cell appears to be cubic. The presence of oxygen vacancies can relax the strain in the structure and reduce the distortion.

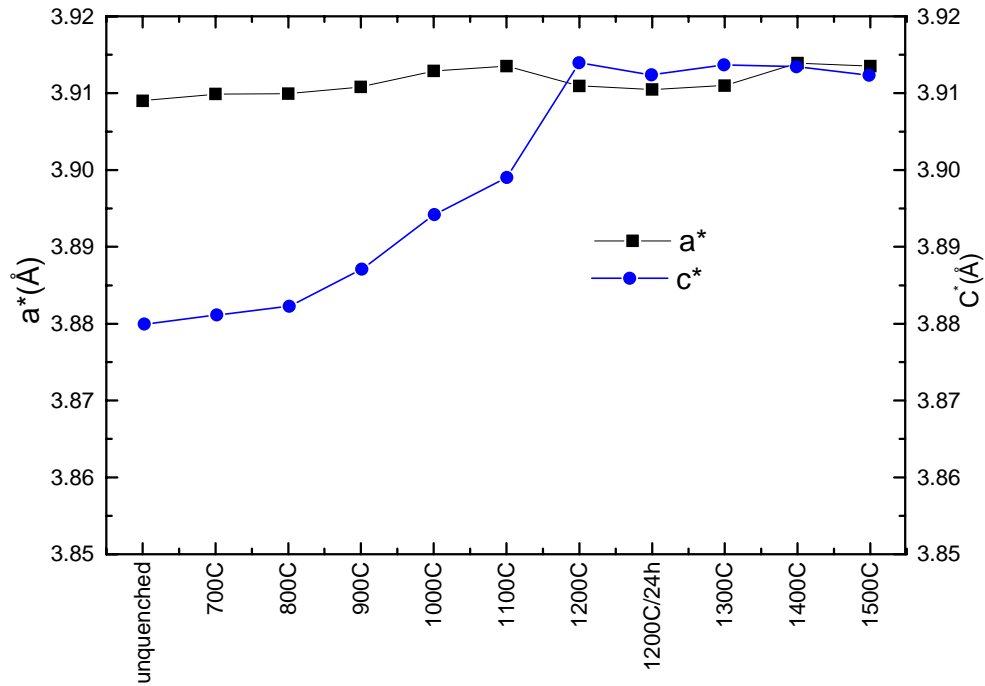


Figure 4.3: Lattice parameters of L6SF vs. quenching condition.

THE MAGNETIC MOMENT AND UNIT CELL VOLUME AT ROOM TEMPERATURE: CORRELATION WITH OXYGEN VACANCY CONCENTRATION

According to the direct refinement, the oxygen vacancy concentration increases from almost zero for the unquenched sample to about 0.2 for the 1500°C quenched sample (Figure 4.4a). The statistical uncertainty shows that the direct refinement is reliable only when the oxygen vacancy concentration is high.

The unit cell volume increases as the quenching temperature increases by a total of 3.8\AA^3 from the unquenched sample to the 1500°C quenched sample (Figure 4.4c). The statistical uncertainty in the unit cell volume is about 0.04\AA^3 . It shows that the unit cell volume can be a good metric for the determination of vacancy concentration. However, the unit cell volumes are relative due to the uncertainty in wavelength and sample position. Thus, the volumes of a series of samples can easily be compared, but the unit cell volume of a single specimen cannot be used to estimate its oxygen vacancy concentration. The small downturn in volume at the 1500°C quenched sample appears to be an artifact, since the data on the samples treated in different reducing atmospheres with vacancy concentration up to 9.6% show a continued increase in volume ⁽³⁸⁾.

The unit cell expansion associated with the formation of oxygen vacancies can be explained by: 1): The repulsive force arising between those mutually exposed cations when oxygen ions are absent in the lattice. 2): The increase in cation size due to the reduction of Fe ions from a high valence state to a lower valence state, which must occur concurrently with the formation of oxygen vacancies in order to maintain electrical neutrality.

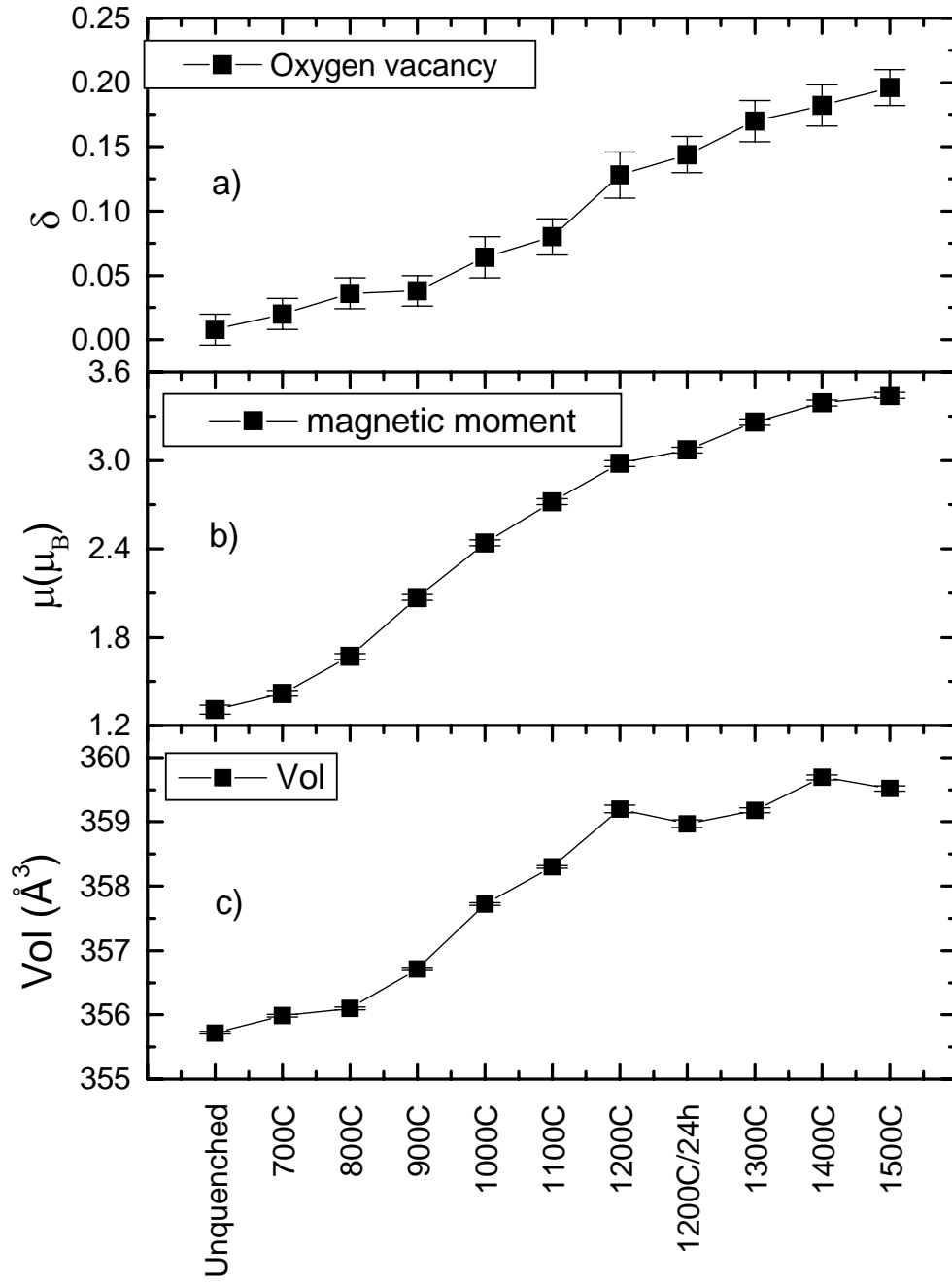


Figure 4.4: The changes of oxygen vacancy concentration, magnetic moment, and unit cell volume with the quench temperature for the L6SF samples.

The magnetic moment on the Fe sites at room temperature was found to increase from $1.31\mu_B$ for the untreated sample to $3.44\mu_B$ for the sample quenched from 1500°C (Figure 4.4b). The statistical uncertainty in the magnetic moment is less than 2.3% of the total moment, significantly less than the uncertainty in the vacancy concentration directly determined by the crystallographic refinement. The small increase in moment between the untreated and 700°C quenched samples probably reflects the production of a small oxygen vacancy concentration, outside the limit of the direct determination.

Figure 4.5 shows the magnetic moment and the unit cell volume of L6SF samples as a function of oxygen vacancy concentration. It appears that, in this range, the magnetic moment shows smoother behavior than does the unit cell volume, and may be the more reliable indirect measurement of the oxygen vacancy concentration.

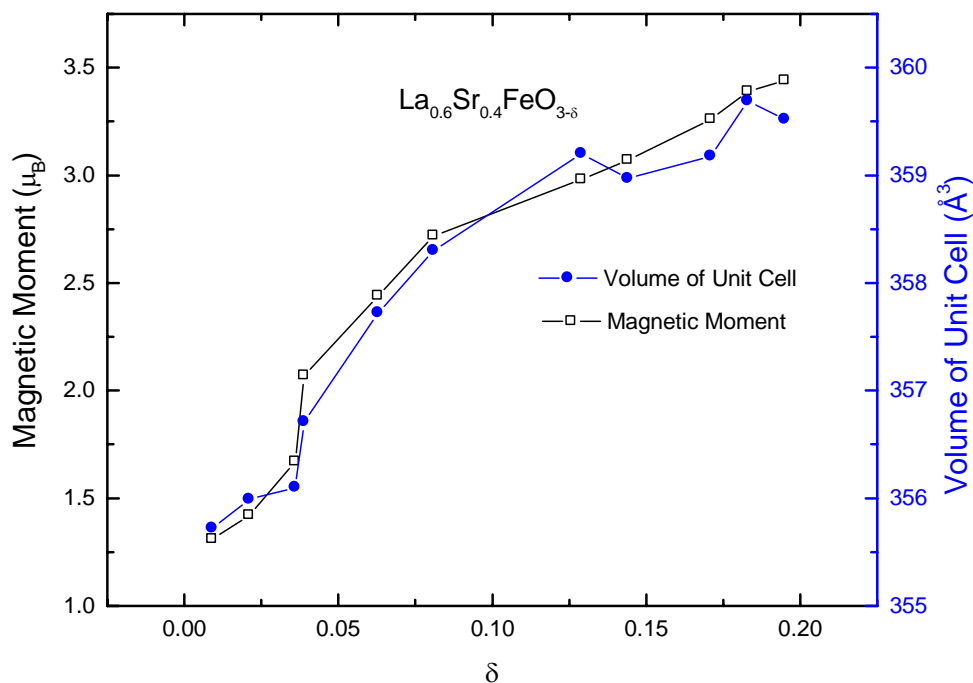


Figure 4.5: Magnetic moment and unit cell volume at room temperature vs. oxygen vacancy concentration for L6SF.

DIRECT DETERMINATION OF OXYGEN VACANCY CONCENTRATION FROM THE SATURATION MAGNETIC MOMENT

Fig. 4.6 shows the saturation moments, determined from the neutron powder diffraction measurement at 10K, as a function of oxygen deficiency. The saturation moment is linear with vacancy concentration, the highest deficiency, $\delta=0.2$, corresponds to a nearly pure Fe^{3+} state, and its value is about $3.8\mu_B$, which is equal to the magnetic moment of Fe^{3+} in LaFeO_3 . The moment when $\delta=0$ is about $2.33\mu_B$, and this value is about 60% of the magnetic moment of Fe^{3+} . This shows the magnetic moments at Fe sites are contributed by Fe^{3+} , and that the moment of Fe^{4+} is almost zero.

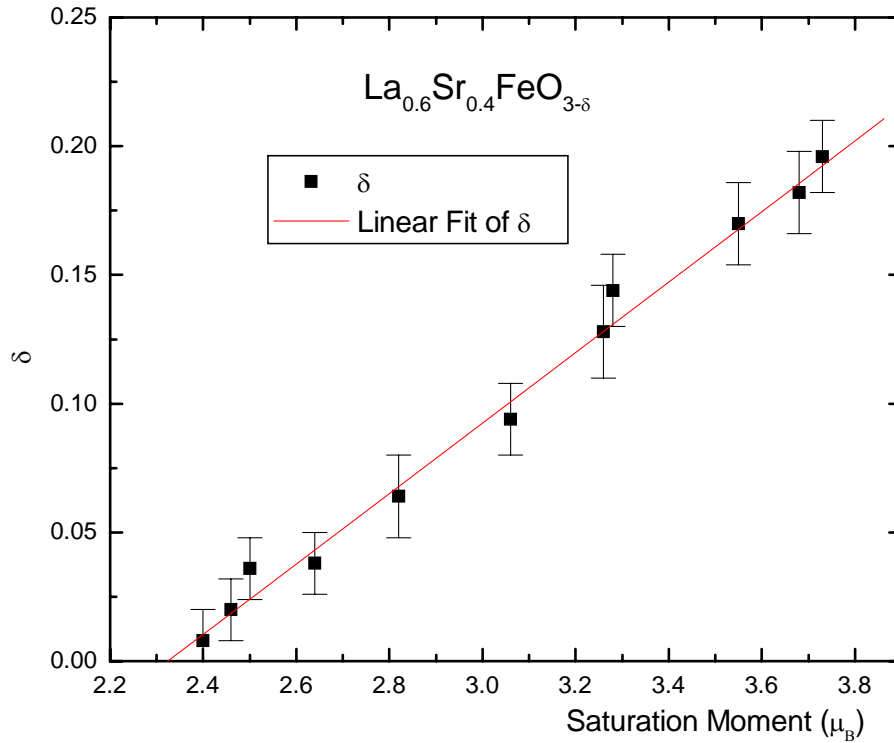


Figure 4.6: Oxygen vacancy concentration vs. saturation moment for L6SF.

For the ferrites with high La (50% or more) in an oxidizing environment, it is reasonable to assume that the Fe atoms are in the 3+ and 4+ charge states. The great difference between the saturation moments of the two Fe ions provide a direct determination of the ratio of the two ions and, thus, of the oxygen stoichiometry.

The magnetization as a function of temperature follows the Brillouin curve: saturated at low temperature and decreasing slowly up to about 70% of T_N and more rapidly as T_N is approached. Thus, according the ratio of the magnetic moment at room temperature to the moment at low temperature (Table 4.3), T_N is a little above room temperature when the quenching temperature is below 900°C.

Table 4.3: The magnetic moment of L6SF at different quenching temperature. The mol% of Fe^{3+} is calculated from the oxygen vacancy concentration.

T(°C)	No Quench	700	800	900	1000	1100	1200	1200/ 24h	1300	1400	1500
μ_{RT} (μ_B)	1.31	1.42	1.67	2.07	2.44	2.72	2.98	3.07	3.26	3.39	3.44
μ_{10K} (μ_B)	2.40	2.46	2.50	2.64	2.82	3.06	3.26	3.28	3.55	3.68	3.73
$\frac{\mu_{RT}}{\mu_{10K}}$	0.546	0.577	0.66 8	0.784	0.865	0.889	0.914	0.936	0.918	0.921	0.922
Fe^{3+} %	61.4	64	67.2	67.4	72.8	76	85.6	88.8	94	96.4	98.4

L6SF exhibits antiferromagnetic ordering below the Neel temperature. Comparing the magnetic moments at room temperature and 10K, the Neel temperature (T_N) increases with increasing oxygen vacancies along with the concentration of Fe^{3+} . The magnetic interactions between Fe ions, leading to magnetic ordering in this type of oxide, are predominantly superexchange; exchange that is mediated by polarization of oxygen ions lying between the Fe near neighbors. Since the Fe^{4+} ions have small or zero moments, the

exchange interactions in L6SF are expected to be dominated by the $\text{Fe}^{3+}\text{-O}^{2-}\text{-Fe}^{3+}$ interactions. This is the reason why T_N increases with increasing Fe^{3+} concentration, despite the loss of some bonding oxygen atoms.

There are many advantages in using the magnetic moment as a measure of vacancy concentration in L6SF. First, the saturation moment gives an absolute determination without establishing the room temperature curves, while the room temperature moment may be quickly and reliably determined if the correlations have been established. The uncertainty in magnetic moment is 2% at low vacancy concentration, decreasing to less than 1% when the moment is large, thus, the vacancy concentration should be known, by this indirect determination, to a precision of 1% or 2% over the range of interest. Second, the magnetic moment is not affected by the sample position and the model used for the refinement. Third, it is necessary to collect full data sets in order to accurately refine the vacancy concentration, while it is possible to extract the magnetic moment with the low angle range data only, and such data may be collected in as little as 1 hour. Of course, at very high vacancy concentration ($\delta > 0.2$), Fe^{2+} is expected to appear, with a smaller moment than Fe^{3+} , the average moment at Fe sites will become small as δ increases, and the linear relationship between the saturation moment and the oxygen vacancy will break down. At those concentrations, however, the direct determination of oxygen vacancy concentration by crystallographic refinement will become more precise.

On the other hand, collection of a full data set allows us to extract all the three determinations: volume, oxygen occupancy, and magnetic moment. These three determinations are essentially independent. The unit cell volume is based only on peak positions and not peak intensities, and uses the full data set. The oxygen occupancies

affect the intensities at all angles and especially uses the high angle data, while the magnetic moment is based primarily on the intensities of magnetic peaks at low angle. Thus use of neutron diffraction provides redundancy and cross checks on the oxygen vacancy determination.

IN-SITU NEUTRON DIFFRACTION STUDIES AT HIGH TEMPERATURE

Two L6SF samples were used for the in-situ neutron diffraction studies at high temperature. One is a 1500°C air-quenched sample, which was measured up to 507°C without air filling, slowly cooled to room temperature, and then heated up to 736°C with air filling. The other one is a slowly cooled sample, which was heated up to 800°C without air filling. The specimens were in a Pt mesh holder, which does not react with the sample. The specimens were studied inside the furnace discussed in the previous chapter. The data were collected above 28° (2θ) since the background of the furnace is high in the low angle range.

The patterns of all L6SF samples at high temperature can be fit by model 3. The results are listed in tables 4.4, 4.5 and 4.6. The crystal structure is rhombohedral with space group $P\bar{3}c1$. The magnetic ordering transition temperature for the 1500°C quenched sample is in the 345°C-394°C range, but for the slowly cooled sample, the transition temperature is a little above room temperature. Figure 4.7 is a typical neutron diffraction pattern. The 2nd phase is the Pt phase, its crystal structure is cubic with space group $Fm\bar{3}m$ and lattice parameter a is about 3.92Å, which is similar to the lattice parameter of the cubic structure of perovskite. The Pt peaks overlap with the perovskite peaks, and it is difficult to determine the correct oxygen occupation of the perovskite due

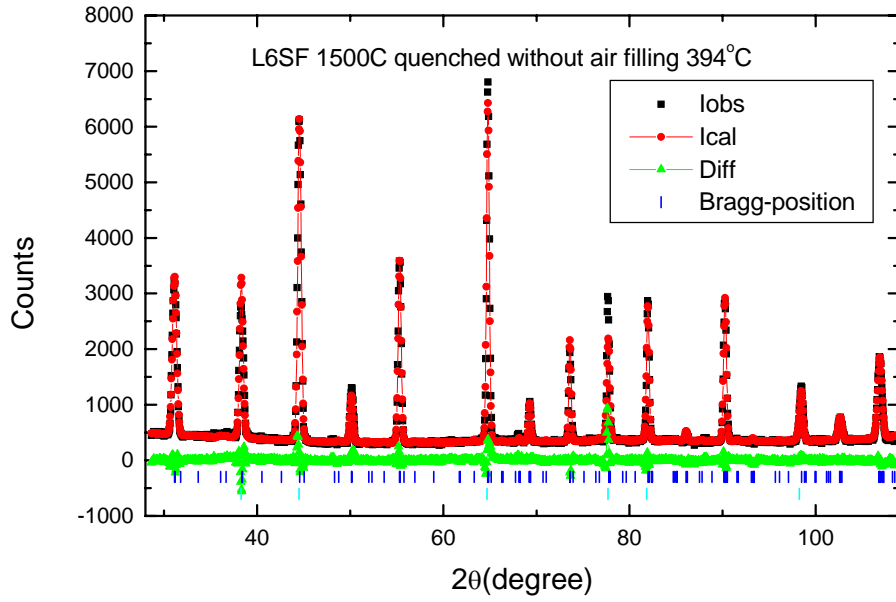


Figure 4.7: The neutron diffraction profile of L6SF 1500°C air quenched sample heated at 394°C without air filling.

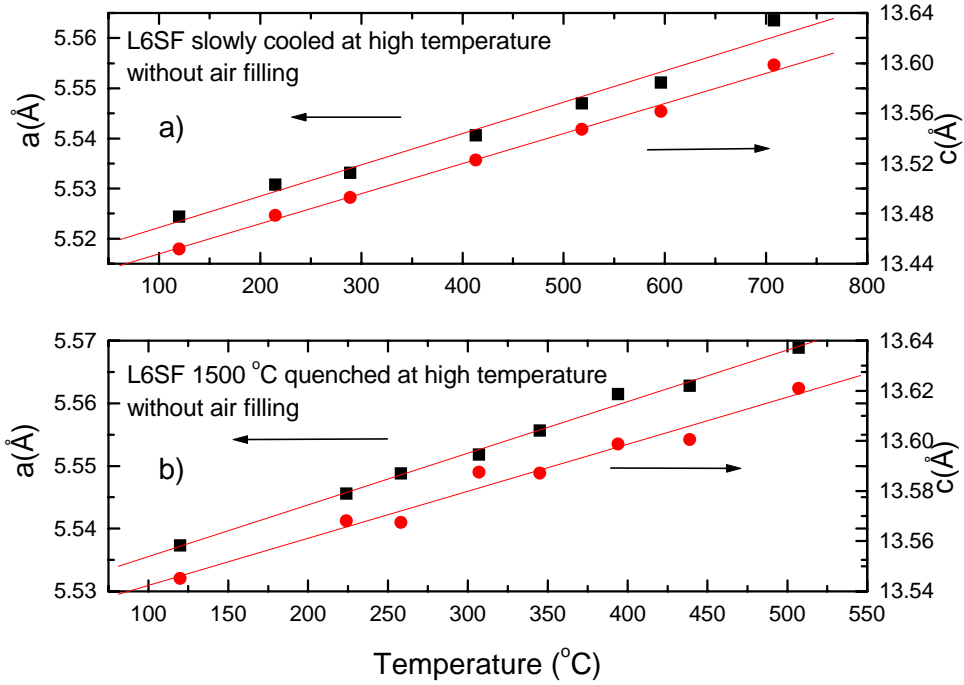


Figure 4.8: Temperature variation of lattice parameters a and c of the L6SF slowly cooled and 1500°C quenched samples.

to the texture of the Pt. The unit cell volume is a reliable index of the change in oxygen occupation since the sample position is the same in all measurements.

Figure 4.8 plots a and c as a function of measuring temperature. The lattice expansion can be calculated over the temperature range from 100 to 700°C for the L6SF slowly cooled sample and from 100 to 500°C for the 1500°C quenched sample. For the L6SF slowly cooled sample, the slopes for a and c vs. temperature are $6.3(4) \times 10^{-5}$ and $2.40(7) \times 10^{-4}$ respectively, and the thermal expansion coefficients for a and c lattice parameters are found to be $11.4 \times 10^{-6}/^{\circ}\text{C}$ and $17.8 \times 10^{-6}/^{\circ}\text{C}$. For the 1500 °C quenched sample, the slopes for a and c vs. temperature are $8.2(4) \times 10^{-5}$ and $1.9(1) \times 10^{-4}$ respectively, and the thermal expansion coefficients for a and c lattice parameters are found to be $14.8 \times 10^{-6}/^{\circ}\text{C}$ and $14.0 \times 10^{-6}/^{\circ}\text{C}$. Hence, the thermal expansion coefficient of the slowly cooled sample is anisotropic, but it is almost isotropic for the 1500°C quenched sample. This result is consistent with the crystal structure discussed above, the slowly cooled sample has rhombohedral distortion, but the 1500°C quenched sample is almost cubic due to the presence of oxygen vacancies.

Figure 4.9 shows the change of the volume vs. the temperature under three conditions. For the 1500°C quenched sample, measured in flowing N_2 (no air), the volume increased linearly with temperature up to 500 °C indicating that no oxygen was absorbed. The slope of the volume vs. temperature is 0.0158(3), and the volume thermal expansion coefficient is about $43.9 \times 10^{-6}/^{\circ}\text{C}$. For the slowly cooled sample, measured in N_2 , the volume increased linearly up to 600°C, then increased more rapidly above 600°C, which indicated that the oxygen loss began when the temperature exceeded 600°C. The slope in the linear region is 0.0133(3), and the average volume thermal expansion

coefficient is about $37.4 \times 10^{-6}/^{\circ}\text{C}$. The 1500°C quenched sample was studied with air flowing through the furnace. Its volume increased linearly up to 303°C , indicating its oxygen vacancy is not changed. In the temperature range from 303°C - 655°C , its volume is almost unchanged, indicating the oxygen uptake. Above the 655°C , its volume increased more rapidly than the linear increases of the slowly cooled sample, indicating oxygen loss.

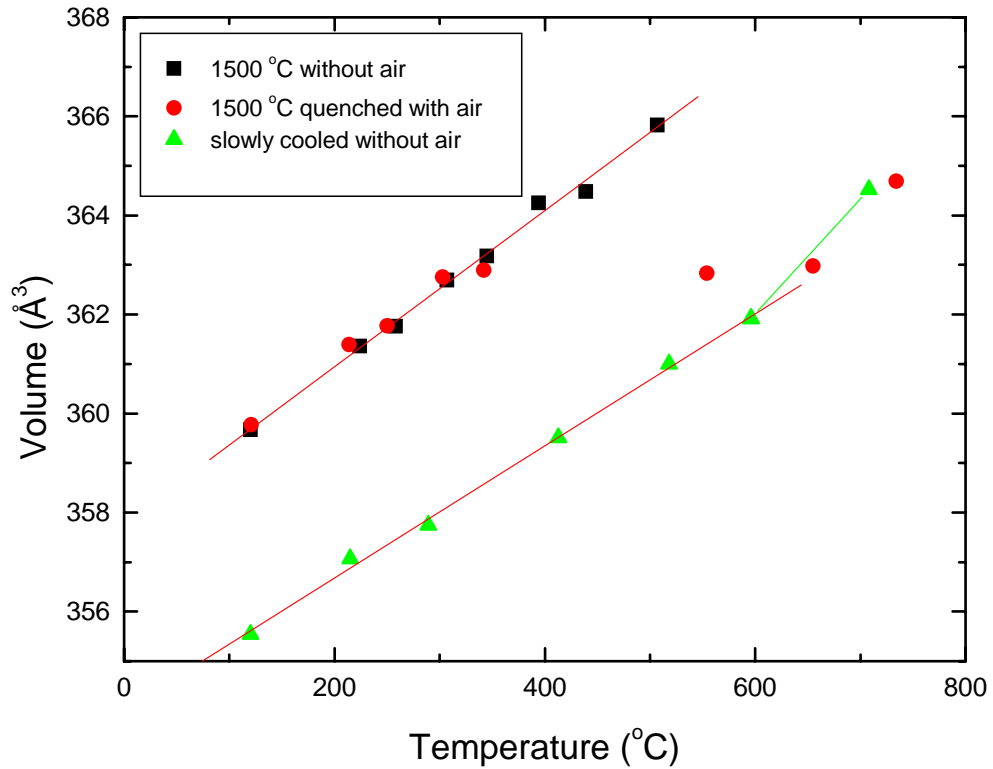


Figure 4.9: The unit cell volume of L6SF samples quenched from 1500°C and slowly cooled at high temperature with/without air flowing.

The average volume expansion coefficient α is related to the linear expansion coefficient a by $\alpha = 3a$ if a is small. This results in a linear expansion coefficient of $14.6 \times 10^{-6}/^{\circ}\text{C}$ and $12.5 \times 10^{-6}/^{\circ}\text{C}$ for the 1500°C quenched and slowly cooled samples respectively. The presence of oxygen vacancies increases the linear expansion coefficient.

Table 4.4: L6SF sample quenched in air from 1500°C , measured as a function of temperature and without air filling. The $\text{RT}^{(1)}$ is a measurement at room temperature before the sample was heated, and the $\text{RT}^{(2)}$ is the measurement after the sample was slowly cooled to room temperature. The measurements at room temperature were run with the specimen outside the furnace.

T ($^{\circ}\text{C}$)	a (\AA)	c (\AA)	Volume (\AA^3)	Occ. (O)	μ (μ_{B})
$\text{RT}^{(1)}$	5.53412(23)	13.54368(99)	359.224(34)	2.792(16)	3.54(2)
120	5.53729(26)	13.54505(120)	359.672(40)	2.774(24)	3.23(4)
224	5.54557(30)	13.56812(139)	361.362(46)	2.756(26)	2.62(4)
258	5.54878(25)	13.56743(116)	361.762(39)	2.874(34)	2.41(5)
307	5.55179(36)	13.58757(167)	362.693(56)	2.970(32)	2.02(6)
345	5.55562(23)	13.58719(109)	363.182(36)	2.650(24)	1.47(6)
394	5.56146(25)	13.59869(118)	364.255(39)	2.508(104)	0
439	5.56282(22)	13.60060(102)	364.484(34)	2.700(26)	0
507	5.56888(28)	13.62096(133)	365.826(44)	2.716(26)	0
$\text{RT}^{(2)}$	5.53526(31)	13.54296(141)	359.352(47)	2.752(20)	3.45(3)

Table 4.5: L6SF sample quenched in air from 1500°C, measured as a function of temperature and with air filling. The RT is the measurement outside the furnace after the sample was slowly cooled to room temperature.

T (°C)	a (Å)	c (Å)	Volume (Å ³)	Occ. (O)	μ (μ _B)
121	5.53866(20)	13.54225(82)	359.775(29)	2.8	3.29(4)
214	5.54652(23)	13.56449(98)	361.389(34)	2.8	2.79(5)
250	5.54890(20)	13.56703(81)	361.767(28)	2.8	2.54(5)
303	5.55421(20)	13.57811(80)	362.756(28)	2.8	2.18(5)
342	5.55434(23)	13.58260(95)	362.893(33)	2.8	1.73(7)
554	5.55535(46)	13.57538(220)	362.832(72)	2.8	0
655	5.55658(22)	13.57498(105)	362.982(35)	2.846(24)	0
734	5.56440(25)	13.60079(123)	364.696(40)	2.806(24)	0
RT	5.52836(15)	13.41870(44)	355.168(18)	3.014(18)	1.25(3)

Table 4.6: L6SF slowly cooled sample measured as a function of temperature. The room temperature measurement is outside the furnace.

T (°C)	a (Å)	c (Å)	Volume (Å ³)	Occ. (O)	μ (μ _B)
RT	5.52202(16)	13.43174(57)	354.698(21)	2.992(8)	1.38(2)
120	5.52441(22)	13.45182(84)	355.536(30)	2.988(20)	0
215	5.53078(22)	13.47847(88)	357.063(31)	2.996(20)	0
289	5.53312(23)	13.49276(97)	357.744(33)	2.944(20)	0
413	5.54059(26)	13.52288(125)	359.510(41)	2.936(20)	0
518	5.54701(33)	13.54735(169)	360.997(55)	2.884(24)	0
596	5.55115(35)	13.56153(175)	361.913(57)	2.840(24)	0
708	5.56353(34)	13.59870(171)	364.526(56)	2.836(24)	0

b) $\text{La}_{0.8}\text{Sr}_{0.2}\text{FeO}_{3-\delta}$ (L8SF)

There are six specimens of L8SF quenched in air in the temperature range of 800°C-1500°C. All of them have been studied by neutron diffraction at room temperature. The in-situ neutron diffraction study has been done for one L8SF bar-shaped specimen up to about 900°C, the limit of the quartz furnace tube.

NEUTRON DIFFRACTION STUDIES OF THE AIR-QUENCHED SPECIMENS AT ROOM TEMPERATURE

The crystal structure of all the L8SF specimens is orthorhombic, with space group Pbnm, lattice parameters are $a \approx \sqrt{2}a_p$; $b \approx \sqrt{2}a_p$; $a \neq b$; $c \approx 2a_p$; $\alpha=\beta=\gamma=90^\circ$; where a_p is the lattice parameter of the cubic perovskite. There are 4 formula units per unit cell. The large cations $\text{La}^{3+}/\text{Sr}^{2+}$ are at 4c sites, the small cations $\text{Fe}^{3+}/\text{Fe}^{4+}$ are at 4a sites. The oxygen ions, however, are on two sites 4c and 8d. The neutron diffraction pattern of the sample quenched in air from 800°C is illustrated in Figure 4.10. The first peak is purely magnetic, its intensity is much bigger than the L6SF sample quenched under the same conditions.

Table 4.7 shows the results of the L8SF samples quenched in air from 800°C-1500°C. the direct refinement shows that there are no oxygen vacancies when the quench temperature is below 1000°C, the magnetic moments are about $3.0\mu_B$, and there is a very small increase in the unit cell volume from 240.34 to 240.48 Å³. When the quench temperature is above 1000°C, oxygen vacancies appear, and the magnetic moment increases slowly from 3.0 to $3.3\mu_B$. The highest oxygen vacancy is about 2% for the highest quenching temperature, but its unit cell volume still shows almost no change, increasing to 240.96 Å³. It is apparent that it is much more difficult to produce oxygen

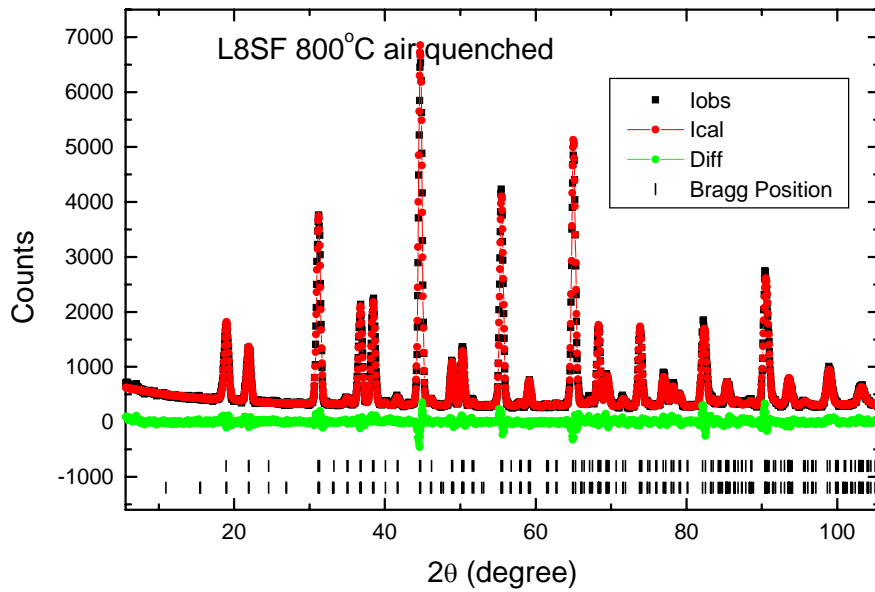


Figure 4.10: The neutron diffraction pattern at room temperature of L8SF sample quenched from 800°C.

Table 4.7: Refinement results for L8SF samples quenched in air from 800°C to 1500°C. The A and B sites are fully occupied, and the ratio of La/Sr is fixed as 0.8/0.2.

Quench	a (Å)	b (Å)	c (Å)	Vol (Å ³)	Total O	Mag (μ _B)	δ
800°C	5.54992(42)	5.51978(42)	7.84544(68)	240.340(33)	2.992(14)	3.03(2)	0.008(14)
900°C	5.54946(53)	5.52044(56)	7.84982(85)	240.483(42)	2.990(16)	2.97(3)	0.010(16)
1000°C	5.55041(47)	5.52166(48)	7.85090(74)	240.610(37)	2.988(16)	3.12(3)	0.012(16)
1200°C	5.55288(39)	5.53091(40)	7.84244(72)	240.861(33)	2.954(12)	3.17(2)	0.046(12)
1300°C	5.55178(38)	5.53002(37)	7.83581(69)	240.570(31)	2.942(12)	3.24(2)	0.058(12)
1500°C	5.55663(34)	5.53374(33)	7.83631(62)	240.958(28)	2.940(12)	3.31(2)	0.060(12)

vacancies in L8SF than in the L6SF samples since the La content is high. In addition, it is clear that the Neel temperature of L8SF samples is well above room temperature and, thus, the effect of vacancy concentration on the room temperature magnetic moment is modest. The magnetic moment could be made to be a more sensitive measure of vacancy concentration by carrying out these measurements at higher temperature. It should be quite easy to determine the optimum measuring temperature by following the temperature dependence of the magnetization and choosing one where the moment of the low temperature quenched sample is in the neighborhood of $1\mu_B$. Then we might expect to see the moment increase strongly with vacancy concentration.

IN-SITU NEUTRON DIFFRACTION STUDY OF L8SF HEATED UP TO 900°C WITH AIR FILLING

In-situ neutron diffraction studies of a L8SF bar-shaped sample was carried out from room temperature (31°C) to 900°C in about 100°C steps without using a sample holder. The crystal structure is orthorhombic with space group Pbnm when the temperature is below 394°C, as are the quenched samples. When the temperature is above or equal to 394°C, there is a phase change; the crystal structure changes to rhombohedral with space group $\bar{P}3c1$. The neutron patterns at or above 394°C can be fitted by the model 3, which was described in the L6SF section. Figure 4.11 illustrates the neutron patterns at 190°C, 292°C, and 394°C. Many small peaks of the orthorhombic structure, such as the peaks at 34.7° and 41.6°, disappear in the rhombohedral structure, and some peaks merge together in the orthorhombic samples structure, such as the peaks at 65°, 82.4°, and 90.5°. These are separated into two peaks in the rhombohedral structure. All of these changes indicate the structure change above 394 °C.

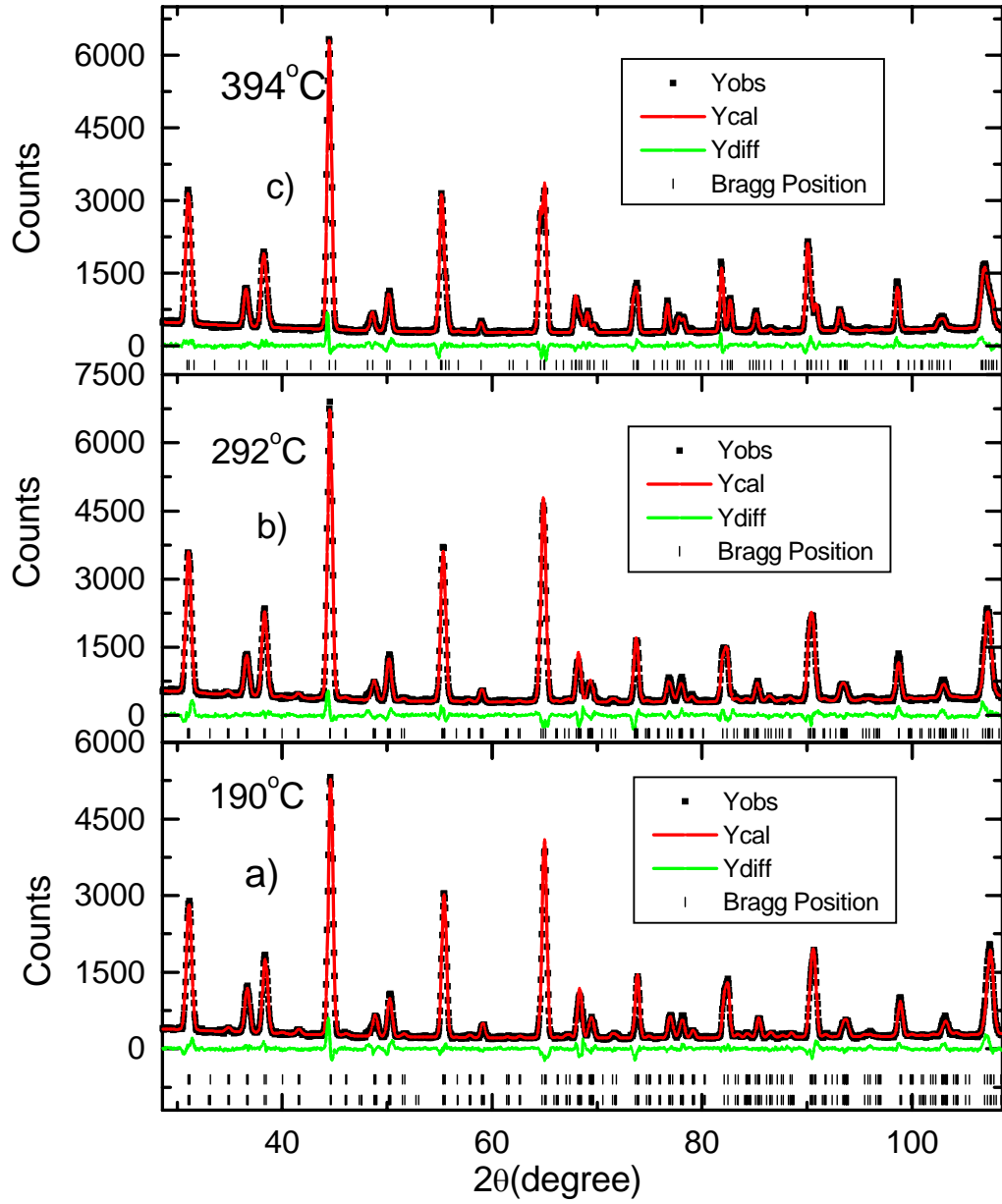


Figure 4.11: The neutron diffraction patterns of L8SF at 190°C, 292°C, and 394°C. The magnetic ordering disappears at 292°C, and the structural phase transition occurs below 394°C.

Table 4.8 gives the results the in-situ study of L8SF at high temperature with flowing air. The magnetic moment decreases as the temperature increases and the magnetic ordering disappears at 292°C, the magnetic phase transition temperature. The total oxygen occupancies are a little above 3, indicating that there are no oxygen vacancies in the whole temperature range (or the oxygen vacancy is too small to be detected by the direct refinement). The lattice parameters and the unit cell volume increase as the temperature increases. A phase change occurs in the temperature range between 292°C and 394°C.

Table 4.8: Refinement results for L8SF at high temperature with air filling.

T (°C)	Space group	a (Å)	b (Å)	c (Å)	Total O	Moment (μ_B)	Vol. (Å ³)
31	Pbnm	5.54274(39)	5.51576(40)	7.81062(56)	3.010(18)	2.90(7)	238.790(30)
92	Pbnm	5.54538(41)	5.51750(42)	7.81381(57)	3.028(20)	2.53(7)	239.076(31)
190	Pbnm	5.55219(36)	5.52186(38)	7.82231(50)	3.052(18)	1.6(1)	239.820(27)
292	Pbnm	5.55903(42)	5.52506(42)	7.83417(54)	3.004(18)	0	240.619(31)
394	P-3c1	5.56180(18)		13.50134(56)	3.032(16)	0	361.692(22)
500	P-3c1	5.56805(18)		13.52827(58)	3.036(16)	0	363.228(23)
596	P-3c1	5.57399(18)		13.55316(58)	3.004(16)	0	364.673(22)
702	P-3c1	5.57803(18)		13.57392(62)	3.032(16)	0	365.761(24)
790	P-3c1	5.58728(18)		13.60497(62)	3.024(16)	0	367.815(24)
898	P-3c1	5.59740(24)		13.63818(86)	3.016(20)	0	370.050(32)

Figure 4.12 shows the lattice parameters of the two phases as a function of temperature. The lattice expansion can be calculated over the temperature ranges from 31°C to 292°C for the orthorhombic phase and from 394°C to 898°C for the rhombohedral phase. The thermal expansion coefficients for the a , b , and c lattice parameters of the orthorhombic phase were found to be $11.3 \times 10^{-6}/^{\circ}\text{C}$, $6.5 \times 10^{-6}/^{\circ}\text{C}$, and $11.6 \times 10^{-6}/^{\circ}\text{C}$ respectively. The thermal expansion coefficients for the a , and c lattice parameters of the rhombohedral phase were found to be $12.7 \times 10^{-6}/^{\circ}\text{C}$ and $20.1 \times 10^{-6}/^{\circ}\text{C}$ respectively. The L8SF is anisotropic.

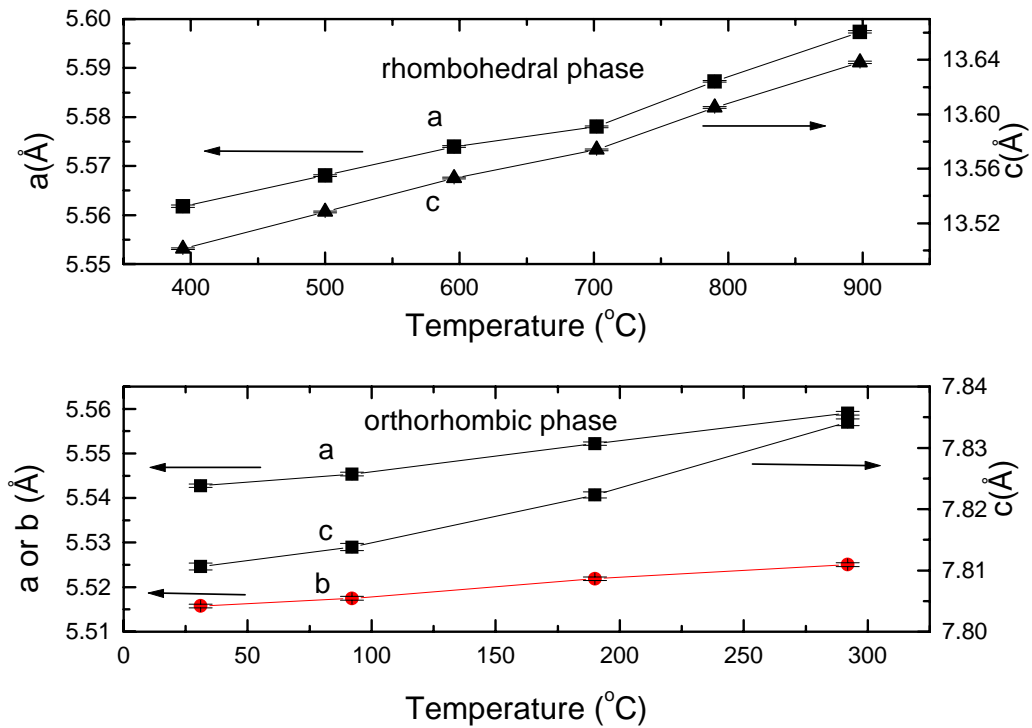


Figure 4.12: Lattice Lattice parameters of L8SF vs. temperature.

Figure 4.13 shows the unit cell volume per formula unit as a function of temperature. The volume expansion is roughly linear in each phase, while the volume expansion coefficients are $29.82 \times 10^{-6}/^{\circ}\text{C}$ and $44.79 \times 10^{-6}/^{\circ}\text{C}$ for the orthorhombic and rhombohedral phases respectively. Therefore, the linear TECs are $9.94 \times 10^{-6}/^{\circ}\text{C}$ and $14.93 \times 10^{-6}/^{\circ}\text{C}$. The linear thermal expansion coefficient for the rhombohedral phase is significantly larger than that of the orthorhombic phase.

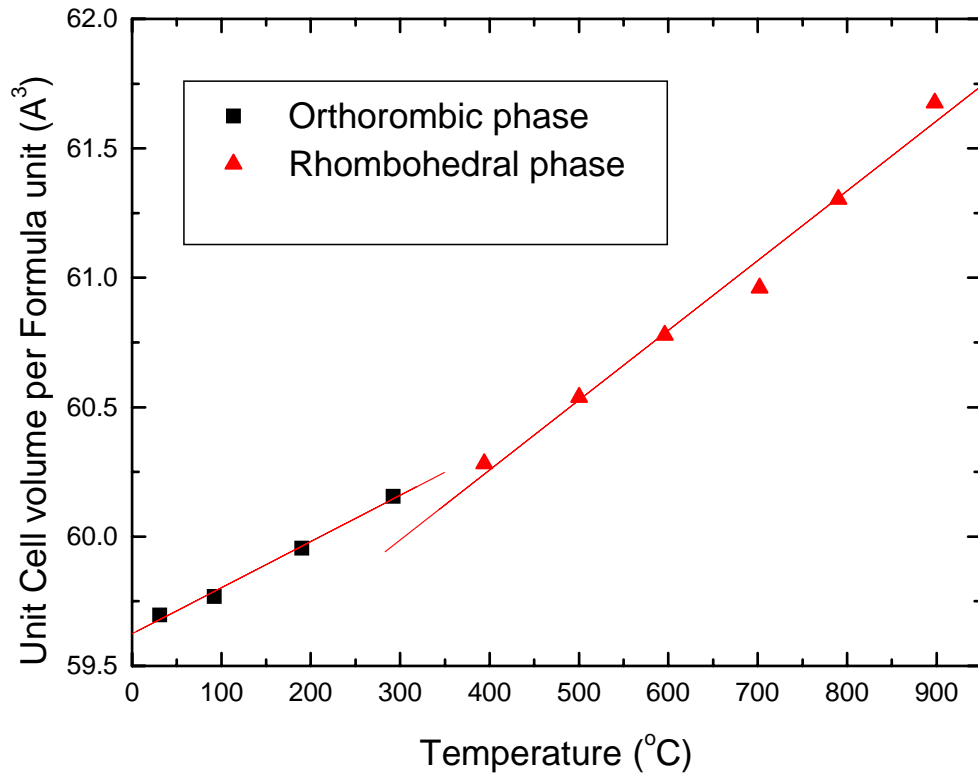


Figure 4.13: The unit cell volume per formula unit of L8SF, as a function of temperature.

4.1.4 CONCLUSIONS

L6SF specimens quenched from 700-1500°C exhibit antiferromagnetic ordering at room temperature. The unit cell volume and the oxygen vacancy concentrations increase with increasing quenching temperature. The magnetic ordering is dominated by the Fe^{3+} - O^{2-} - Fe^{3+} interactions, and the Fe^{3+} concentration increases with increasing oxygen vacancy δ . Thus, the magnetic moment and the Neel temperature increase with increasing oxygen vacancy. The saturation moment, determined by neutron diffraction at 10K, is linear with the oxygen vacancy concentration(δ). At high temperature with air flowing, L6SF will absorb oxygen at 303°C-655°C and then lose oxygen when temperature is above 655°C. The presence of oxygen vacancies increases the thermal expansion coefficient.

L8SF exhibits antiferromagnetic ordering at room temperature. It is more difficult to create oxygen vacancies for L8SF than L6SF since the Sr content is small. At high temperature there is a phase transition below 394°C, the thermal expansion coefficient of the rhombohedral phase is higher than the orthorhombic phase.

Neutron diffraction measurement coupled with refinement by the Rietveld method appears to be a reliable, redundant method for determining the oxygen vacancy in L6SF. The unit cell volume, the oxygen occupation, and the magnetic moment can be used to determine the oxygen vacancy. The unit cell volume can be affected by the sample position, but the magnetic moment at room temperature can provide the data more accurately than the other two parameters. The saturation moment (μ_{10K}) is an even more powerful tool which can be used to determine the vacancy concentration.

4.2 LaFe_{1-x}M_xO₃ (M=Ni, Mn, AND Cu)

4.2.1 INTRODUCTION

Besides the A site doping with aliovalent cations in ABO₃ perovskites, B site doping with different transition metals is another way to alter the physical properties of ABO₃ since the electronic conductivity and magnetic ordering are determined by the B site ion. The perovskite-type ABO₃ compositions containing more than two types of transition metal ions on the B site are always more reactive (for oxygen reduction) than those with only one type of transition metal ion.⁽³³⁾ Reiichi Chiba et al.⁽³⁹⁾ investigated the properties of La(Ni-M)O₃ (M=Al, Cr, Mn, Fe, Co) and found that LaNi_{0.6}Fe_{0.4}O₃ satisfied the important requirements for a cathode of IT SOFC. It has higher electronic conductivity (580 S/cm at 800°C) than that of La_{0.8}Sr_{0.2}MnO₃ (180 S/cm), and its average thermal expansion coefficient from 30 to 1000°C (11.4x10⁻⁶K⁻¹) is closer to that of YSZ (10x10⁻⁶K⁻¹) than La_{0.8}Sr_{0.2}MnO₃ (12.0x10⁻⁶K⁻¹). The Cu doping at the B site of La_{0.8}Sr_{0.2}FeO₃ was studied by S. Simner et al.⁽⁴⁰⁾, and they found 2-5 atm% Cu doping can significantly enhance sinterability below 1000°C. Low temperature sintering can reduce the reaction between the La_{0.8}Sr_{0.2}FeO₃ and YSZ.

In this work, neutron diffraction was used to study the crystal structure and magnetic properties of LaFe_{1-x}M_xO₃ (M=Mn, Ni, and Cu) at room temperature, low temperature, and high temperature.

4.2.2 EXPERIMENTAL

The glycine nitrate process was used to prepare the oxide powders.⁽⁴¹⁾ Nitrate solutions were standardized using thermogravimetric analysis. The A/B ratio was set at 1.00. The powder samples were calcined at 1000°C for one hour in air for the

$\text{LaFe}_{1-x}\text{Ni}_x\text{O}_3$ and $\text{LaFe}_{1-x}\text{Mn}_x\text{O}_3$ and 1000°C for two hours for the $\text{LaFe}_{1-x}\text{Cu}_x\text{O}_3$ samples. The $\text{LaFe}_{0.4}\text{Ni}_{0.6}\text{O}_3$ bar shaped samples were sintered from 800°C to 1400°C in order to study the stability at high temperature. The neutron diffraction study was carried out at the University of Missouri-Columbia Research Reactor (MURR), and neutron diffraction data were refined by using the FULLPROF program.

4.2.3 RESULTS AND DISCUSSION

a) $\text{LaFe}_{1-x}\text{Ni}_x\text{O}_3$ ($x=0, 0.2, 0.4, 0.5, 0.8$)

The neutron diffraction patterns of the $\text{LaFe}_{1-x}\text{Ni}_x\text{O}_3$ ($x=0, 0.2, 0.4, 0.5, 0.8$) series are shown in Fig. 4.14. All of them are single phase. It means that the LaFeO_3 and LaNiO_3 can form a continuous series of solid solutions without the formation of intermediate phases. The iron-rich compounds ($x<0.5$) have an orthorhombic structure with space group Pbnm, and the nickel-rich compounds ($x\geq 0.5$) have a rhombohedral structure with space group $R\bar{3}c$; the same as LaNiO_3 . The orthorhombic patterns have additional superstructural Bragg reflections of low intensity at positions far from the characteristic reflections of the ideal perovskite, and the rhombohedral patterns are characterized by the splitting of the main reflections. For all intermediate composition, the superstructural reflections, which might suggest long-range ordering of Fe^{3+} and Ni^{3+} , were not observed. However, the difference in the scattering lengths of Fe and Ni is modest; strong preferential occupancy is needed to produce Fe/Ni superstructure peaks. The Ni^{3+} and Fe^{3+} cations appear to be randomly distributed in the same crystallographic positions.

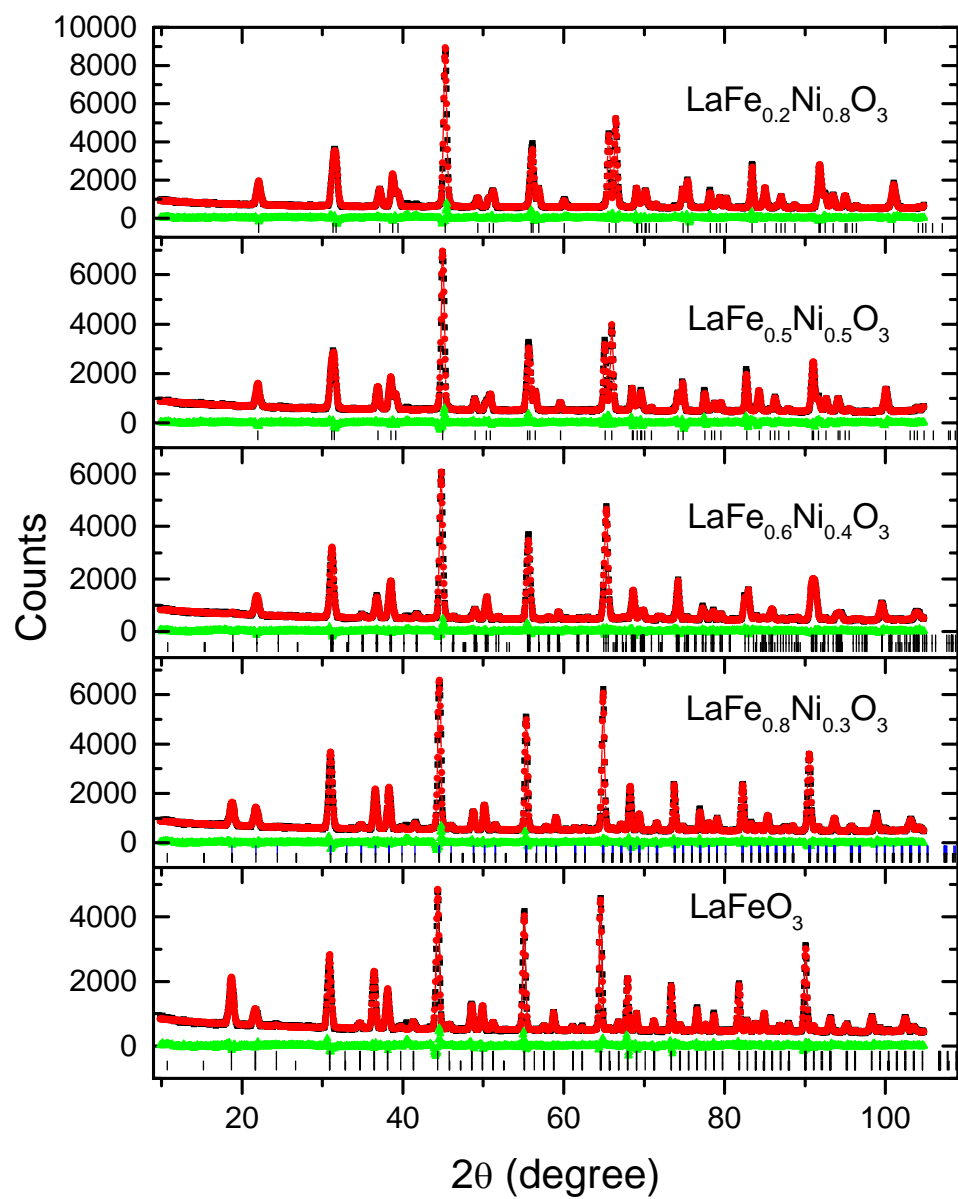


Figure 4.14: The neutron diffraction patterns of $\text{LaFe}_{1-x}\text{Ni}_x\text{O}_3$ at room temperature.

The two different symmetries observed in this series can be explained by the tolerance factor t ⁽¹⁸⁾, which is defined in formula (2.2). For the ideal cubic perovskite, the tolerance factor is around 1. If the t value is slightly less than 1, rhombohedral distortion is observed. For smaller t (<0.97), the distortion is orthorhombic. Table 4.9 shows the tolerance factor t calculated from the ionic radii. In these calculations, we have taken 1.36Å as the 12-coordinated effective ionic radius of La^{3+} , 0.56Å and 0.645Å as the 6-coordinated effective radii for Ni^{3+} (low spin) and Fe^{3+} (high spin) respectively and 1.40Å as the radius of O^{2-} .⁽⁴²⁾ The radii of the B sites were obtained by the atom-weighted average of the radii of Ni^{3+} and Fe^{3+} . From Table 4.9, the tolerance factor t is seen to decrease as the iron fraction increases. The rhombohedral symmetry was observed experimentally for the tolerance factor between 0.987 and 0.975. For $t \leq 0.970$, the orthorhombic distortion appeared.

Table 4.9: Tolerance factor t for $\text{LaFe}_{1-x}\text{Ni}_x\text{O}_3$.

Sample	$x=0.8$	$x=0.5$	$x=0.4$	$x=0.2$	$x=0$
t	0.987	0.975	0.970	0.964	0.954
Symmetry	R	R	O	O	O

The tolerance factor t decreases as the fraction of iron increases indicating that the distortion increases as the iron fraction increases. This result can be seen from the refined results in Table 4.10. For example, in the rhombohedral range, the x coordinate of oxygen changes from 0.5478(3) to 0.5541(3) as the iron fraction increases from 0.2 to 0.5. This parameter is 0.5 without distortion, and the larger deviation from this value corresponds

to an increase of the tilting of the octahedral (Ni, Fe)O₆ and therefore of the distortion of the perovskite.

Table 4.10: The results obtained from the Rietveld refinement of the neutron diffraction data of LaFe_{1-x}Ni_xO_{3+δ} at room temperature. The A and B sites are fully occupied and the ratio of Fe/Ni is fixed at the synthesis ratio.

Sample	LaFeO _{3+δ}	Fe _{0.8}	Fe _{0.6}	Fe _{0.5}	Fe _{0.2}
Space Group	Pbnm	Pbnm	Pbnm	R-3c	R-3c
a (Å)	5.55153(46)	5.53531(48)	5.52353(27)	5.51539(20)	5.47561(18)
b (Å)	5.55946(46)	5.52378(44)	5.48510(28)		
c (Å)	7.85318(78)	7.82335(81)	7.77920(45)	13.27986(60)	13.18234(53)
Vol (Å ³)	242.377(37)	239.206(38)	235.687(22)	349.845(24)	342.285(21)
Total O	3.016(22)	3.044(18)	3.054(16)	3.054(18)	3.036(12)
La x	-0.004(2)	-0.006(1)	-0.0049(9)		
y	-0.0296(6)	-0.0257(6)	-0.0192(6)		
Occ	0.5	0.5	0.5	0.167	0.167
B (Å ²)	0.71(6)	0.82(5)	0.80(4)	0.87(4)	0.69(4)
Fe Occ	0.5	0.4	0.3	0.083	0.033
Ni Occ	0	0.1	0.2	0.083	0.133
B (Å ²)	0.75(5)	0.67(4)	0.58(3)	0.73(4)	0.74(4)
μ _{RT} (μ _B)	3.75(3)	2.61(3)	0.76(6)	0	0
O1 x	0.082(2)	0.071(2)	0.0624(9)	0.5541(3)	0.5478(3)
y	0.512(1)	0.508(1)	0.506(1)		
Occ	0.5	0.5	0.5	0.509(3)	0.506(2)
B (Å ²)	1.0(2)	1.1(2)	0.81(9)	1.27(5)	1.09(5)
O2 x	0.780(1)	0.7790(9)	0.7743(6)		
y	0.218(1)	0.223(1)	0.2242(6)		
z	0.0362(7)	0.0368(8)	0.0347(5)		
Occ	1.008(11)	1.022(9)	1.027(8)		
B (Å ²)	0.8(1)	1.2(1)	1.24(9)		
R _p (%)	4.24	4.05	3.91	4.52	4.35
R _{wp} (%)	5.76	5.39	5.00	6.05	5.75
χ ²	2.37	2.29	1.75	2.78	2.95

Figure 4.15 shows the dependence of the cell parameters with composition for both phases, they are all normalized by $\sqrt{2}$, 2, or $2\sqrt{3}$ to put them on the same scale. Figure 4.16 shows the unit cell volume per formula unit with the Ni fraction in the LaFe_{1-x}Ni_xO₃ series. The lattice parameters and the unit cell volume decrease as the Ni fraction

increases in both phases. This effect can be easily understood considering the ionic radii of Ni^{3+} (low spin) and Fe^{3+} (high spin), which are 0.56\AA and 0.645\AA respectively. In the orthorhombic phase, they are linear; in the rhombohedral phase, we need more points to verify the linear relationship between them.

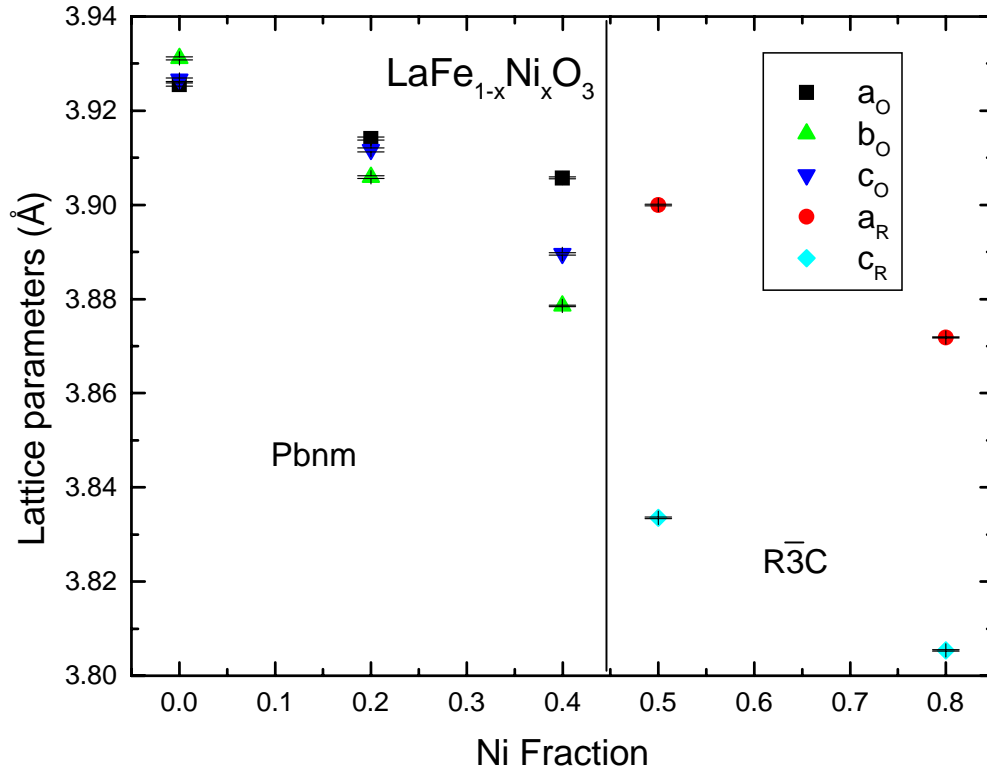


Figure 4.15: Dependence of lattice parameters with composition for $\text{LaFe}_{1-x}\text{Ni}_x\text{O}_3$. For the orthorhombic phase, $a_o = a/\sqrt{2}$, $b_o = b/\sqrt{2}$, and $c_o = c/2$; for the rhombohedral phase, $a_R = a/\sqrt{2}$, and $c_R = c/2\sqrt{3}$.

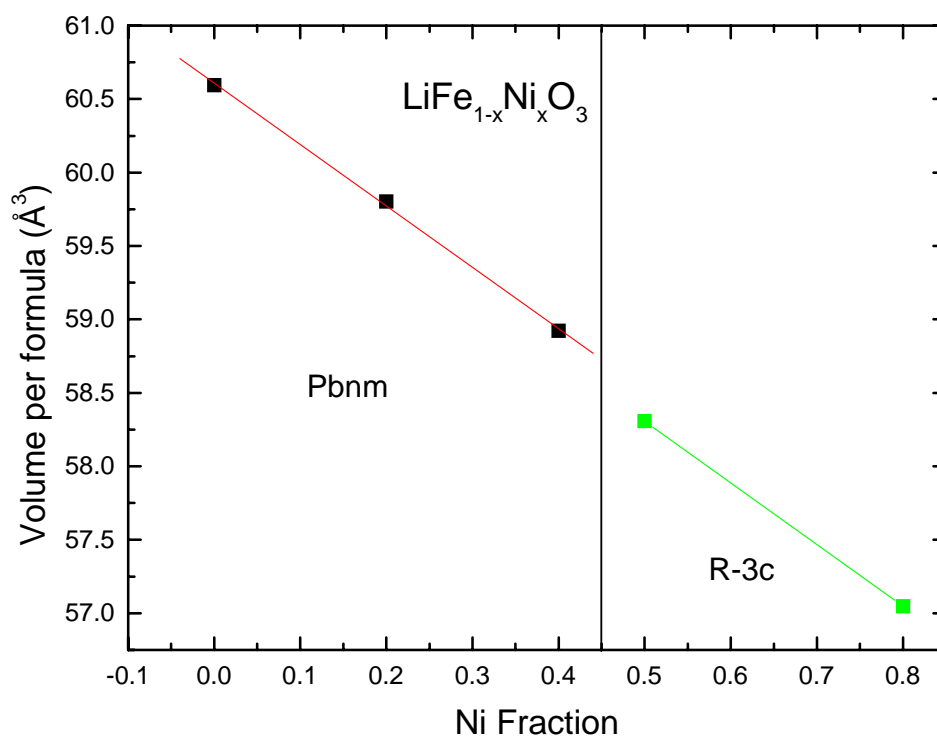


Figure 4.16: Dependence of the unit cell volume per formula unit with composition, for $\text{LaFe}_{1-x}\text{Ni}_x\text{O}_3$.

According to Table 4.10, the total oxygen per formula unit is very close to stoichiometric. The maximum oxygen excess is 1.8(5)% for the $\text{LaFe}_{0.6}\text{Ni}_{0.4}\text{O}_3$ and $\text{LaFe}_{0.5}\text{Ni}_{0.5}\text{O}_3$ compounds. The presence of oxygen excess indicates some vacancies in the A and B sites in this system.

There is a long range anti-ferromagnetic ordering at room temperature in the compounds of $\text{LaFe}_{1-x}\text{Ni}_x\text{O}_3$ ($x \leq 0.4$), and the average magnetic moment at the B sites decreases with the substitution of Fe by Ni since Ni^{3+} is in a low spin state. Figure 4.17 shows the dependence of the average magnetic moment at room temperature with the Ni fraction. The magnetic ordering disappears in the rhombohedral phase range.

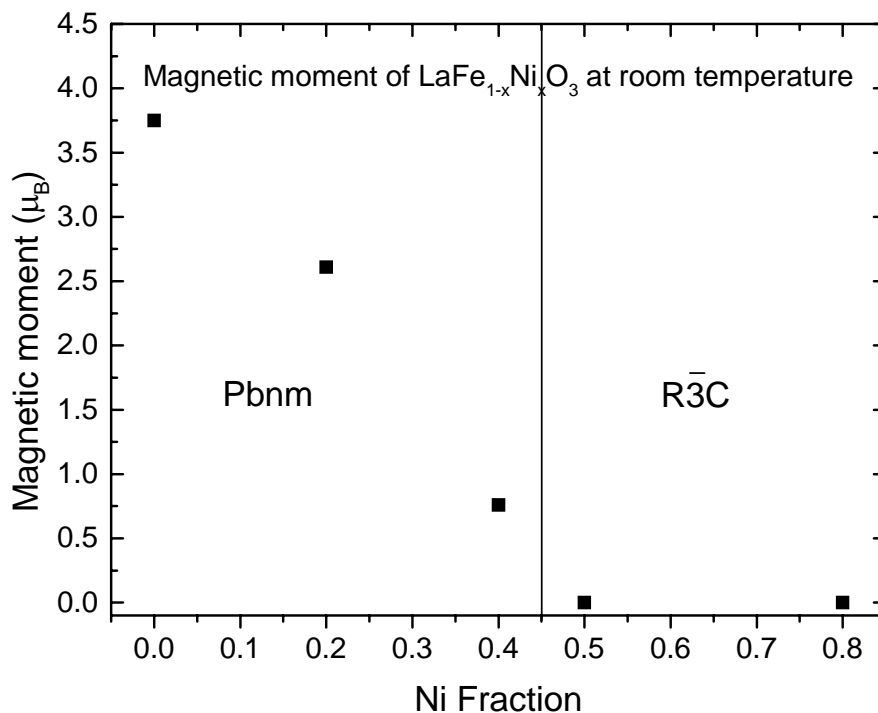


Figure 4.17: The average magnetic moment at B sites vs. Ni content for the $\text{LaFe}_{1-x}\text{Ni}_x\text{O}_3$ series.

$\text{LaFe}_{0.4}\text{Ni}_{0.6}\text{O}_3$ SINTERED IN AIR FROM 800°C to 1400°C

According to Chiba's paper,⁽³⁹⁾ $\text{LaFe}_{0.4}\text{Ni}_{0.6}\text{O}_3$ has maximum electronic conductivity at 800°C in the $\text{LaFe}_{1-x}\text{Ni}_x\text{O}_3$ series, and its thermal expansion coefficient is $11.4 \times 10^{-6} \text{ (K}^{-1}\text{)}$ between room temperature and 1000°C. This is closer to the TEC of YSZ of $10.0 \times 10^{-6} \text{ (K}^{-1}\text{)}$ than $\text{La}_{0.8}\text{Sr}_{0.2}\text{MnO}_3$ ($12.0 \times 10^{-6} \text{ (K}^{-1}\text{)}$). It is important to find the stability of this compound at high temperature in air. In this study, six $\text{LaFe}_{0.4}\text{Ni}_{0.6}\text{O}_3$ samples, sintered in air for 1 hour from 800°C to 1400°C, were studied by powder neutron diffraction.

All the samples have the rhombohedral structure with space group $R\bar{3}c$, this result is consistent with the above study. The samples sintered at 800°C, 900°C, 1000°C and

1100°C are all single phase, this means that $\text{LaFe}_{0.4}\text{Ni}_{0.6}\text{O}_3$ is stable in air up to 1100°C. This is in contrast to LaNiO_3 , which is unstable above 850°C and decomposes to La_2NiO_4 (which has a K_2NiF_4 structure) and NiO , whose conductivities are insufficiently high⁽⁴³⁾. The samples sintered at 1300°C and 1400°C, contain the main perovskite phase, and no more than 2.5wt% NiO . The presence of NiO indicates that some perovskite decomposed to La_2NiO_4 and NiO , and the remaining perovskite phase has a higher ratio of Fe/Ni than 0.4/0.6. The substitution of Ni by Fe considerably increases the stability of the perovskite phase at high temperature. This increase in stability might be assigned to the higher stability of Fe^{3+} compare to Ni^{3+} , which can be reduced easily. The refined results are listed in Table 4.11, and two typical patterns are shown in Figure 4.18. There is no magnetic ordering at room temperature for any sample and there is no magnetic ordering at 12K for the sample sintered at 1400°C.

According to Table 4.11, the refined Fe/Ni ratio is 0.58/0.42 for the 1300°C sintered sample and 0.74/0.36 for the 1400°C sample. The uncertainty in this result is large, since the coherent scattering length of Fe and Ni are 0.945×10^{-12} and 1.03×10^{-12} cm respectively, and their scattering lengths are sufficiently close that neutron cannot indentify the Fe and Ni clearly. Incidentally, the structure should be orthorhombic and long range magnetic ordering should appear if the iron fraction is as high as reported in the refinement.

Figure 4.19 shows the dependence of the unit cell volume and the oxygen excess/vacancy with the sintering temperature. When the sintering temperature is less

Table 4.11: The results obtained from the Rietveld refinement of the neutron diffraction data of $\text{LaFe}_{0.4}\text{Ni}_{0.6}\text{O}_{3-\delta}$ at room temperature. The A site and B sites are fully occupied and the ratio of Fe/Ni is fixed as 0.4/0.6 if there is no second phase.

Sample	800°C	900°C	1000°C	1100°C	1300°C	1400°C
Space group	R-3c	R-3c	R-3c	R-3c	R-3c	R-3c
a (Å)	5.50611(18)	5.50552(18)	5.50465(17)	5.50559(17)	5.51858(23)	5.52177(22)
c (Å)	13.26188(51)	13.26071(52)	13.25792(49)	13.25863(50)	13.26199(65)	13.28446(65)
Vol (Å ³)	348.197(21)	348.092(21)	347.909(20)	348.046(20)	349.779(27)	350.777(26)
Total O	3.030(12)	3.024(12)	3.030(12)	3.018(12)	2.916(18)	2.874(18)
La Occ.	0.167	0.167	0.167	0.167	0.167	0.167
B (Å ²)	1.00(4)	1.02(4)	0.96(3)	0.99(3)	1.31(6)	1.36(6)
Fe Occ.	0.067	0.067	0.067	0.067	0.097(13)	0.123(13)
Ni Occ.	0.1	0.1	0.1	0.1	0.070(13)	0.044(13)
B (Å ²)	0.71(3)	0.69(3)	0.67(3)	0.66(3)	0.88(4)	0.84(4)
O _x	0.5533(2)	0.5533(2)	0.5534(2)	0.5533(2)	0.5561(3)	0.5569(3)
Occ.	0.505(2)	0.504(2)	0.504(2)	0.503	0.486(3)	0.479(3)
B (Å ²)	1.28(4)	1.30(4)	1.28(4)	1.27(4)	1.75(6)	1.87(6)
2 nd phase						
NiO wt%					1.15%	2.49%
a (Å)					4.17779(67)	4.17622(33)
R _p (%)	5.43	5.30	5.39	5.51	6.28	5.86
R _{wp} (%)	6.97	6.70	6.97	7.00	7.96	7.42
χ ²	3.19	3.00	3.44	3.78	5.62	3.99

than or equal to 1100°C, the oxygen excess and unit cell volume do not change much; when the sintering temperature is above 1100°C, oxygen vacancies appear and the unit cell volume increases. The obvious relation between the unit cell volume and oxygen vacancies vs. sintering temperature shows that the increase of unit cell volume is due to the increase of the oxygen vacancies.

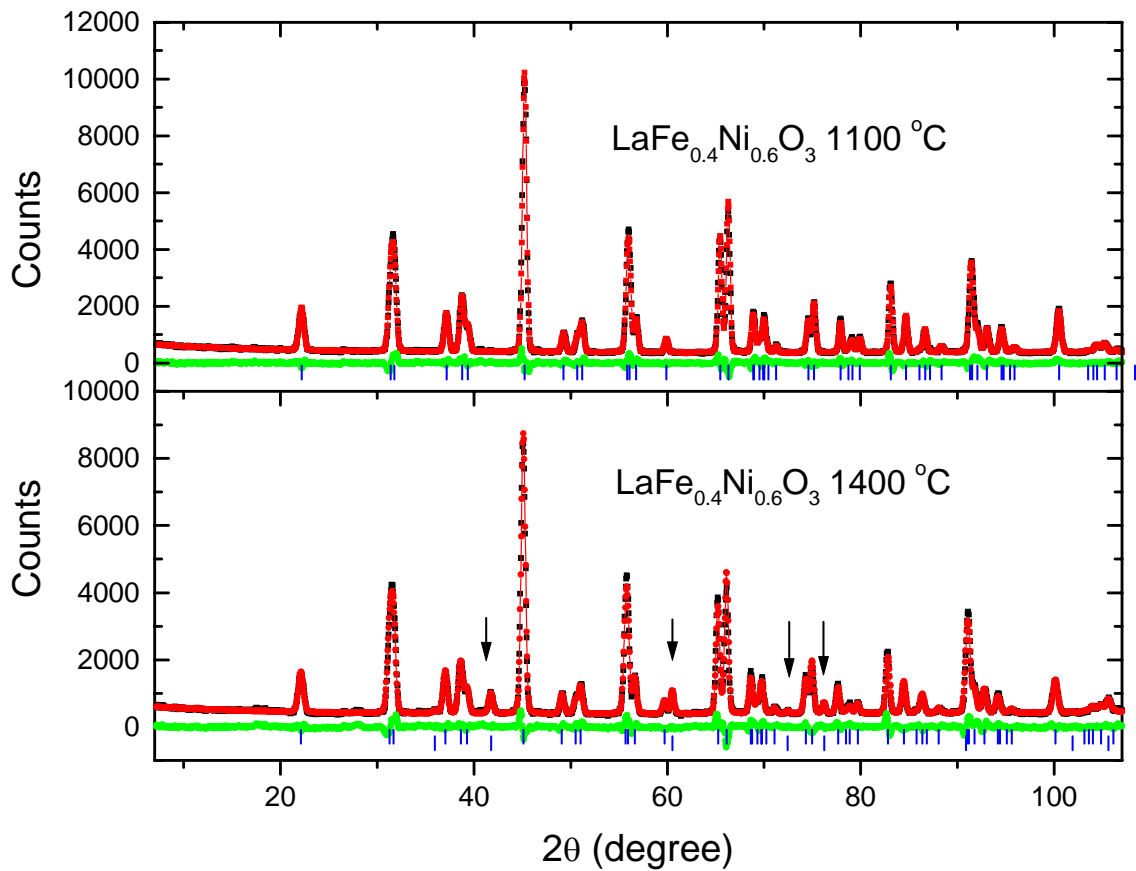


Figure 4.18: The neutron diffraction patterns of $\text{LaFe}_{0.4}\text{Ni}_{0.6}\text{O}_3$ samples sintered at 1100°C and 1400°C. The peaks indicated by the arrows are the NiO peaks.

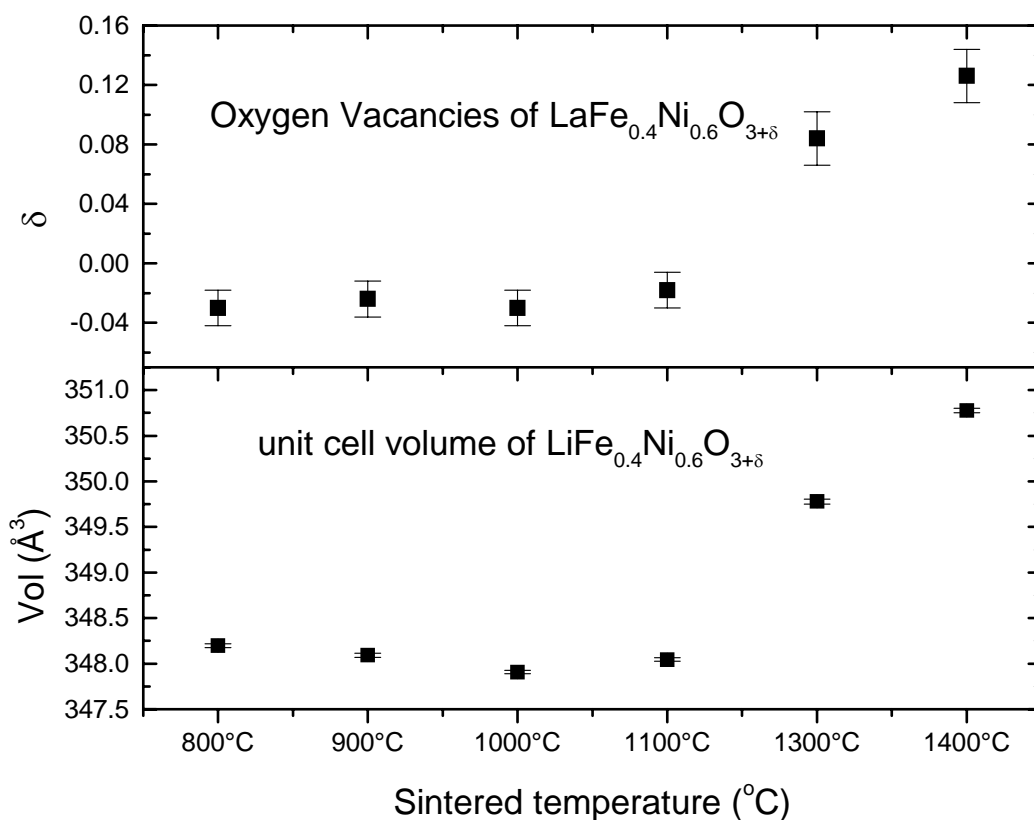


Figure 4.19: The oxygen stoichiometry deviation and unit cell volume in $\text{LaFe}_{0.4}\text{Ni}_{0.6}\text{O}_{3+\delta}$ vs. sintering temperature.

b) $\text{LaFe}_{1-x}\text{Mn}_x\text{O}_{3+\delta}$

The neutron diffraction studies on samples of $\text{LaFe}_{1-x}\text{Mn}_x\text{O}_{3+\delta}$ were carried out at room temperature and low temperature (16K). The Rietveld refinements were performed with the constraint of full A site and B site occupancies, but the Fe and Mn fractions were allowed to be refined since the coherent scattering lengths of Fe and Mn are very different and the refinement are very sensitive to their ratio. The oxygen sites occupancy, therefore, was allowed to vary. The refined results are listed in Table 4.12, and four typical neutron diffraction patterns at room temperature are shown in Figure 4.20. For the Fe-rich samples ($x \leq 0.5$), the crystal structure is orthorhombic with space group Pbnm.

Table 4.12: Refinement results for $\text{LaFe}_{1-x}\text{Mn}_x\text{O}_3$ at room temperature.

sample	Fe _{0.95}	Fe _{0.9}	Fe _{0.8}	Fe _{0.6}	Fe _{0.5}	Fe _{0.4}	Fe _{0.2}	Fe _{0.1}	Fe _{0.05}
Space Group	Pbnm	Pbnm	Pbnm	Pbnm	Pbnm	R-3c	R-3c	R-3c	R-3c
a (Å)	5.54528(48)	5.55307(50)	5.55647(80)	5.53574(127)	5.53818(64)	5.52284(49)	5.52139(31)	5.51923(31)	5.51885(32)
b (Å)	5.55785(38)	5.55367(53)	5.53843(73)	5.50701(123)	5.50072(64)				
c (Å)	7.86089(73)	7.84386(90)	7.8325(12)	7.8231(13)	7.79733(95)	13.3707(14)	13.33712(86)	13.33050(86)	13.32585(86)
Vol (Å ³)	242.271(35)	241.904(42)	241.038(60)	238.489(96)	237.538(49)	353.189(58)	352.119(36)	351.669(36)	351.498(36)
Total O	3.026(18)	3.052(20)	3.100(34)	3.188(66)	3.194(36)	3.378(78)	3.240(54)	3.330(54)	3.294(54)
La x	-0.003(1)	-0.005(1)	-0.009(2)	-0.002(4)	-0.008(1)				
y	-0.0275(5)	-0.0289(5)	-0.0272(9)	-0.021(2)	-0.0195(9)				
Occ	0.5	0.5	0.5	0.5	0.5	0.167	0.167	0.167	0.167
B (Å ²)	1.09(5)	0.85(6)	0.93(9)	0.9(1)	0.8(1)	1.1(1)	1.2(1)	1.3(1)	1.4(1)
Fe Occ	0.469(2)	0.449(2)	0.393(4)	0.310(6)	0.258(5)	0.071(1)	0.032(1)	0.014(1)	0.006(1)
Mn Occ	0.031(2)	0.051(2)	0.107(4)	0.190(6)	0.242(5)	0.095(1)	0.135(1)	0.153(1)	0.161(1)
B (Å ²)	0.60(4)	0.77(5)	0.5(1)	0.3(2)	1.1(3)	1.0(5)	0.3(5)	0.8(3)	0.7(3)
$\mu_{\text{RT}}(\mu_{\text{B}})$	3.49(3)	3.33(3)	2.82(4)	1.67(7)	0	0	0	0	0
$\mu_{16\text{K}}(\mu_{\text{B}})$	3.80(3)	3.75(3)	3.33(3)	2.34(5)	1.80(3)	0.99(6)	0	0	0
$\mu_{\text{RT}}/\mu_{16\text{K}}$	0.918	0.888	0.847	0.714	0	0			
O1 x	0.064(1)	0.080(2)	0.078(2)	0.054(3)	0.068(1)	0.4505(3)	0.4503(3)	0.4517(3)	0.4514(3)
y	0.5134(9)	0.510(1)	0.506(1)	0.499(3)	0.503(1)				
Occ	0.5	0.5	0.5	0.5	0.5	0.563(13)	0.540(9)	0.555(9)	0.549(9)
B (Å ²)	1.18(5)	1.24(6)	1.50(9)	1.4(1)	1.58(9)	1.73(9)	1.67(6)	1.73(6)	1.78(6)
O2 x	0.7795(8)	0.779(1)	0.785(2)	0.775(2)	0.776(1)				
y	0.2151(9)	0.220(1)	0.223(2)	0.230(2)	0.230(1)				
z	0.0419(6)	0.0343(6)	0.027(1)	0.036(1)	0.0271(8)				
Occ	1.013(9)	1.026(10)	1.050(17)	1.094(33)	1.097(18)				
2 nd phase Mn wt%				3.4(4)%	2.6(3)%	3.1(3)%	0.7(1)%	1.4(3)%	2.7(3)%
a (Å)				3.0277(8)	3.0291(7)	3.0243(7)	3.027(1)	3.026(1)	3.0299(8)

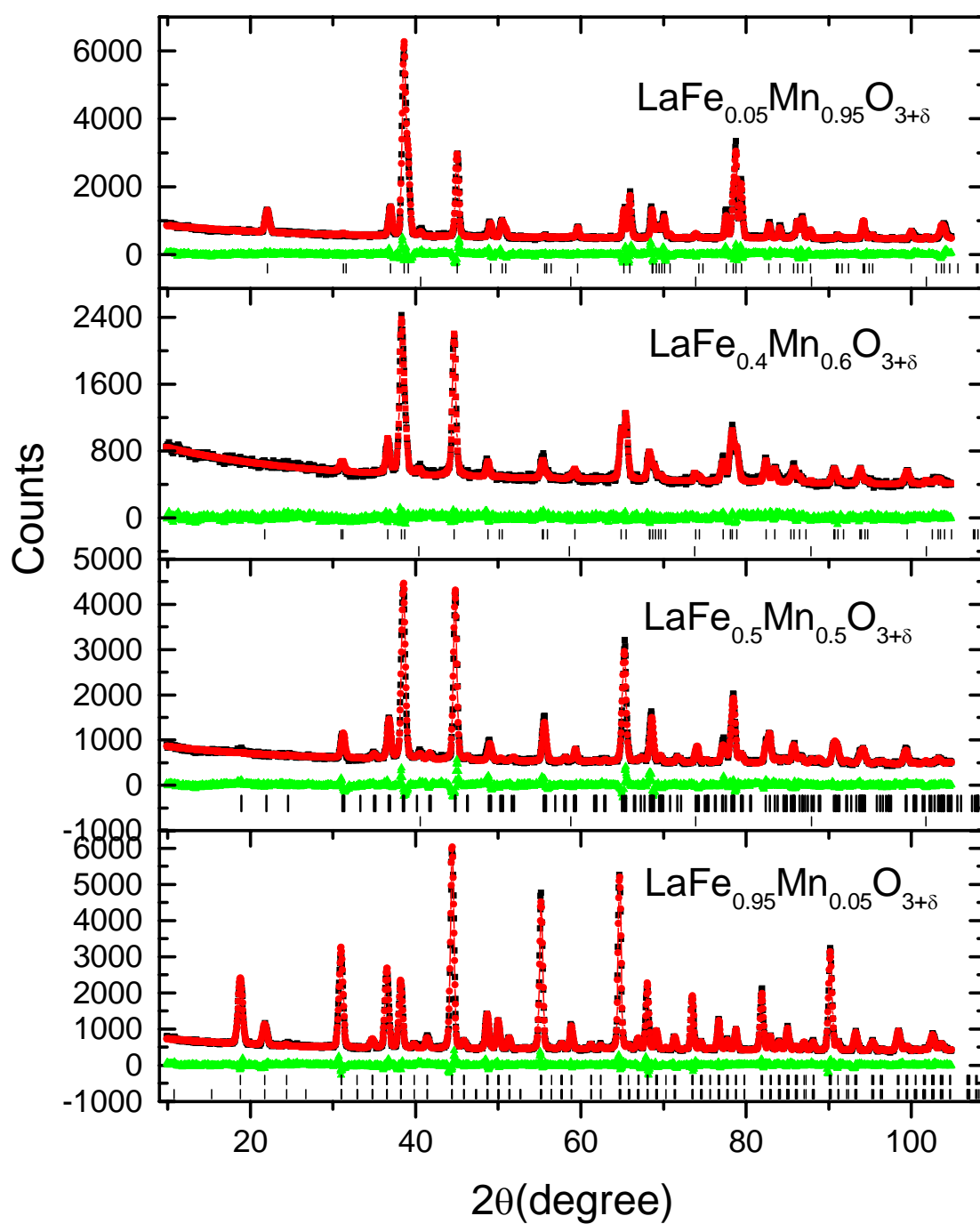


Figure 4.20: Four typical neutron diffraction patterns from the $\text{LaFe}_{1-x}\text{Mn}_x\text{O}_3$ series, at room temperature.

There are many additional superstructural reflections with low intensity at Bragg positions far from the characteristic reflections of the ideal perovskite, and these reflections decrease as the Mn fraction increases. For the Mn-rich samples, the structure is rhombohedral with space group $R\bar{3}c$. There is no more than 3.4wt% Mn metal as a second phase for the samples with $x \geq 0.4$. Mn has a cubic structure with space group $Im\bar{3}m$, and lattice parameter a equal to 3.0277Å.

The two different crystal structures observed in these samples can not be explained by the substitution of Fe^{3+} by Mn^{3+} , since the ionic radius of Fe^{3+} (high spin) is 0.645Å for coordination number 6, nearly identical with that of Mn^{3+} (high spin). However, excess oxygen in these samples can explain the symmetry change. Figure 4.21 shows the total oxygen as a function of the Mn fraction in these samples. In the orthorhombic range, the oxygen excess increases linearly as the Mn fraction increases, but in the rhombohedral range, the oxygen excess is large and does not increase as the Mn fraction increases. The average oxygen excess δ is about 0.31, which is close to the maximum value 0.29 in the over-stoichiometric $LaMnO_{3+\delta}$ perovskites reported by A. Barnabe⁽⁴⁴⁾. It seems that there is a limit to the oxygen excess. For the perovskite materials, interstitial oxygen is not allowed since the perovskite structure is close-packed; therefore, the excess oxygen refined for the nominal site indicates the existence of cation vacancies on both A and B sites, and the maximum cation vacancy concentration is about 9.4%. Refinement of the relative oxygen occupancy simplifies the analysis by keeping the A and B sites occupancies fixed at one. When cation vacancies are present, the charge neutrality condition necessitates an increasing oxidation state of some Mn ions from Mn^{3+} to Mn^{4+} . Since the ionic radius of Mn^{4+} (0.53Å) is smaller than that of Fe^{3+} , the tolerance factor

will increase as the Mn^{4+} fraction increases and Table 4.13 shows the tolerance factor t calculated from the refined oxygen excess. Not surprisingly the symmetry change occurs when the tolerance factor t is above 0.976.

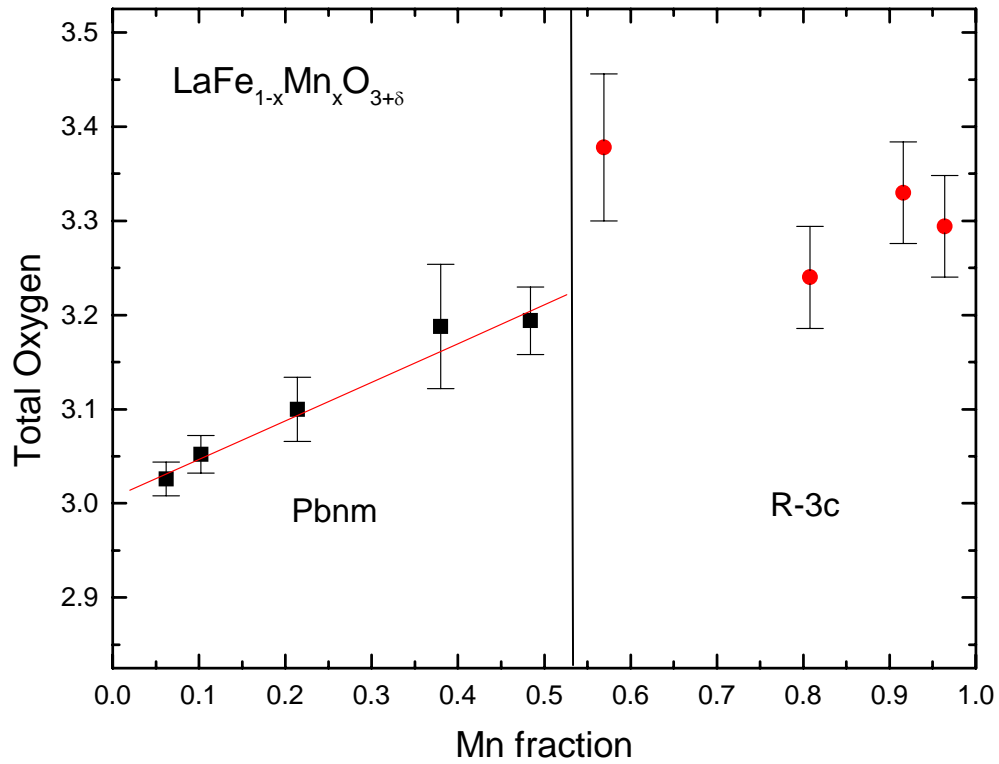


Figure 4.21: Total oxygen as a function of Mn content in $\text{LaFe}_{1-x}\text{Mn}_x\text{O}_3$.

Table 4.13: The tolerance factor t for $\text{LaFe}_{1-x}\text{Mn}_x\text{O}_{3+\delta}$

Sample	$\text{Fe}_{0.95}$	$\text{Fe}_{0.9}$	$\text{Fe}_{0.8}$	$\text{Fe}_{0.6}$	$\text{Fe}_{0.5}$	$\text{Fe}_{0.4}$	$\text{Fe}_{0.2}$	$\text{Fe}_{0.1}$	$\text{Fe}_{0.05}$
t	0.957	0.960	0.965	0.975	0.976	0.988	0.981	0.991	0.987
Symmetry	O	O	O	O	O	R	R	R	R

Figure 4.22 shows the unit cell volume (normalized by the number of formulae in the unit cell) as a function of the Mn fraction. The unit cell volume decreases linearly as the Mn fraction increases, in both the orthorhombic and rhombohedral phases, but the unit cell volume decreases much faster in the orthorhombic phase than it does in the rhombohedral phase. The two different slopes of the unit cell volume in the two ranges indicates that the unit cell volume decrease has more than one origin. In the orthorhombic phase range, the oxygen excess dominates the unit cell volume change, it increases the oxidation state of most Mn ions from Mn^{3+} to Mn^{4+} , and the ionic radius of Mn^{4+} (0.53\AA)⁽⁴²⁾ is smaller than that of Fe^{3+} (0.645\AA)⁽⁴²⁾. In the rhombohedral phase range, the oxygen excess is saturated, and the volume change is dominated by the substitution of Fe by Mn. The unit cell volume drop at the phase change is due to a discontinuity in the oxygen excess.

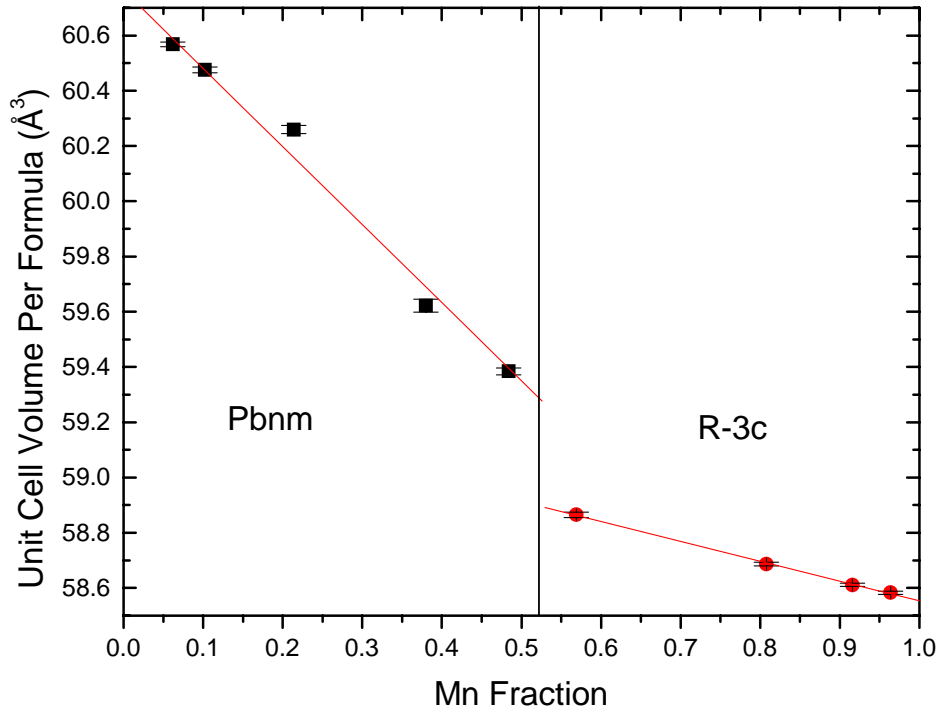


Figure 4.22: The unit volume per formula of $\text{LaFe}_{1-x}\text{Mn}_x\text{O}_{3+\delta}$ vs. Mn content.

The magnetic properties of $\text{LaFe}_{1-x}\text{Mn}_x\text{O}_{3+\delta}$ mirror the behaviors of the end members of the series. One end compound, LaFeO_3 , shows antiferromagnetic ordering with $T_N=750\text{K}$. Its oxygen concentration is stoichiometric, therefore, the $\text{Fe}^{3+}\text{-O}^{2-}\text{-Fe}^{3+}$ superexchange dominates its magnetic exchange. The other end compound, $\text{LaMnO}_{3+\delta}$, can be antiferromagnetic, ferromagnetic and magnetically disordered depending on the oxygen excess δ . The Fe-rich samples ($x\leq 0.4$) are antiferromagnetic at room temperature and the average magnetic moment at the B site decreases with increasing Mn content. The Mn-rich samples ($x>0.6$), which have a large oxygen excess, show no magnetic ordering above 16K. It is of interest to compare LFMO with $\text{La}_{0.6}\text{Sr}_{0.4}\text{FeO}_{3-\delta}$, whose saturated magnetic moment increases linearly with the oxygen vacancies, i.e., the fraction of Fe^{3+} . Figure 4.23 shows the magnetic moments at the B site at room temperature and 16K both as a function of Mn fraction. The solid line showing the magnetic moment (and Fe^{3+} concentration) observed in L6SF, is included for comparison. When $x\leq 0.4$, the refined magnetic moment exceeds the linear approximation. In this range, almost all Mn ions are Mn^{4+} due to the oxygen excess, therefore, $\text{Fe}^{3+}\text{-O}^{2-}\text{-Mn}^{4+}$ superexchange may exist and contribute to the overall antiferromagnetic moment. When $x\geq 0.5$, the refined magnetic moment is smaller than the linear approximation. In this range, Mn^{3+} ions appear and increase with the Mn fraction, The $\text{Fe}^{3+}\text{-O}^{2-}\text{-Mn}^{3+}$ superexchange is probably ferromagnetic and competes with the antiferromagnetic $\text{Fe}^{3+}\text{-O}^{2-}\text{-Mn}^{4+}$ superexchange, depressing the ordering temperature.

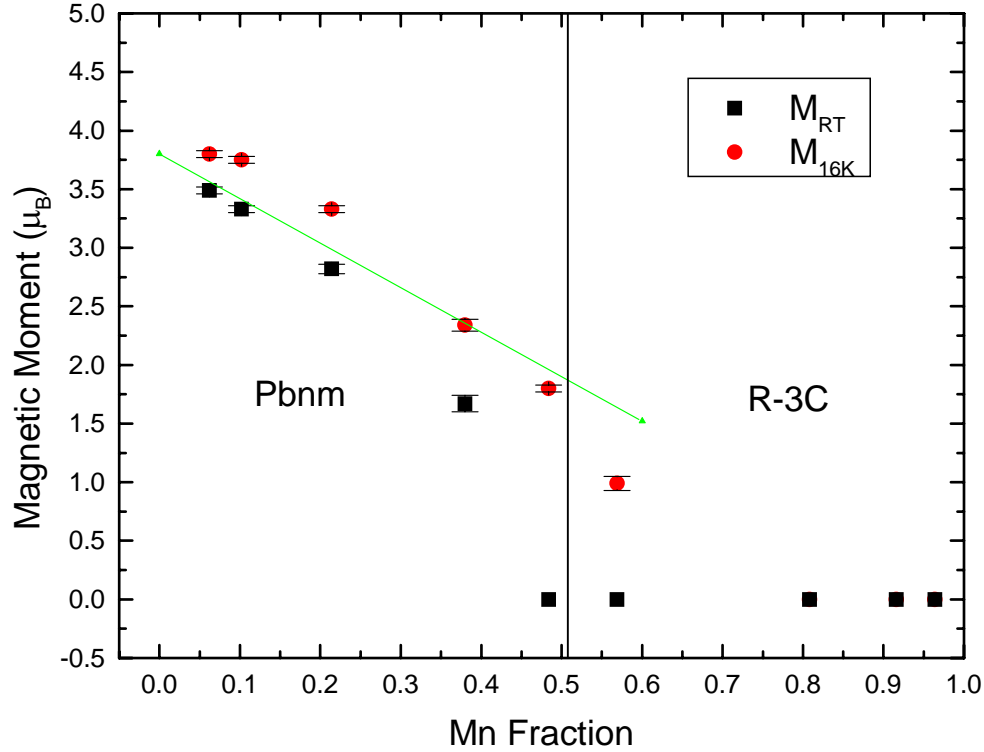


Figure 4.23: The magnetic moments at B sites at room temperature and 16K as a function of Mn fraction in $\text{LaFe}_{1-x}\text{Mn}_x\text{O}_3$.

c) $\text{LaFe}_{1-x}\text{Cu}_x\text{O}_3$ ($x \leq 0.5$)

In order to understand the properties of $\text{LaFe}_{1-x}\text{Cu}_x\text{O}_3$, it is necessary to have a general knowledge about its end compounds. The end compound, LaFeO_3 , is an orthorhombic distorted perovskite with antiferromagnetic ordering near $750\text{K}^{(45)}$. The other end compound, LaCuO_3 , is isomorphous with LaNiO_3 , with a rhombohedrally distorted perovskite structure. The rhombohedral LaCuO_3 can only be synthesized under high oxygen pressure⁽⁴⁶⁾. This stoichiometric perovskite loses oxygen upon heating at ambient pressure, yielding various $\text{LaCuO}_{3-\delta}$ oxygen deficient phases as intermediates, such as the tetragonal, monoclinic, and orthorhombic phases. LaCuO_3 decomposes to La_2CuO_4 and CuO or Cu_2O around $1070\text{K}^{(47)}$.

The $\text{LaFe}_{1-x}\text{Cu}_x\text{O}_3$ samples synthesized by using the glycine-nitrate process, are single phase when $x \leq 0.3$; the maximum Cu solubility in this system is $\sim 30\%$ atm, and the samples with $x \geq 0.4$ have La_2CuO_4 as their second phase. The crystal structure of all samples is orthorhombic with space group Pbnm. Figure 4.24 shows three typical neutron diffraction patterns at room temperature. The characteristic reflections of the orthorhombic phase; the additional superstructural reflections with low intensity far from the characteristic reflections of the ideal perovskite, begin to disappear at high angle as the Cu content increases. This can be explained by the increase of the tolerance factor t , due to the substitution of Fe^{3+} by Cu^{3+} . The calculated tolerance factor t is listed in Table 4.14, and the maximum tolerance factor is 0.974, which is close to the critical value of 0.975. The refined parameters are listed in Table 4.15; the oxygen occupancy refined from neutron diffraction data at room temperature is found to be 3.0 and is independent of Cu content. The unit cell volume is shown in Figure 4.25 as a function of the Cu content. The unit cell volume decreases linearly with the Cu content, since the ionic radius of the substitutional Cu^{3+} ions ($r=0.54\text{\AA}$)⁽⁴²⁾ is smaller than that of Fe^{3+} ions ($r=0.645\text{\AA}$)⁽⁴²⁾.

Table 4.14: The tolerance factor t of $\text{LaFe}_{1-x}\text{Cu}_x\text{O}_3$ ($x \leq 0.5$).

Sample	$\text{Cu}_{0.01}$	$\text{Cu}_{0.05}$	$\text{Cu}_{0.1}$	$\text{Cu}_{0.15}$	$\text{Cu}_{0.2}$	$\text{Cu}_{0.3}$	$\text{Cu}_{0.4}$	$\text{Cu}_{0.5}$
t	0.955	0.957	0.959	0.962	0.964	0.969	0.971	0.974
Symmetry	O	O	O	O	O	O	O	O

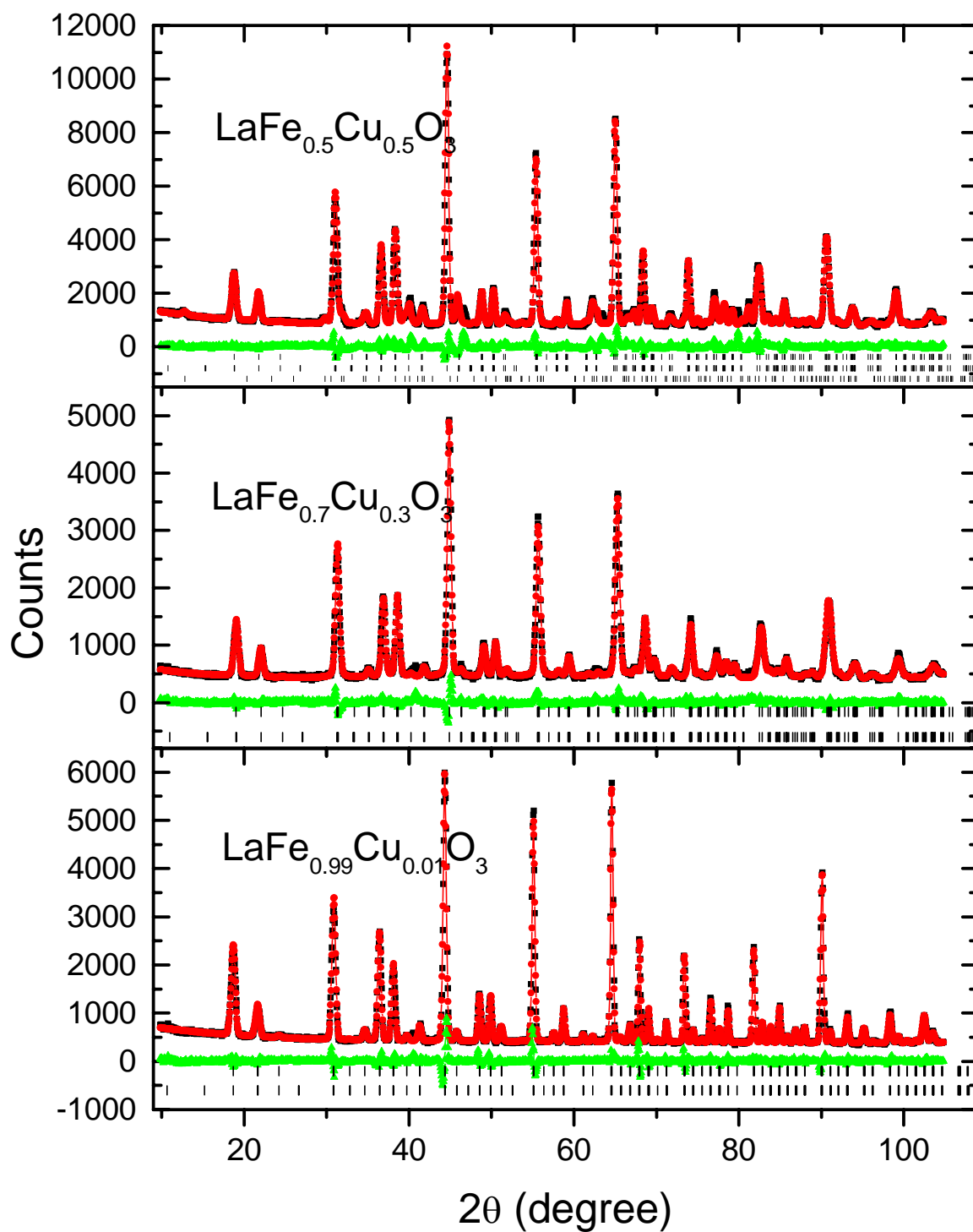


Figure 4.24: Three typical neutron diffraction patterns for the $\text{LaFe}_{1-x}\text{Cu}_x\text{O}_3$ ($x=0.01, 0.3, 0.5$) series.

Table 4.15: Refinement results for $\text{LaFe}_{1-x}\text{Cu}_x\text{O}_3$. All samples are orthorhombic structure with space group Pbnm.

Sample	$\text{Cu}_{0.01}$	$\text{Cu}_{0.05}$	$\text{Cu}_{0.1}$	$\text{Cu}_{0.15}$	$\text{Cu}_{0.2}$	$\text{Cu}_{0.3}$	$\text{Cu}_{0.4}$	$\text{Cu}_{0.5}$
a (Å)	5.55167(37)	5.55079(38)	5.54926(41)	5.54541(47)	5.54589(49)	5.53856(79)	5.53994(58)	5.53618(58)
b (Å)	5.55977(39)	5.55121(39)	5.54379(38)	5.53702(43)	5.52907(46)	5.50971(81)	5.51182(56)	5.50825(58)
c (Å)	7.84882(62)	7.84290(65)	7.83778(70)	7.83327(81)	7.83221(84)	7.81046(135)	7.81368(96)	7.81247(97)
Vol (Å ³)	242.262(30)	241.668(31)	241.121(33)	240.521(37)	240.164(39)	238.343(64)	238.592(46)	238.238(46)
Total O	2.992(20)	2.998(20)	3.038(18)	3.020(18)	3.002(20)	2.990(18)	2.992(20)	3.030(26)
La x	-0.007(1)	-0.006(1)	-0.007(1)	-0.007(1)	-0.006(1)	-0.001(2)	-0.005(1)	-0.003(2)
y	-0.0306(5)	-0.0299(5)	-0.0286(5)	-0.0268(5)	-0.0262(6)	-0.0236(7)	-0.0226(6)	-0.0238(8)
Occ	0.5	0.5	0.5	0.5	0.5	0.5	0.5	0.5
B (Å ²)	0.64(5)	0.71(5)	0.66(5)	0.73(5)	0.76(5)	0.72(6)	0.89(6)	1.02(8)
Fe Occ	0.495	0.475	0.45	0.425	0.4	0.35	0.331(19)	0.303(20)
Cu Occ	0.005	0.025	0.05	0.075	0.1	0.15	0.169(19)	0.197(20)
B (Å ²)	0.76(4)	0.78(4)	0.70(4)	0.65(4)	0.66(4)	0.60(5)	0.66(5)	1.1(1)
$\mu_{\text{RT}} (\mu_{\text{B}})$	3.73(3)	3.62(3)	3.47(3)	3.32(3)	3.16(3)	2.91(3)	2.80(3)	2.60(4)
$\mu_{16\text{K}} (\mu_{\text{B}})$	3.97(3)	3.97(3)	3.72(3)	3.51(3)	3.33(2)	3.16(3)		
$\mu_{\text{RT}}/\mu_{16\text{K}}$	0.940	0.912	0.933	0.946	0.949	0.921		
O1 x	0.082(2)	0.081(2)	0.080(2)	0.079(2)	0.077(2)	0.078(2)	0.072(1)	0.075(2)
y			0.510(1)	0.509(1)	0.509(1)	0.506(2)	0.508(1)	0.504(2)
Occ	0.5	0.5	0.5	0.5	0.5	0.5	0.5	0.5
B (Å ²)	0.7(1)	0.8(1)	0.8(1)	0.8(1)	1.0(2)	1.0(1)	1.2(2)	1.542)
O2 x	0.782(1)	0.782(1)	0.7812(9)	0.7809(9)	0.7798(8)	0.7786(9)	0.7748(8)	0.776(1)
y	0.218(1)	0.220(1)	0.221(1)	0.222(1)	0.2244(9)	0.226(1)	0.2246(8)	0.227(1)
z	0.0344(6)	0.0349(6)	0.0347(6)	0.0351(6)	0.0352(6)	0.0331(6)	0.0350(6)	0.0352(7)
Occ	0.996(10)	0.999(10)	1.019(9)	1.010(9)	1.001(10)	0.995(9)	0.996(10)	1.015(13)
B (Å ²)	0.9(1)	1.0(1)	1.1(1)	1.0(1)	0.9(1)	0.5(1)	0.9(1)	1.4(1)
La_2CuO_4								
Space group							Bmab	Bmab
a (Å)							5.35783(140)	5.35402(131)
b (Å)							5.39466(152)	5.40197(146)
c (Å)							13.15013(298)	13.14097(286)
Wt%							10.95(27)%	14.45(36)%
R_p (%)	5.06	5.38	5.49	5.13	5.61	4.60	4.62	5.15
R_{wp} (%)	7.06	7.42	7.57	7.08	7.86	5.92	5.91	7.14
χ^2	3.35	3.51	4.31	4.05	5.34	2.31	2.54	6.78

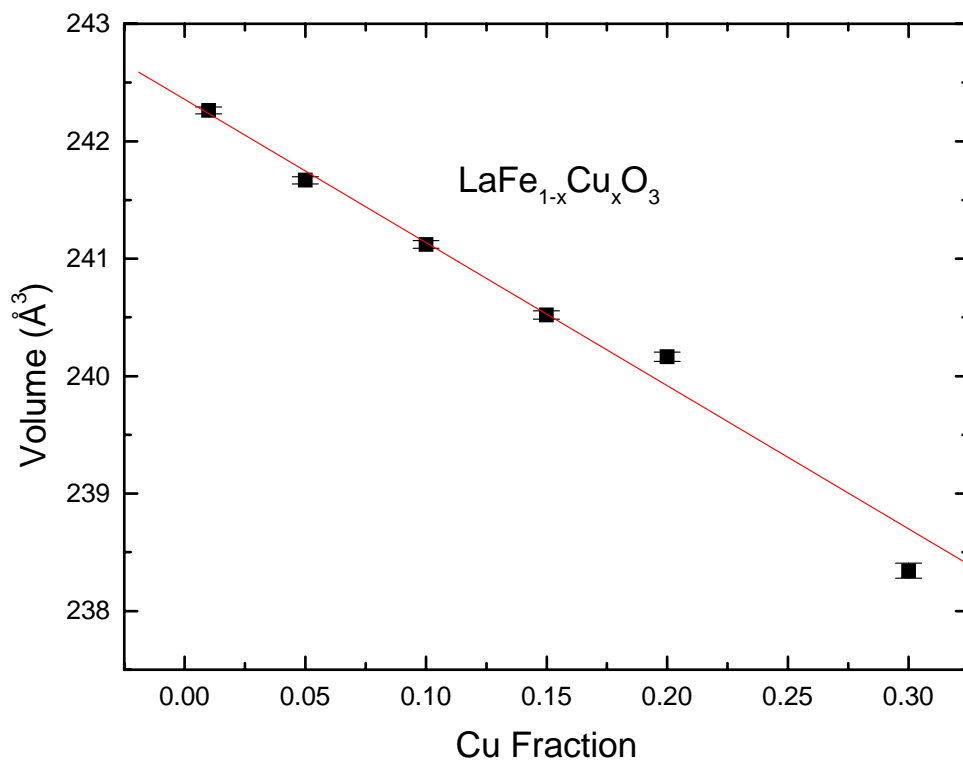


Figure 4.25: The unit cell volume of $\text{LaFe}_{1-x}\text{Cu}_x\text{O}_3$ ($x \leq 0.3$) vs. Cu content.

There is long range antiferromagnetic ordering at room temperature for all the samples. The average magnetic moment at the B site at room temperature and low temperature (16K) as a function of Cu content is shown in Figure 4.26, and the magnetic moments at room temperature and 16K both decrease as the Cu content increases. There is a linear relationship between the magnetic moment at room temperature and the Cu content, and the fitted relationship is:

$$\mu(x) = 3.76 - 2.9x \quad (4.4)$$

where μ is the average magnetic moment at the B sites (in Bohr magnetons), and x is the Cu atom content in the perovskite.

$\mu(0) = 3.76\mu_B$ gives the magnetic moment of Fe^{3+} at room temperature. This value is very close to $3.75\mu_B$, which is the refined magnetic moment of Fe^{3+} in LaFeO_3 at room temperature. $\mu(1) = 0.86\mu_B$ is the extrapolated magnetic moment of Cu^{3+} at room temperature.

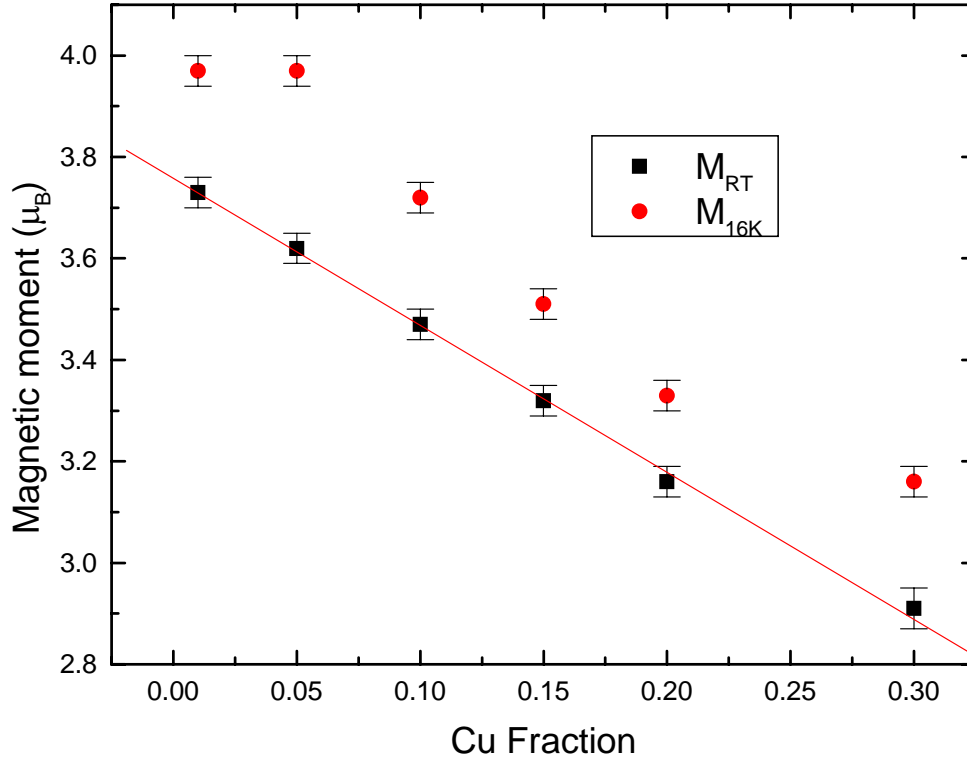


Figure 4.26: The magnetic moment of $\text{LaFe}_{1-x}\text{Cu}_x\text{O}_3$ at room temperature and 16K vs. Cu content.

The ratio of μ_{RT} to μ_{16K} is listed in Table 4.15. Unlike the $\text{LaFe}_{1-x}\text{Mn}_x\text{O}_3$ series, this ratio is above 90% for all Cu content and does not decrease as the Cu content increases. Apparently, the Neel temperature of all $\text{LaFe}_{1-x}\text{Cu}_x\text{O}_3$ ($x \leq 0.3$) samples does not decrease significantly with the substitution of Fe^{3+} by Cu^{3+} .

In-situ neutron diffraction studies on $\text{LaFe}_{0.9}\text{Cu}_{0.1}\text{O}_3$ were carried out at high temperature. Figure 4.27 shows the neutron diffraction patterns from 28°C to 500°C . In

order to save time, only the data at low angle were collected. The background from the quartz furnace tube is high, only the four peaks labeled by arrows belong to the $\text{LaFe}_{0.9}\text{Cu}_{0.1}\text{O}_3$ sample. The first one is a purely magnetic peak, and the other three are nuclear peaks. It is clear that the antiferromagnetic ordering disappears between 450°C to 500°C . This value is very close to the Neel temperature of LaFeO_3 (750K). Therefore, 10 mol.% substitution of Fe^{3+} by Cu^{3+} does not reduce the Neel temperature.

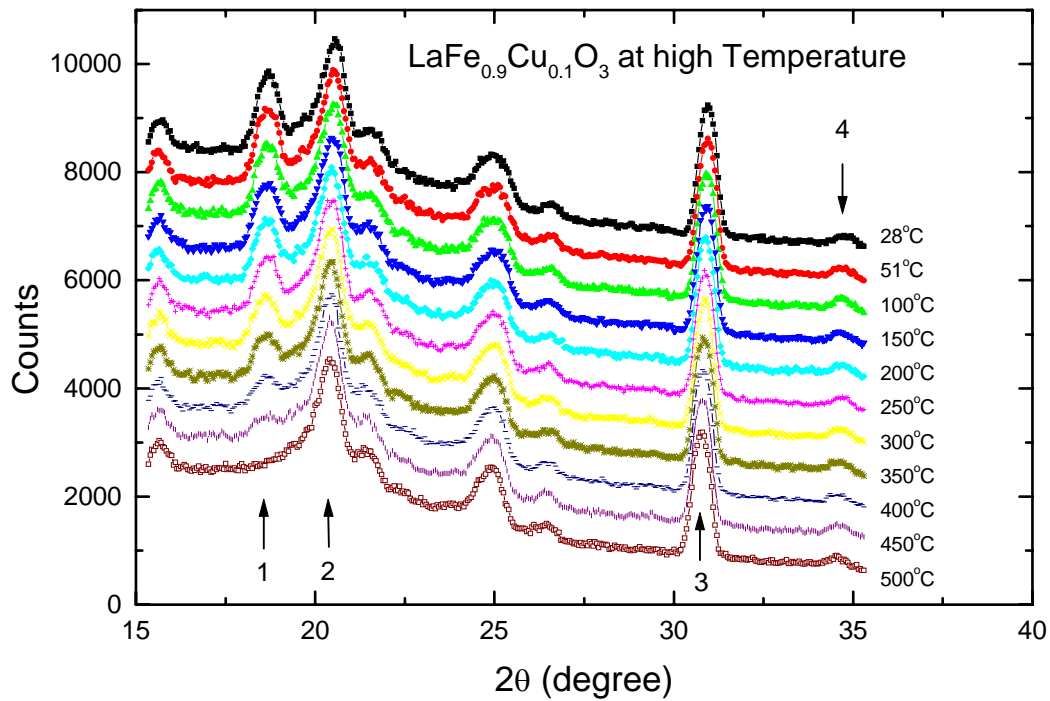


Fig. 4.27: The neutron diffraction patterns of $\text{LaFe}_{0.9}\text{Cu}_{0.1}\text{O}_3$ at high temperature.

In order to find the change of the average magnetic moment at the B site as the temperature increases, the data without magnetic ordering were subtracted from the data with magnetic ordering. The magnetic peak was fitted with a Gaussian shape by using the program ORIGIN. Table 4.16 lists the intensity of the magnetic peak at different temperatures. Since the Debye-Waller factor is very small at low angle, and the intensity

I of the magnetic peak is proportional to the square of the magnetic moment, \sqrt{I} is proportional to the magnetic moment. Figure 4.28 shows \sqrt{I} as a function of the temperature.

Table 4.16: The intensity of the magnetic peak of (1 0 1)/(0 1 1) at different temperatures.

T (°C)	28	51	100	150	200	250	300	350	400	450	500
I	905.52	916.36	843.52	800.12	711.26	625.95	542.16	457.93	345.67	176.67	0
\sqrt{I}	30.09	30.27	29.04	28.29	26.67	25.02	23.28	21.40	18.59	13.29	0

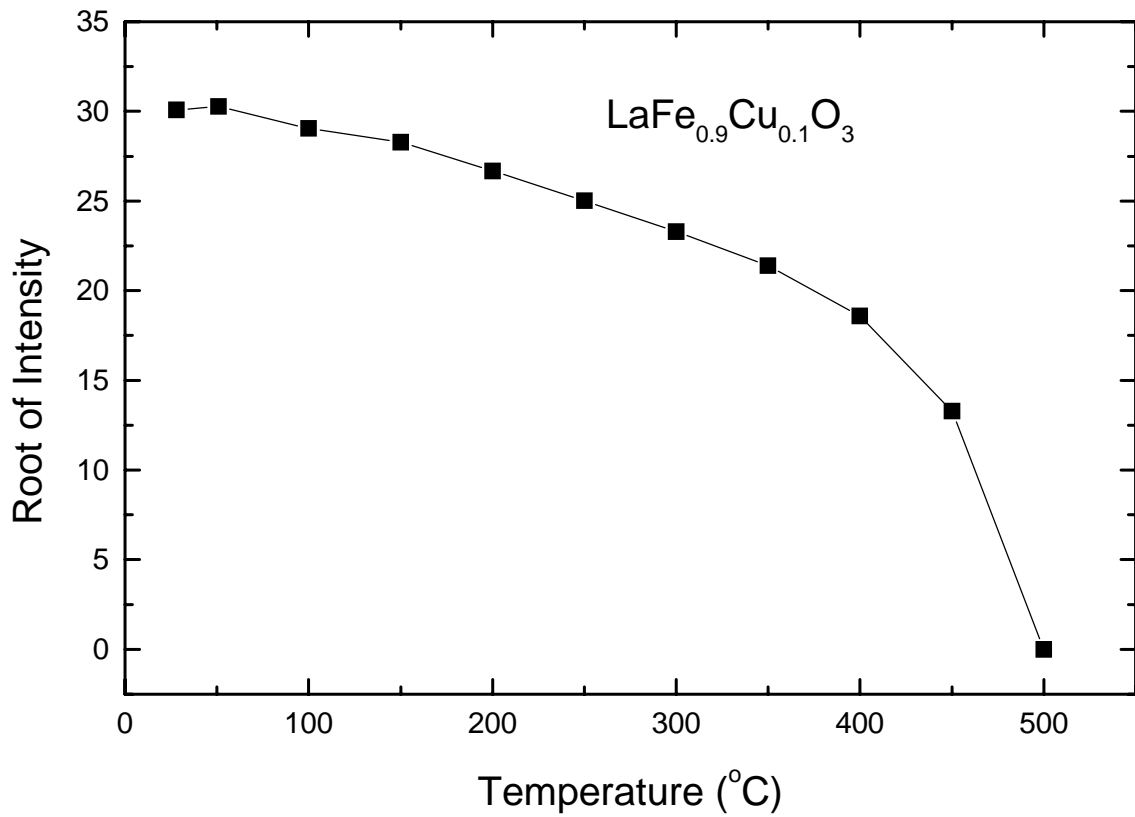


Figure 4.28: The root of the intensity of the magnetic peak (\sqrt{I}) in $\text{LaFe}_{0.9}\text{Cu}_{0.1}\text{O}_3$ vs. temperature.

4.2.4 CONCLUSIONS

Systematic neutron diffraction measurements have been reported for the crystal structure and magnetic properties of $\text{LaFe}_{1-x}\text{Ni}_x\text{O}_3$, $\text{LaFe}_{1-x}\text{Mn}_x\text{O}_3$, and $\text{LaFe}_{1-x}\text{Cu}_x\text{O}_3$. The transition metal ions at the B site are always randomly distributed, i.e., there is no B site ordering for these compounds. Ni- and Mn- doped LaFeO_3 form a continuous series of solid solutions, but the maximum Cu doping in the $\text{LaFe}_{1-x}\text{Cu}_x\text{O}_3$ is 30%. There is a phase transition for both the Ni- and Mn- doped samples. The iron-rich samples are orthorhombic and the Ni- or Mn- rich samples are rhombohedral. The oxygen occupancy is almost stoichiometric for the Ni- or Cu-doped LaFeO_3 , but there is an oxygen excess for the Mn-doped LaFeO_3 , implying vacancies at the A and B sites. Antiferromagnetic ordering was observed for all the iron-rich samples. The Neel temperature decreases with Ni or Mn doping, but Cu doping seems to have no effect on the Neel temperature.

4.3 $\text{La}_{1-x}\text{Sr}_x\text{Fe}_y\text{Co}_{1-y}\text{O}_{3-\delta}$ (LSCF) AND $\text{La}_{0.2}\text{Sr}_{0.8}\text{Fe}_{0.55}\text{Ti}_{0.45}\text{O}_3$ (LSFT)

4.3.1 INTRODUCTION

$\text{La}_{1-x}\text{Sr}_x\text{Fe}_y\text{Co}_{1-y}\text{O}_{3-\delta}$ (LSCF) is another candidate for the cathode of IT SOFCs. The substitution of some Fe by Co can enhance the electrical conductivity and oxygen vacancy concentration, and the two types of transition metal ions on the B sites are always more reactive (for oxygen reduction) than those with only one type of transition metal ion on the B sites. The chemical stability with YSZ and CGO (Gadolinia-doped Ceria) electrolyte were studied by James M. Ralph⁽³²⁾, the results show that the reaction between LSCF and YSZ is slight, and there is no reaction between LSCF and CGO. The perovskite oxide $\text{La}_{0.6}\text{Sr}_{0.4}\text{Fe}_{0.8}\text{Co}_{0.2}\text{O}_{3-\delta}$ (L6SF8C) has been successfully employed in SOFCs operating at 700°C using $\text{Ce}_{0.9}\text{Gd}_{0.1}\text{O}_{1.95}$ (CGO) solid electrolyte^(48, 49, 50). However, the substitution of Fe by Co will increase the TEC, the TEC of $\text{La}_{0.6}\text{Sr}_{0.4}\text{Fe}_{0.8}\text{Co}_{0.2}\text{O}_{3-\delta}$ is $15.3 \times 10^{-6}/^\circ\text{C}$ ⁽⁵¹⁾, which is 22% greater than the TEC of CGO (the TEC of CGO is $12.5 \times 10^{-6}/^\circ\text{C}$ ⁽⁵²⁾). In order to reduce the TEC of L6SF8C, an A-site deficient L6SF8C based perovskite oxide has been studied⁽⁵³⁾. The results show that the TEC is reduced by the A site deficiency.

The Ni+YSZ ceramic anode is widely used in the SOFCs, Ni is an excellent catalyst and electronic conductor, and the YSZ was discovered to constrain Ni aggregation through grain growth at high temperature. But this Ni-based anode has some disadvantages, such as poor redox tolerance, sulfur poisoning, and carbon deposition in hydrocarbon fuels. Nickel is easily oxidized above 500°C; the presence of sulfur or sulfur-containing compounds in the fuel leads to degradation of anode performance even

when the S content is less than 5 ppm. The Ni-based anode is not stable in the presence of hydrocarbons due to hydrocarbon cracking, since Ni is a catalyst for carbon formation.

Current improvements of the anode of SOFCS include the development of a copper/ceria anode for direct oxidation of hydrocarbons. Unlike Ni, Cu is not an active catalyst for carbon formation. Thus, Cu-based cermets dramatically reduce coking and loss of performance^(54, 55). Cu-based anodes show improved sulfur tolerance relative to that of Ni-based anodes.

Recent work has focused on the use of ceramic anode materials based on titanates, such as lanthanum strontium titanate. Titanates are stable in reducing atmosphere at the anode, and are also resistant to coking and sulfur poisoning. At present, the conductivity of titanates is too low to use as the anode alone. However, a number of new compositions, such as $\text{La}_{1-x}\text{Sr}_x\text{Ti}_{1-y}\text{Fe}_y\text{O}_3$ are being investigated^(56, 57). The substitution of Ti by Fe can increase the electrical conductivity and ion conductivity⁽⁵⁷⁾. If an anode can be found that is stable in the reducing atmosphere at the fuel side, resistant to coking and sulfur poisoning, and has large electronic conductivity, the cost of SOFCS could be reduced greatly.

4.3.2 EXPERIMENTAL

Like the LSF samples, the LSCF and LSFT samples are prepared by the liquid-mixing method. LSCF samples are quenched in air from 700-1200°C, and the LSFT samples are quenched in air from 1100-1500°C. The neutron diffraction studies have been carried out at room temperature for all samples, high temperature neutron diffraction measurements have been carried out only for the LSFT samples.

4.3.3 RESULTS AND DISCUSSION

a) $\text{La}_{0.6}\text{Sr}_{0.4}\text{Fe}_{0.8}\text{Co}_{0.2}\text{O}_3$ (L6SFC)

The crystal structure of L6SFC at room temperature is rhombohedral with space group $\bar{P}3c1$, which gives a better fit than the $R\bar{3}c$ space group. The peak at 41° , seen in the L6SF, is also seen here, indicating the $\bar{P}3c1$ space group. Table 4.17 gives the refinement results of L6SFC and Figure 4.29 shows the lattice parameters a^* ($a/\sqrt{2}$) and c^* ($c/2\sqrt{3}$) dependence on the quenching temperature. The rhombohedral distortion becomes small when the quenching temperature is high, but the crystal structure remains rhombohedral up to 1200°C . Since the ionic radii of Co^{3+} ($r=0.61\text{\AA}^{(42)}$) is smaller than that of Fe^{3+} ($r=0.645\text{\AA}^{(42)}$), the rhombohedral distortion becomes smaller when Fe ions are substituted by Co ions.

Figure 4.30 illustrates the dependence of oxygen vacancies, magnetic moment at the B site, and the unit cell volume with the quenching temperature. The sample

Table 4.17: L6SFC refinement with constraints: fraction of O1 ≤ 0.5 . Fraction of O2 is same as O3, and the sum of the fractions of O2 and O3 ≤ 1.0 .

Quench Temp.	a (\AA)	c (\AA)	Vol. (\AA^3)	Total O	Mag. (μ_B)	χ^2	R_{wp}	R_p	Vacancy
700°C	5.50215(16)	13.38267(54)	350.86(2)	2.968(12)	0.62(5)	2.00	5.38	4.33	0.032(12)
800°C	5.50290(15)	13.38712(50)	351.08(2)	2.952(12)	0.72(4)	3.71	6.10	4.91	0.048(12)
900°C	5.50445(15)	13.39823(53)	351.57(2)	2.940(12)	0.78(4)	3.32	6.03	4.90	0.060(12)
1000°C	5.50822(19)	13.43567(71)	353.03(3)	2.880(12)	1.62(2)	4.17	6.98	5.54	0.120(12)
1100°C	5.50676(28)	13.46917(138)	353.72(4)	2.866(14)	2.22(2)	3.92	6.87	5.45	0.134(14)
1200°C	5.50797(28)	13.47328(140)	353.99(5)	2.876(14)	2.23(2)	4.77	7.32	5.82	0.124(14)

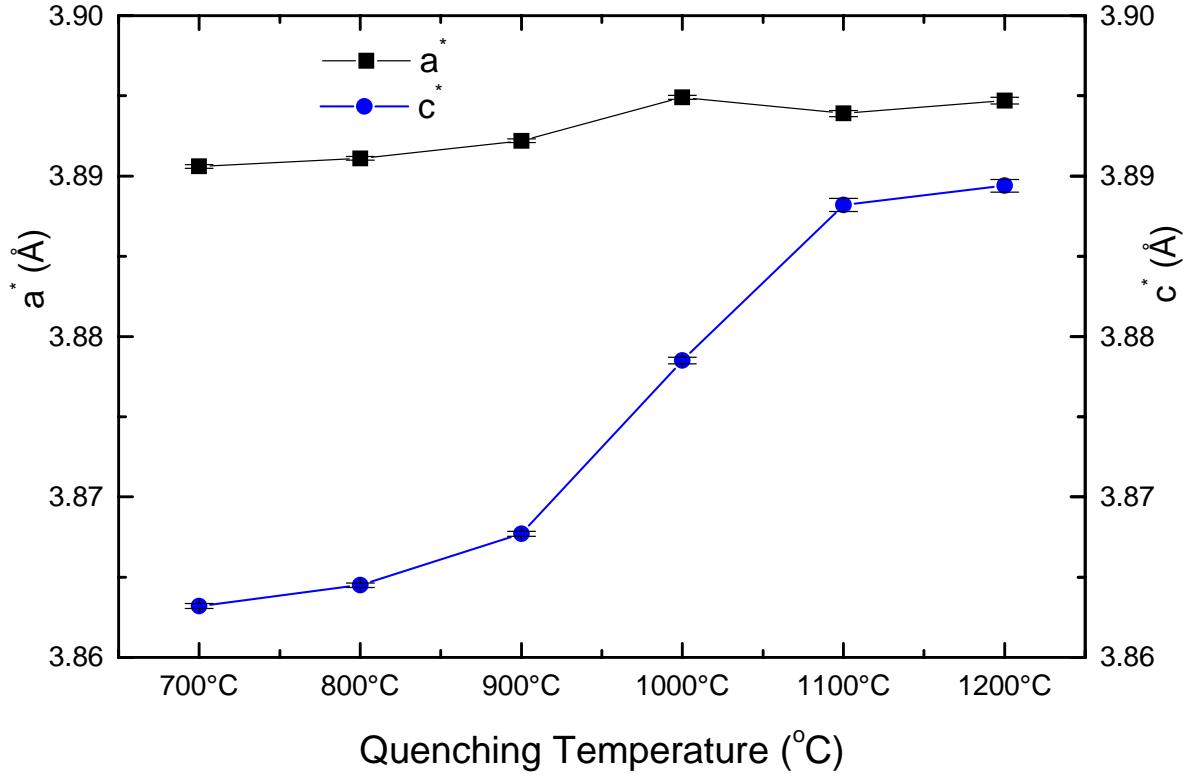


Figure 4.29: Lattice parameter a^* and c^* of L6SF8C vs. the quenching temperature.

quenched from 700°C shows a small fitted oxygen vacancy concentration, approximately 1.1%. At 900°C this increases to 2%, and at 1100°C it is found to be approximately 4.5%. Between 1100°C and 1200°C no change (within statistical uncertainty) is seen. Higher temperature treatments will be needed to determine if this is close to the limiting concentration or an artifact. At all temperatures the vacancy concentration is modestly higher than observed in the L6SF samples since the Co ions on the B sites appear to have a smaller binding energy for oxygen than do Fe ions. The magnetic moment for the 700°C sample is only $0.62\mu_B$, indicating that the Neel temperature for this sample is only slightly above room temperature. The moments increase strongly with increasing

quenching temperature, reaching $2.2\mu_B$ for the 1100°C and 1200°C samples. The smaller value of the moment compared to the L6SF specimen is, at least, partly the result of the smaller Fe content. As was observed for the vacancy concentration, the magnetic moment does not differ significantly for the 1100°C and 1200°C samples. The unit cell volume for these samples shows a similar trend as for the L6SF samples, increasing strongly with vacancy concentration up to about 4% vacancy and then varying more slowly at higher concentration.

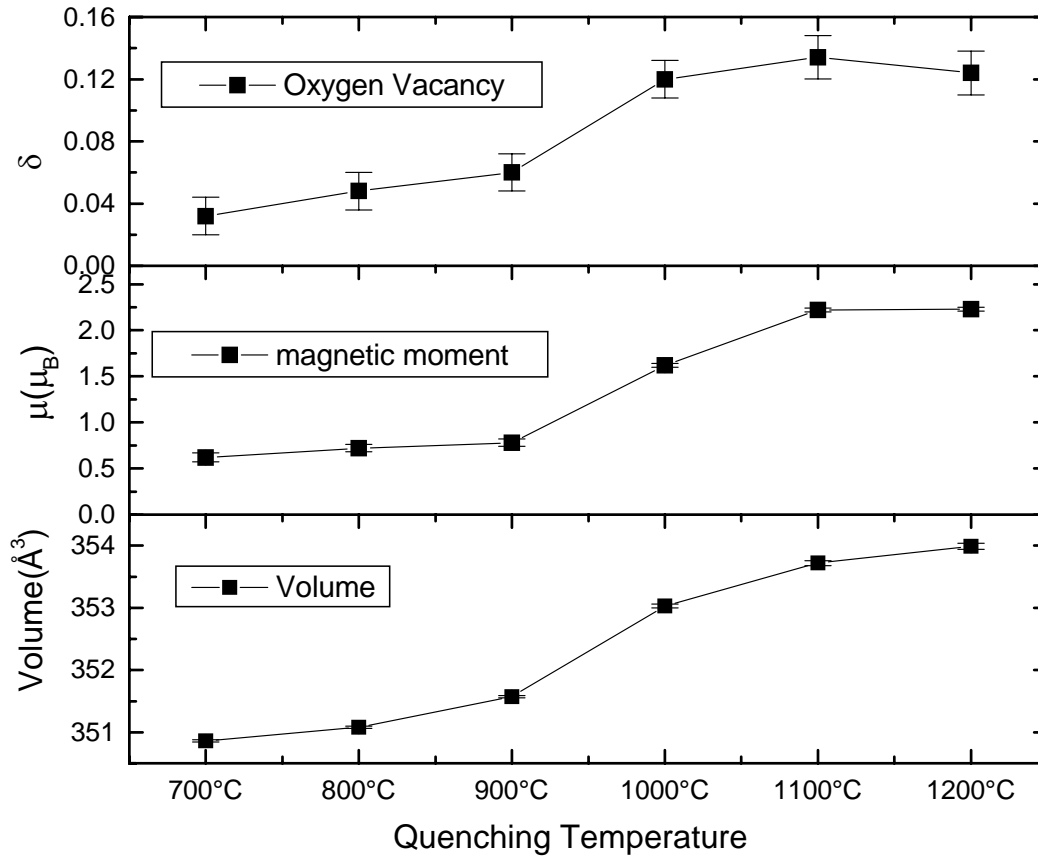


Figure 4.30: The oxygen vacancies, magnetic moment, and unit cell volume of L6SF8C vs. the quenching temperature.

b) $\text{La}_{0.8}\text{Sr}_{0.2}\text{Fe}_{0.8}\text{Co}_{0.2}\text{O}_3$ (L8SFC)

Unlike L8SF, the crystal structure of L8SFC is rhombohedral with space group $R\bar{3}c$. Model 1, described in the L6SF section, was used for the refinement; the large cation, La/Sr, occupies the 6a site with the ratio of La/Sr fixed as 0.8/0.2. The small cation Fe/Co occupies the 6b site with the ratio of Fe/Co fixed as 0.8/0.2, and the oxygen ions occupy the 18e site. Their occupation was refined. The magnetic structure is the same as previously used for model 1.

The refinement results are presented in Table 4.18. The direct refinement shows very few oxygen vacancies for the samples quenched from 700°C and 800°C: approximately 0.6%. The concentration increases to 2.8% for samples quenched from 1100°C and 1200°C. At all temperatures the vacancy concentration is modestly higher than observed in the L8SF samples since the Co ions on the B sites appear to have a smaller binding energy for oxygen than do Fe ions. The magnetic moment of the sample quenched from 700°C is $2.09\mu_B$, and its Neel temperature should be well above the room temperature since the Sr content is low. The magnetic moments are almost the same for the 700°C, 800°C, and 900°C quenched samples, then increases slowly to $2.40\mu_B$ for the 1200°C quenched sample. It is clear that the effect of oxygen vacancy concentration on the room temperature moment is modest since the Neel temperature is well above room temperature. The magnetic moment should be more sensitive to the oxygen vacancy concentration if we measure it at a higher temperature. The unit cell volume is 354.26\AA^3 for the 700°C quenched sample, and increases a little, to 354.79\AA^3 for the 1200°C

quenched sample. Apparently the unit cell volume is not sensitive to the quenching temperature.

Table 4.18: Refinement results for L8SF8C quenched samples. Space group is $R\bar{3}c$, and oxygen is at 18e sites.

T (°C)	a (Å)	c (Å)	x(O)	Occ(O)	μ (μ_B)	Vol (\AA^3)	δ
700°C	5.52698(20)	13.39094(61)	0.5507(3)	2.982(12)	2.09(2)	354.257(24)	0.018(12)
800°C	5.52825(21)	13.39595(65)	0.5505(3)	2.982(12)	2.14(3)	354.552(26)	0.018(12)
900°C	5.52745(20)	13.39575(64)	0.5507(3)	2.976(12)	2.13(2)	354.444(25)	0.024(12)
1000°C	5.52748(20)	13.40482(63)	0.5505(2)	2.946(12)	2.21(2)	354.687(25)	0.054(12)
1100°C	5.52741(20)	13.41600(65)	0.5487(3)	2.916(12)	2.36(2)	354.974(25)	0.084(12)
1200°C	5.52609(20)	13.41561(65)	0.5487(2)	2.916(6)	2.40(2)	354.794(25)	0.084(12)

c) $\text{La}_{0.2}\text{Sr}_{0.8}\text{Fe}_{0.55}\text{Ti}_{0.45}\text{O}_3$ (LSFT)

NEUTRON DIFFRACTION STUDY OF THE AIR-QUENCHED SPECIMEN AT ROOM TEMPERATURE

The crystal structure of LSFT is rhombohedral with space group $R\bar{3}c$ for the non-quenched and 1200°C slowly cooled samples. Its lattice parameters (hexagonal setting) are $a = b \approx \sqrt{2}a_p$; $c \approx 2\sqrt{3}a_p$; $\alpha = \beta = 90^\circ$; and $\gamma = 120^\circ$; where a_p is the lattice parameter of the cubic perovskite cell. There are 6 formula units per unit cell. The large cation La/Sr occupies the 6a site, the small cation Fe/Ti occupies the 6b site randomly, and the oxygen ion occupies the 18e site. For LSFT samples quenched from high temperature (above 1100°C), the structures are believed to be cubic with space group $\text{Pm}\bar{3}m$. There is one formula per unit cell. The large cation La/Sr occupies the 1a site, the small cation Fe/Ti occupies the 1b site, and the oxygen ion occupies the 3d site.

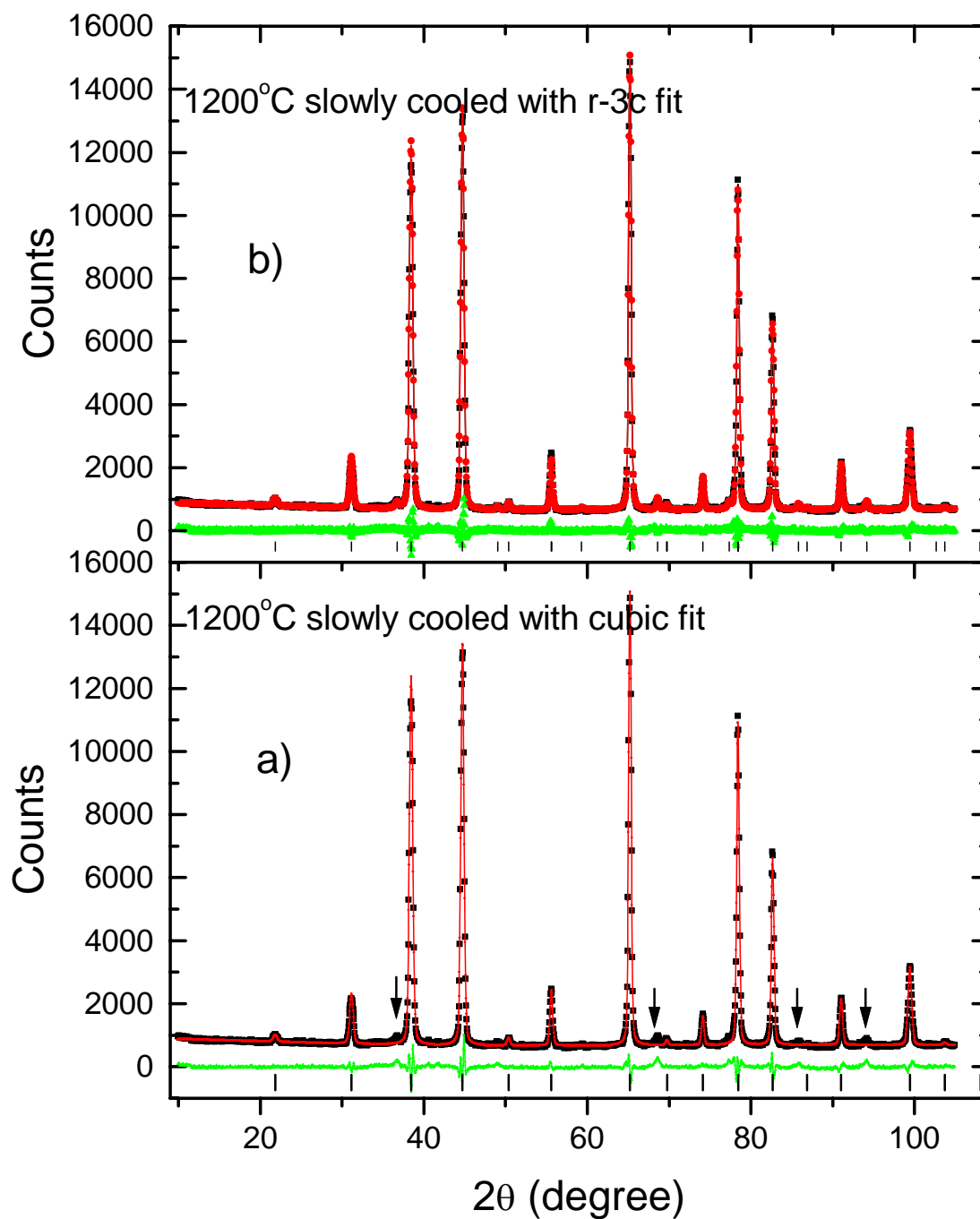


Figure 4.31: Neutron data for the 1200°C slowly cooled LSFT sample fitted by the cubic (a) and rhombohedral (b) structure. For the cubic model, a number of small peaks indicated by arrows are not fitted. For the rhombohedral model, all peaks are fitted well.

Figure 4.31 gives the neutron diffraction patterns fitted by the rhombohedral model (space group $R\bar{3}c$) and the cubic model (space group $Pm\bar{3}m$). For the 1200°C slowly cooled pattern, the cubic model can fit all the main peaks, but many small peaks (indicated by the arrows) can not be fitted (Figure 4.31 a)), and the χ^2 is 3.65. The rhombohedral model can fit all the small peaks (Figure 4.31 b)), and the χ^2 is reduced to 2.66. So the structures of the 1200°C slowly cooled and the unquenched samples are clearly rhombohedral. Since the distortion of this rhombohedral structure is very small, the statistical uncertainties of the lattice parameters a and c are large if they are refined independently. In order to reduce the statistical error, they are constrained as $c = \sqrt{6}a$ in our refinement. For the samples quenched in air above 1100°C, all the small peaks are gone, and the structure is cubic. In order to get a better fit, anisotropic thermal factors for the oxygen atom are used. They are constrained by symmetry to $b_{22} = b_{33}$; and $b_{12} = b_{13} = b_{23} = 0$. The detailed results of the refinement are listed in Table 4.19.

Table 4.19: Refinement results for LSFT ($La_{0.2}Sr_{0.8}Fe_{0.55}Ti_{0.45}O_3$) samples measured at room temperature. The space group is $R\bar{3}c$ for the unquenched and 1200°C slowly cooled samples, and the space group is $Pm\bar{3}m$ for the quenched samples. The Fe and Ti ions occupy the 6b sites (in the $R\bar{3}c$ space group) or the 1b sites (in the $Pm\bar{3}m$ space group) randomly; the ratios of La/Sr and of Fe/Ti are fixed as 0.2/0.8 and 0.55/0.45 respectively.

Sample	a (Å)	c (Å)	x(o)	δ	Occ(O)	Vol. (Å ³)	χ^2
1200°C s c	5.50823(2)	13.49430(86)	0.51385(25)	0.012(12)	2.988(12)	354.572(23)	2.66
No Quench	5.51077(2)	13.50060(95)	0.51229(32)	0.036(12)	2.964(12)	355.065(25)	2.36
1100°C 24h	3.90568(10)			0.154(14)	2.846(14)	59.579(3)	2.64
1200°C 24h	3.90691(11)			0.149(19)	2.851(19)	59.635(3)	3.63
1300°C	3.90849(12)			0.168(19)	2.832(19)	59.707(3)	3.99
1400°C 10s	3.90742(10)			0.154(14)	2.846(14)	59.658(3)	3.09
1500°C	3.90804(11)			0.130(19)	2.870(19)	59.687(3)	3.81

Unlike the LSF specimen, there was no evidence for magnetic ordering in the neutron diffraction data of LSFT at room temperature. The observed data could be fully fitted by the nuclear phase only. The high Sr content in the A sites and the substitution of Fe by the nonmagnetic atom Ti destroys the magnetic ordering.

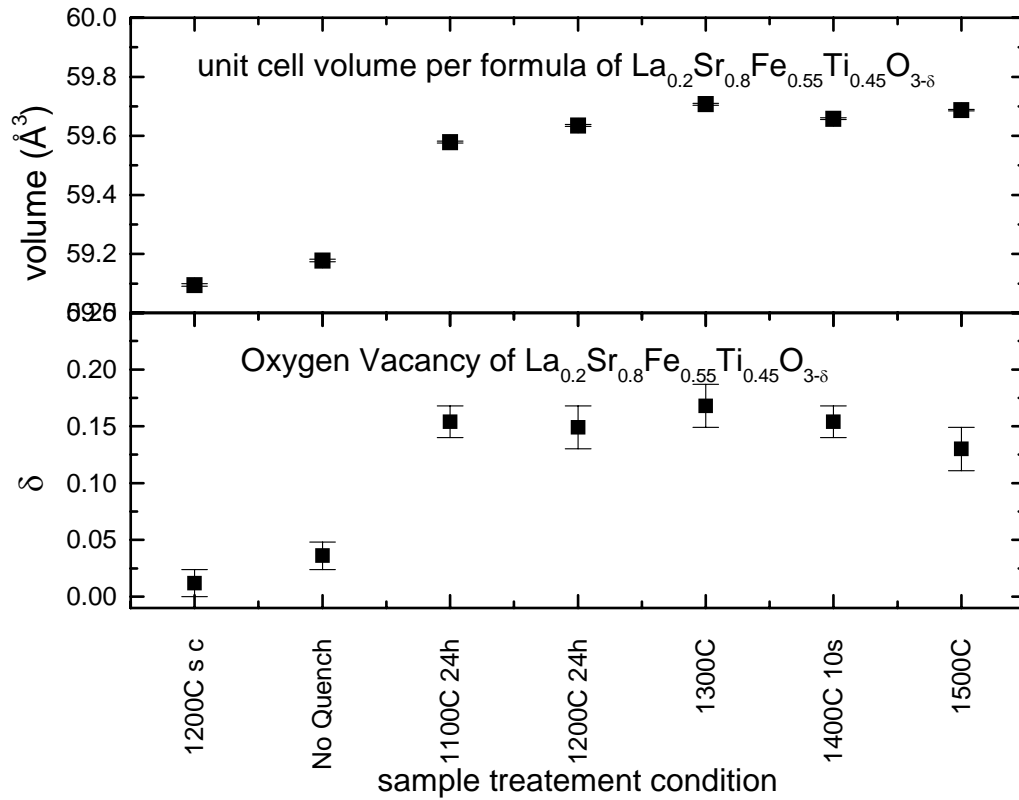


Figure 4.32: The oxygen vacancy and the unit cell volume per formula as a function of the LSFT sample treatment conditions.

Figure 4.32 shows the oxygen vacancy concentration and the cell volume per formula unit as a function of the sample treatment condition. The oxygen vacancy concentration is quite small for the 1200°C slowly cooled and unquenched samples. It becomes large when the quench temperature is above 1100°C, and it seems that there is little or no change with the quench temperature up to 1500°C. It shows that there is an

oxygen vacancy limit for the samples quenched in air above 1100°C. The average oxygen vacancy concentration δ of the quenched samples is 0.151, and the average valence of Fe is about 3.09 if we assume the valence of Ti is +4. Therefore, there are some Fe^{4+} ions in these samples.

The cell volume is closely correlated with the oxygen vacancy concentration. It is small for the 1200°C slowly cooled and unquenched samples, while it is large for the samples quenched in air above 1100°C and shows only small changes with the quench temperature up to 1500°C.

IN-SITU NEUTRON DIFFRACTION STUDY OF LSFT HEATED UP TO 900°C WITH AIR AND N₂ FILLING

The LSFT specimen for the in-situ neutron diffraction study was sintered at 1400°C for 2 hours and then cooled to room temperature at 3 °C/min. The specimen is bar shape with a geometry 35mm x 3mm x 3mm. It was first measured at room temperature outside the furnace, then the in-situ neutron diffraction studies at high temperature (up to 900 °C) with air or N₂ filling were performed.

Unlike the unquenched sample and the 1200 °C slowly cooled sample, the crystal structure of the bar shape sample at all temperatures is cubic, there are no small peaks unfitted by the $\text{Pm}\bar{3}\text{m}$ space group. The refinement results are given in the Tables 4.20 and 4.21. In these refinements, the anisotropic thermal factors and their constraints for the oxygen atom are used, as above, and the thermal parameters increase as the temperature increases. The thermal parameters at room temperature are larger than those at 97 °C. This is an artifact related to absorption by the furnace.

Table 4.20: Refinement results for LSFT 1400°C bar sample at high temperature with air filling. Sample is cubic structure with space group $Pm\bar{3}m$, La/Sr is at 1a site, Fe/Ti is at 1b site, and O is at 3d sites. The ratio of La/Sr is fixed as 0.2/0.8, and the ratio of Fe/Ti is fixed as 0.55/0.45. The anisotropic thermal parameters are constrained as $b_{22}=b_{33}$, and $b_{12}=b_{13}=b_{23}=0$. b_{11} and b_{22} are timed by 10^4 .

T (°C)	B(A) (\AA^2)	B(B) (\AA^2)	b_{11} (\AA^2)	b_{22} (\AA^2)	Occ(O)	a (\AA)	Vol (\AA^3)
RT	1.883(48)	1.151(64)	270.6(12.8)	504.3(10.7)	0.618(3)	3.90091(11)	59.360(3)
97	0.908(58)	0.732(82)	148.9(15.0)	390.6(12.5)	0.633(5)	3.91135(11)	59.838(3)
198	1.089(61)	0.910(87)	167.4(15.6)	414.4(13.0)	0.631(5)	3.91680(12)	60.089(3)
294	1.252(61)	1.088(87)	180.4(15.2)	457.6(12.9)	0.633(5)	3.92220(12)	60.338(3)
401	1.348(65)	1.097(92)	190.5(16.2)	466.8(13.7)	0.630(5)	3.92820(12)	60.615(3)
504	1.627(70)	1.437(99)	224.7(17.4)	496.5(14.3)	0.628(5)	3.93440(13)	60.903(4)
598	1.559(67)	1.338(95)	221.6(16.4)	521.8(13.8)	0.633(5)	3.94033(12)	61.178(3)
696	1.734(71)	1.550(102)	247.6(17.3)	578.1(14.5)	0.634(5)	3.94723(13)	61.500(4)
798	2.004(78)	1.919(112)	276.1(18.7)	608.4(15.5)	0.624(6)	3.95507(14)	61.867(4)
891	2.542(72)	2.316(101)	292.3(16.7)	676.1(14.1)	0.611(5)	3.96096(14)	62.144(4)

Table 4.21: Refinement results for LSFT 1400°C bar sample at high temperature with N₂ filling. Sample is cubic structure with space group $Pm\bar{3}m$, La/Sr is at 1a site, Fe/Ti is at 1b site, and O is at 3d sites. The ratio of La/Sr is fixed as 0.2/0.8, and the ratio of Fe/Ti is fixed as 0.55/0.45. The anisotropic thermal parameters are constrained as $b_{22}=b_{33}$, and $b_{12}=b_{13}=b_{23}=0$. b_{11} and b_{22} are timed by 10^4 .

T(°C)	B(A) (\AA^2)	B(B) (\AA^2)	b_{11} (\AA^2)	b_{22} (\AA^2)	Occ(O)	a (\AA)	Vol. (\AA^3)
100	0.907(55)	0.845(80)	183.0(14.5)	367.4(11.5)	0.642(5)	3.90991(11)	59.772(3)
200	1.173(61)	1.046(87)	184.2(16.0)	368.6(12.5)	0.630(5)	3.91662(12)	60.081(3)
296	1.284(62)	1.152(88)	205.3(15.8)	404.0(12.6)	0.633(5)	3.92122(12)	60.292(3)
403	1.487(64)	1.343(91)	225.9(16.1)	449.1(12.9)	0.640(5)	3.92713(12)	60.566(3)
503	1.654(67)	1.525(94)	250.7(16.7)	478.9(13.2)	0.640(5)	3.93212(12)	60.797(3)
601	1.735(61)	1.577(87)	248.1(15.2)	491.2(12.2)	0.630(5)	3.93727(11)	61.036(3)
698	1.996(71)	1.886(101)	278.4(17.2)	558.8(13.9)	0.626(5)	3.94721(13)	61.500(4)
802	2.743(73)	2.454(102)	357.0(17.5)	665.4(14.1)	0.616(5)	3.94995(13)	61.627(4)
893	2.789(69)	2.676(99)	322.4(15.9)	719.5913.4)	0.611(4)	3.95599(13)	61.911(3)

Figures 4.33 and 4.34 show that the oxygen occupancies and the lattice parameters as a function of temperature. In Fig. 4.33, the oxygen occupancy refined at room temperature is 2.966, and the oxygen vacancy δ is 0.034. But in the temperature range 100°C-700°C, the refined oxygen occupancy is a little above 3. The slight increase of oxygen occupancy at 100 °C is very unlikely since the temperature is too low to let the perovskite absorb oxygen. There may be a small systematic error due to the neutron absorption of the heater, and the statistical error of the oxygen occupancy measured at high temperature is bigger than the one measured at room temperature. As can be seen, the oxygen deficiency starts to increase with temperatures higher than 700 °C. The lattice parameter a , measured at room temperature, deviates from the linear extension of other measurements, and could be the result of the change of sample position between the room temperature and high temperature measurements. The lattice parameter increases a little faster at higher temperature, which indicates the formation of oxygen vacancies. The average TEC in the 100-900°C range is about $16.0 \times 10^{-6}/^{\circ}\text{C}$. For the N₂ filling case (Fig. 4.34), the refined oxygen occupancy is a little above 3 when the temperature is below 700 °C; oxygen vacancies appear when the temperature is above 700 °C. The lattice parameter a is linear with temperature below 600 °C, the rapid increase of a above 700 °C indicates the presence of more oxygen vacancies. The average TEC in the 100-900 °C range is $14.9 \times 10^{-6}/^{\circ}\text{C}$.

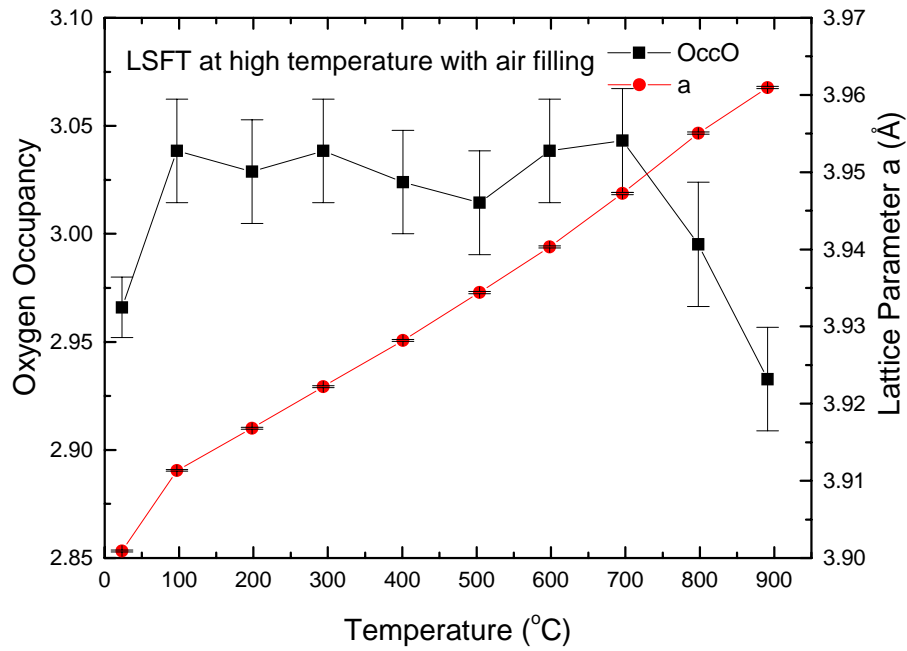


Figure 4.33: The oxygen occupancy and lattice parameter a of LSFT vs. temperature with air filling.

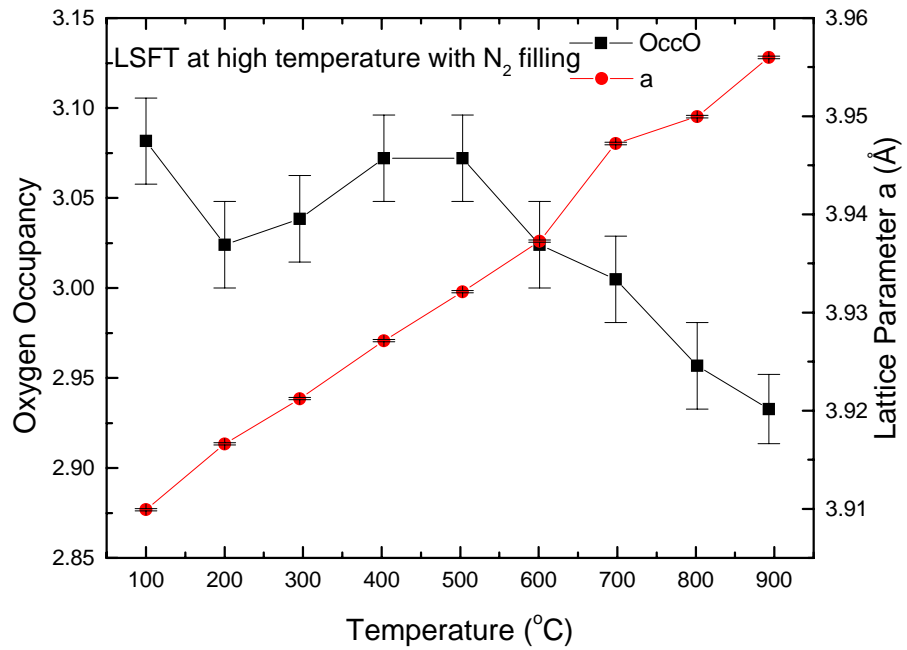


Figure 4.34: The oxygen occupancy and lattice parameter a of LSFT vs. temperature with N₂ filling.

4.3.4 CONCLUSIONS

Neutron diffraction studies show that the crystal structure of LSCF samples quenched at different high temperatures is rhombohedral, and all these samples show antiferromagnetic ordering at room temperature. Oxygen vacancies are present when the quenching temperature is higher than 700 °C, and increase with temperature. At all quenching temperatures, the oxygen vacancy concentration is higher than observed in the LSF samples since the Co ions have a smaller binding energy for oxygen than do Fe ions. The crystal structure of LSFT samples quenched at high temperature is cubic with space group $Pm\bar{3}m$, but there is a little rhombohedral distortion for the no quenching and slowly cooled samples. The oxygen vacancy concentration is small for the slowly cooled and no quenching samples, but is large for the samples quenched at high temperature. The TEC of LSFT slowly cooled sample in air is about $16.0 \times 10^{-6} / ^\circ\text{C}$, and the oxygen vacancies are present when the temperature is higher than 700 °C.

$\text{Ba}_2\text{YRu}_{0.85}\text{Cu}_{0.15}\text{O}_6$ SUPERCONDUCTOR

5.1 INTRODUCTION

Superconductivity in the double perovskites $\text{AE}_2\text{Y}(\text{Ru}_{1-x}\text{Cu}_x)\text{O}_6$ ($0.05 < x < 0.15$), where AE is an alkaline-earth element Ba or Sr, was reported in 1997 by Wu et al. and Chen et al.,⁽¹⁴⁻¹⁵⁾ and the superconductivity of $\text{Sr}_2\text{YRu}_{0.9}\text{Cu}_{0.1}\text{O}_6$ was confirmed by H. A. Blackstead in 2000⁽¹⁶⁾. The superconductivity of these double perovskite materials is of special interest since they are quite different from the cuprate superconductors. First, there are no CuO_2 planes in the double perovskite superconductors, and it has been broadly held that the superconducting electrons are located in the CuO_2 plane in the cuprate superconductors. Second, there is magnetic ordering in the $\text{Y}(\text{Ru}, \text{Cu})\text{O}_4$ planes in the double perovskite superconductors and this magnetic ordering coexists with the superconducting ordering. The coexistence of superconductivity and antiferromagnetism is surprising since these two orderings are expected to compete with each other and apparently do not coexist in the cuprate superconductors.

It has been argued that the superconductivity observed in $\text{Ba}_2\text{YRu}_{1-x}\text{Cu}_x\text{O}_6$ arises from an undetected impurity $\text{YBa}_2\text{Cu}_3\text{O}_{7-\delta}$ (Y123), since all of the elements of Y123 are present in the starting mixture for the synthesis of $\text{Ba}_2\text{YRu}_{1-x}\text{Cu}_x\text{O}_6$ ⁽⁵⁸⁾. This argument has been made despite the fact that the maximum content of Y123 is much lower than that required for bulk percolation (about 16%) even if all the Cu were incorporated in the Y123 phase. Percolating superconductivity (zero resistance) has been observed by Wu et

al.⁽¹⁴⁻¹⁵⁾ and Blackstead et al..⁽¹⁶⁾ In addition, Y123 undergoes a peritectic decomposition at 1020 °C⁽⁵⁹⁾ and the resulting products undergo a second decomposition at 1270 °C,⁽⁶⁰⁾ while the sintering temperature for the synthesis of $\text{Ba}_2\text{YRu}_{1-x}\text{Cu}_x\text{O}_6$ is 1450 °C. Since the $\text{Ba}_2\text{YRu}_{1-x}\text{Cu}_x\text{O}_6$ phase is stable at much higher temperatures, it is very unlikely it will decompose upon cooling through the lower decomposition temperature of the Y123 phase. Furthermore, the O6 samples are not subject to a low temperature (450-500°C) oxygen anneal, usually required to produce superconductivity in the Y123 phase.

Powder neutron diffraction was used to study a $\text{Ba}_2\text{YRu}_{0.85}\text{Cu}_{0.15}\text{O}_6$ superconductor with a transition temperature of 84K as well as a mixture of Ba_2YRuO_6 and 5wt% Y123. The mixed material was subjected to the processing conditions appropriate to the synthesis of the $\text{Ba}_2\text{YRu}_{0.85}\text{Cu}_{0.15}\text{O}_6$ phase, and characterized after each step. The $\text{Ba}_2\text{YRu}_{0.85}\text{Cu}_{0.15}\text{O}_6$ phase is a cubic double perovskite with space group $\text{Fm}\bar{3}\text{m}$. Incommensurate magnetic ordering of Cu is observed coincident with the onset temperature of superconductivity (84K), while the Ru sublattice orders at about 37K. The Rietveld refinement of a nominally stoichiometric sample of $\text{Ba}_2\text{YRu}_{0.85}\text{Cu}_{0.15}\text{O}_6$ reported a small amount of Y123 (2wt%) as an impurity phase present in the $\text{Ba}_2\text{YRu}_{0.85}\text{Cu}_{0.15}\text{O}_6$ superconductor, although some strong reflections of Y123 were not observed. The fit is based on fitting only very weak peaks and is subject to considerable uncertainty, as the observed peaks may arise from other unidentified impurities based on perovskite like structures. Decomposition of the $\text{Ba}_2\text{YRu}_{0.85}\text{Cu}_{0.15}\text{O}_6$ was not observed. Heat treatment of the mixed material showed that the Y123 phase was converted into the thermodynamically stable Cu-doped O6 phase at high temperature.

5.2 EXPERIMENTAL

The preparation of polycrystalline $\text{Ba}_2\text{YRu}_{0.85}\text{Cu}_{0.15}\text{O}_6$ closely follows the procedure given by Wu et al.⁽¹⁴⁾ The starting materials, oxides of Y, Cu, Ru, and Ba carbonate, were mixed in stoichiometric proportions from materials dried at temperatures of 300-500 °C. The powders were hand-ground in an agate mortar for several hours, and calcined at 970 °C for 2 days. Low-energy ball milling alone was found to be ineffective for producing homogeneous samples, although it works well for the cuprates. The calcined powders were reground, and pressed at 10,000 psi into small pellets of approximately 1.5 grams. Two or three pellets were stacked on the remaining calcined powder, to avoid contamination from the crucible, and sintered in a reactant gas mixture of 70% Ar and 30% O₂ for 12 hours at 1450 °C. Multiple calcinations, for long times, at lower temperature were found to be ineffective for producing the desired product phase. This is thought to be due to loss of Ru, which is known to volatilize at temperatures as low as 800 °C. Pellet densification is important; the same procedure using less dense 3-4 gram pellets failed to yield superconducting materials, presumably due to poorer diffusion and consequent component volatility. The sintered pellets are much harder than those of Y123. A mixture of Ba_2YRuO_6 and 5wt% Y123 was prepared and subjected to the same heat treatment schedule as employed for the syntheses described above. High statistics neutron diffraction was carried out at MURR at room temperature and low temperature to find the crystal and magnetic structure of the O6 phase and the impurity phase.

5.3 RESULTS AND DISCUSSION

a) $\text{Ba}_2\text{YRu}_{0.85}\text{Cu}_{0.15}\text{O}_6$

CRYSTAL STRUCTURE

A Cu-doped Ba_2YRuO_6 sample was prepared at the University of Notre Dame with the synthesis method described above. The magnetization and resistivity measurements show that it is a superconductor with $T_c=84\text{K}$. The sample was contained in a $\phi 3\text{mm}$ vanadium can, and a BN sample stopper was used to raise the sample to beam center, since the sample volume was not enough to fill the vanadium can. Data over the angular range $5^\circ < 2\theta < 105^\circ$ were collected at room temperature and 16K, and these data enabled us to determine the crystal and magnetic structures. High statistics data over the first angular scan range of the detector ($5^\circ < 2\theta < 25^\circ$) were collected at temperatures from 16K to 95K, and these data allowed us to follow the magnetic ordering at different temperatures.

The full neutron diffraction spectrum at room temperature is plotted in Fig. 5.1a. This profile is enlarged in the Y scale in order to show the low intensity peaks clearly. The peaks indicated with arrows with a down direction can be indexed with (odd, odd, odd) Miller indexes, and the presence of these peaks, which are not allowed in the simple perovskite structure, shows that the unit cell is doubled in all three directions. This proves that the Y and Ru ions are ordered on the B and B' sites, but the intensities are contributed primarily by the oxygen atoms which are shifted from the ideal position of the simple perovskite. The two profiles are refined with a cubic double perovskite structure with space group $\text{Fm}\bar{3}\text{m}$, and its unit cell volume is $2a_p \times 2a_p \times 2a_p$ (where a_p is the unit cell parameter a of the simple cubic perovskite). As expected, there is no

octahedral tilting in this structure since the size of the Ba^{2+} is large and the tolerance factor is 0.995, which is very close to 1.

The refined structural parameters at room temperature are listed in Table 5.1. The large A cation, Ba^{2+} , occupies the 8c site; the small B cations, Y^{3+} , Ru^{5+} , and Cu^{3+} , occupy the two B sites, 4a and 4b; and the oxygen ion occupies the 24e site. The space group $\text{Fm}\bar{3}\text{m}$ allows an ordered 1:1 arrangement of the B cations, namely Ru, Cu, and Y, over the two B sites 4a and 4b. Due to the size difference, however, it is expected that the Ru and Cu would equally avoid the Y site. Assuming the Y site to be fully occupied, we find that the Ru site contains the nominal Cu, but the uncertainty on this value is large (~50%) due to low contrast of the scattering lengths. Microprobe (Energy Dispersive x-ray Analysis) confirms that Cu and Ru are present at the stoichiometric ratio in large cubic grains. The refinement reaches convergence at two oxygen positions, (0.23445, 0, 0) and (0.26563, 0, 0). These two positions are symmetric relative to the ideal oxygen position (0.25, 0, 0). The second one is reasonable since the bond length of $L_{\text{Y-O}}$ is 2.212(3) Å, and $L_{\text{Ru(Cu)-O}}$ is 1.952(3) Å. The alternate choice leads to a lengthened Ru-O distance and shortened Y-O distance and is, therefore, rejected. The displacement of the oxygen ion from its ideal position is further indirect evidence for the B sites ordering, and the (odd, odd, odd) peaks are mainly due to the displacement of the oxygen ion from its ideal position. Figure 5.2a shows the unit cell of this cubic double perovskite. Note that the YO_6 octahedra are larger than the Ru(Cu)O_6 octahedra.

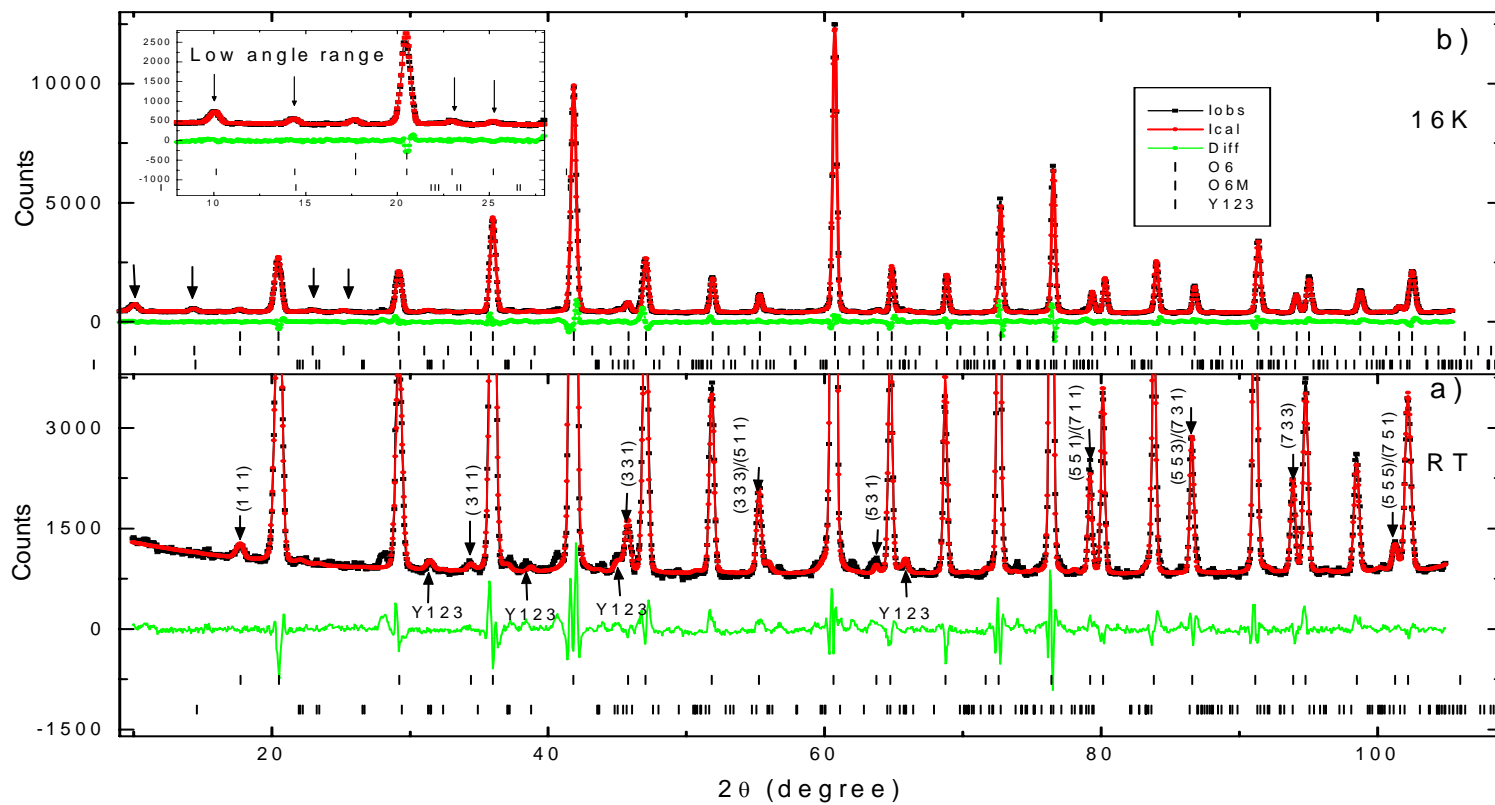


Figure 5.1: The neutron diffraction profiles of $\text{Ba}_2\text{YRu}_{0.85}\text{Cu}_{0.15}\text{O}_6$ at a), room temperature and b), 16K.

Table 5.1: Structural parameters of $\text{Ba}_2\text{YRu}_{0.85}\text{Cu}_{0.15}\text{O}_6$ at room temperature. The unit cell is cubic with lattice parameter $a=8.32859(16)$ Å, and the space group is $Fm\bar{3}m$.

Atom	Site	x	y	z	B (\AA^2)	Occ.
Ba	8c	0.25	0.25	0.25	0.55(4)	1.0
Y	4a	0	0	0	0.27(4)	1.0
Ru	4b	0.5	0.5	0.5	0.68(5)	0.90(5)
Cu	4b	0.5	0.5	0.5	0.68(5)	0.10(5)
O	24e	0.26563(11)	0	0	0.86(2)	1.004(8)

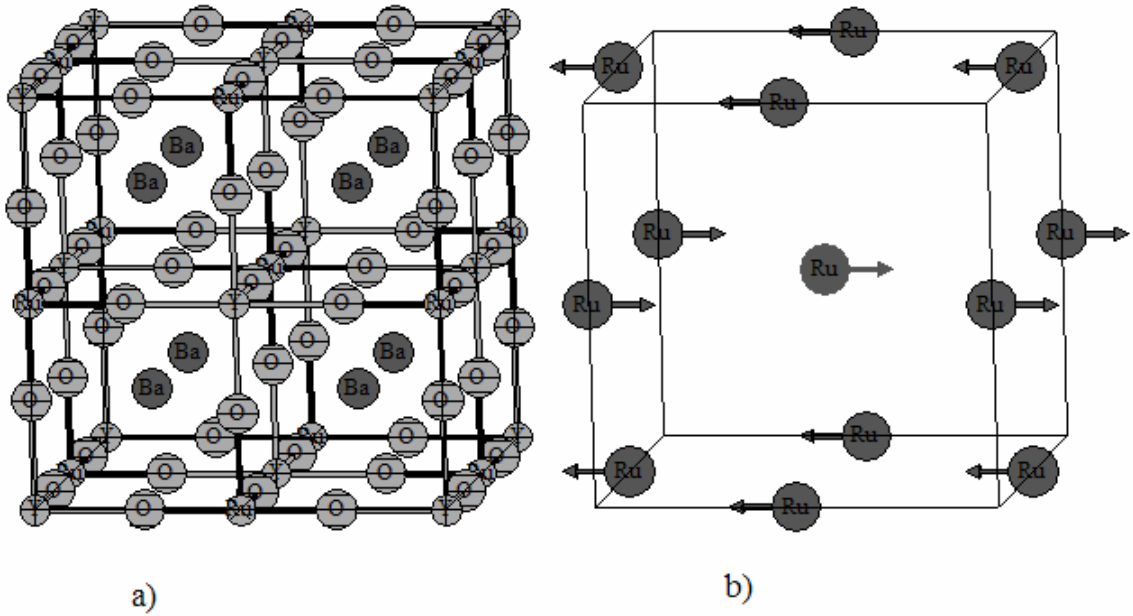
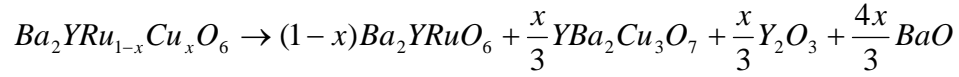
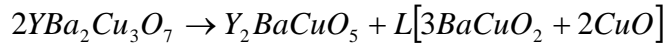


Figure 5.2: a) Crystal structure of $\text{Ba}_2\text{YRu}_{0.85}\text{Cu}_{0.15}\text{O}_6$; b) Magnetic structure of $\text{Ba}_2\text{YRu}_{0.85}\text{Cu}_{0.15}\text{O}_6$.

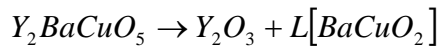
Galstyan et al.⁽⁵⁸⁾ suggested that the Cu could separate out of the calcined mixture and form Cu-rich phases. The neutron diffraction study may allow us to follow the possible decomposition of $Ba_2YRu_{1-x}Cu_xO_6$ to produce Y123 and undoped Ba_2YRuO_6 . The proposed decomposition of $Ba_2YRu_{1-x}Cu_xO_6$ is as follows:



For a dopant content of $x=0.15$, complete decomposition would result in 5% (molar) Y_2O_3 and Y123, with 20% (molar) BaO. These potential products would be of interest only if they are stable at 1450 °C, the sintering temperature of $Ba_2YRu_{1-x}Cu_xO_6$. But the Y123 is not. It undergoes a peritectic decomposition at about 1020 °C as follows:⁽⁵⁹⁾



Here, Y_2BaCuO_5 (Y211) is the non-superconducting ‘green’ phase, and L indicates the liquid phase. Y211 decomposes at a higher temperature (1270°C) as follows:⁽⁶⁰⁾



Thus, the proposed product Y123 is not thermodynamically stable at the sintering temperature. The final products, such as Y_2O_3 , CuO, $BaCuO_2$, and BaO, were tested to fit the data as secondary phases, but none were found. The intermediate compounds, Y123 and Y211, were used to fit the data as secondary phases also, but a maximum of 2% wt of Y123 could be considered to be the impurity in this sample. All the peaks of Y123 are indicated by the arrows with up direction in Fig. 5.1a. The amount of Y123 is too small to be the origin of the magnetization and resistivity data.

Some⁽⁵⁸⁾ have argued that Y123 could form epitaxially on the surface of the O6 grains, due to the presence of similar BaO planes in both structures and that these thin epitaxial layers would be invisible to neutron or x-ray diffraction. In fact, the cell parameters of the O6 (8.3286Å) are substantially larger than twice the basal axes of Y123, and phase separation, rather than epitaxy, is more likely if Y123 were to appear. In any case, no similar “cloak of invisibility” can be invoked to hide the 20% (molar) BaO which would accompany the needed 5% (molar) Y123. The absence of BaO (or BaCO₃) rules out phase separation of the Cu from the O6 phase and therefore excludes Y123 as a decomposition product. Moreover, the absence of BaO in the sample is also confirmed by its air stability, because the BaO rapidly transforms to BaCO₃, which will swell and break the sample to a fine powder. This is in striking contrast to experience in which samples have changed little in either appearance or properties with more than a year’s exposure to ambient air. Of course, this behavior also contrasts sharply with Y123, which deteriorates rapidly when exposed to ambient air. As a test, a mixture of Ba₂YRuO₆ and 20% BaCO₃ was calcined and sintered at Notre Dame. Within 24 hours of air exposure it crumbled.

MAGNETIC STRUCTURE

The large angular range neutron diffraction profile at 16K is plotted in Fig. 5.1b. The four peaks at low angle, indicated with arrows, are pure magnetic peaks, which show that there is antiferromagnetic ordering at the Ru sites. All the magnetic peaks can be fitted by a type I magnetic structure: the Ru⁵⁺ ions in the same (0, 0, l) planes are ferromagnetically ordered, but in adjacent (0, 0, l) planes, they are antiferromagnetically coupled, as illustrated in Fig. 5.2b. The moments lie in the basal plane but their direction

cannot be obtained since the structure is cubic. In the refinement, the direction is set along the b axis, and the Ru^{5+} ions are the only magnetic ions. The refined magnetic moment of Ru^{5+} is $2.38(7) \mu_B$, which is consistent with the moment reported by Parkinson⁽⁶¹⁾. The magnetic Ru^{5+} ions form a face centered cubic array. There are two principal magnetic superexchange interactions in such a structure: that between nearest-neighbor ions, separated by a distance of $\sqrt{2}a_p$, and that between next-nearest-neighbor ions, separated by a distance of $2a_p$. High temperature magnetization studies show strong Ru-Ru antiferromagnetic coupling. However, simple antiferromagnetism is frustrated in FCC structures, and ordering temperature is strongly depressed.

In Fig. 5.3, neutron diffraction data at several temperatures from 16K to 95K are given, focusing on the low angular range, which includes the first three pure magnetic peaks at about 9.9° , 14.2° , and 22.8° . The long range Ru^{5+} antiferromagnetic ordering disappears between 35K and 38K. But, above 38K, the data show the presence of a single broad peak, which is incommensurate with the lattice. This broad peak position varies from approximately 9.9° at 38K to 11° at 85K, and cannot be attributed to short-range order of the Ru, which should be centered at the Bragg position. The broad peak is most likely due to incommensurate antiferromagnetic ordering of Cu. This peak is consistent with the presence of a sinusoidal spin-density-wave (SDW), associated with the Cu dopant, and the SDW appears to lock to the Ru sublattice when Ru is ordered.

The data collection is time consuming (24h) and the broad peak is weak. It was therefore important to confirm that the broad peak was produced by the sample only. Figure 5.4 shows two neutron diffraction profiles at 45K, one is for the sample, and the

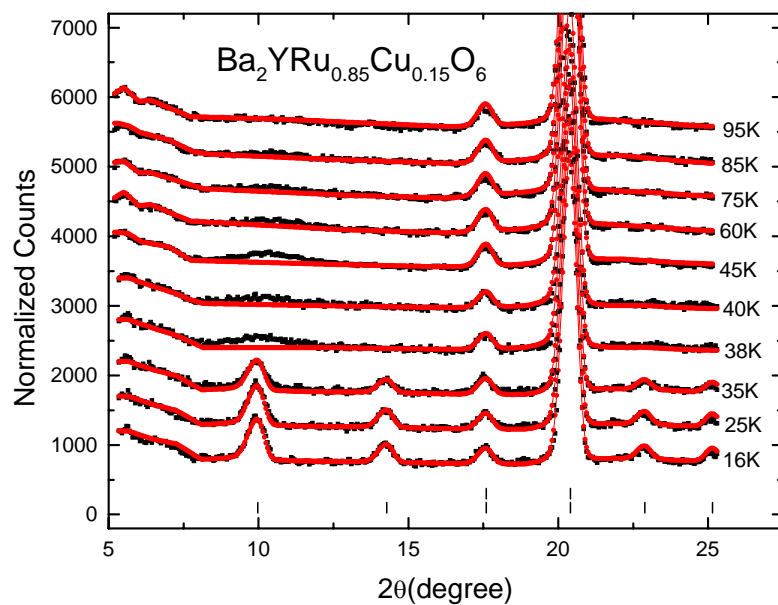


Figure 5.3: Low angle neutron diffraction data as a function of temperature from 16K to 95K.

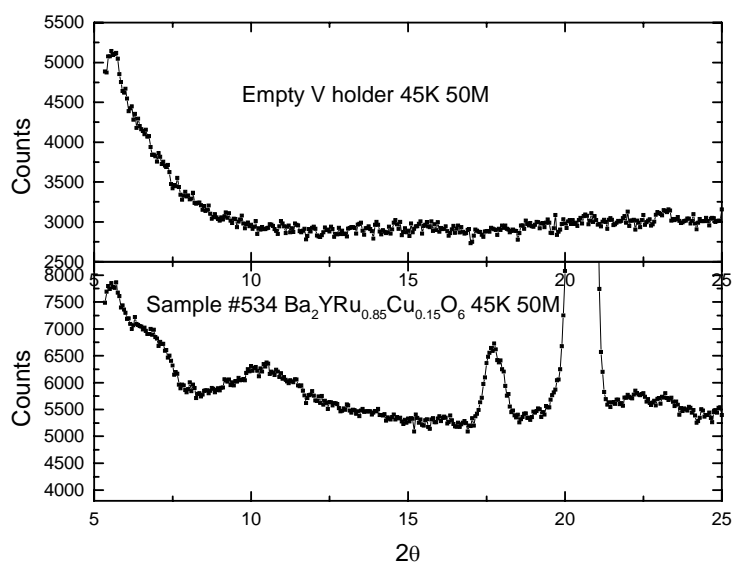


Figure 5.4 Comparison of neutron diffraction profiles of the sample and the empty holder.

other one is for the empty holder only. It is clear that the broad peak is from the sample only.

b) $\text{Ba}_2\text{YRuO}_6 + 5\text{wt\% Y123}$

As discussed above, the superconductor Y123 undergoes complete decomposition at 1270°C into Y_2O_3 , CuO , and BaCuO_2 . A sample with a mixture of undoped Ba_2YRuO_6 (O6) with 5% by weight of superconductor $\text{YBa}_2\text{Cu}_3\text{O}_7$ (Y123) was prepared to test the stability of Y123 with O6 at the heat treatment temperatures used to prepare the Cu-doped Ba_2YRuO_6 superconductor. Neutron diffraction studies were used to identify the presence of Y123 and its possible decomposition products: Y_2O_3 , CuO , and BaCuO_2 .

Fig. 5.5 shows the neutron diffraction profiles of the mixed sample at different heat treatment steps. The y scale is enlarged in order to see the small Y123 peaks clearly, and the profiles are normalized with the highest intensity peak so that we can follow the intensity change of the Y123 peaks. Fig. 5.5a shows the neutron diffraction profile of the mixed sample before the heat treatment. The peaks indicated by the arrows are the peaks of the Y123 phase, and the presence of Y123 is confirmed. The result of the refinement shows that there is about 4.57(20)% Y123 by weight, which is close to the nominal 5%. After the sample is sintered at 900°C , the intensity of the Y123 peaks decreases and the refinement gives a 2.89(31)% Y123 by weight. The amount of Y123 decreases even though the sintering temperature is below the first Y123 decomposition temperature. After the sample is sintered at 1450°C in the Ar/O_2 mixture, the Y123 peaks are almost gone and the refined concentration of Y123 is about 1.28(30)% by weight according to the refinement. There are two peaks at about 44° and 63.5° which appear after the heat treatments. The obvious decomposition products of Y123, Y_2O_3 , CuO , and BaCuO_2 are

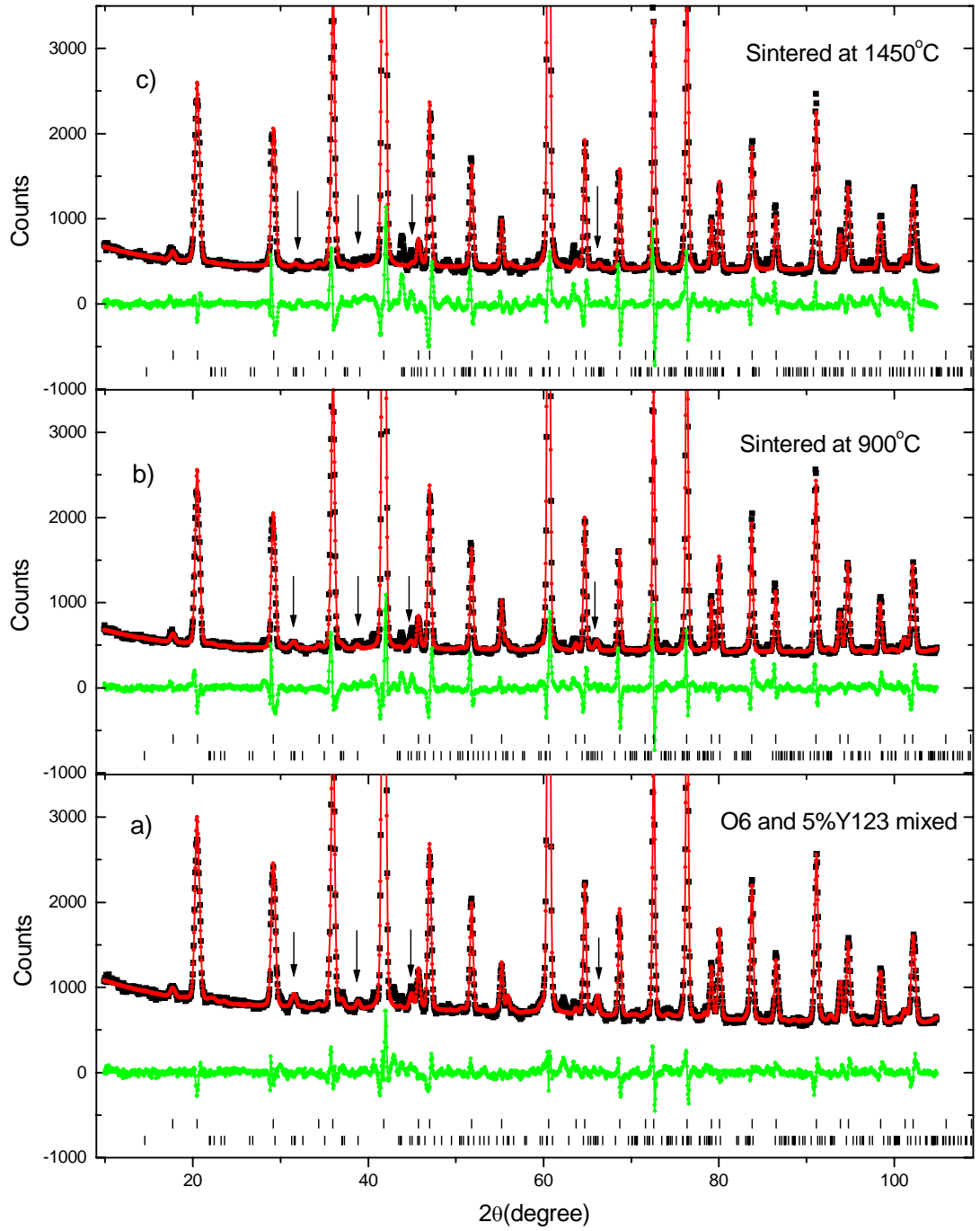


Figure 5.5: The neutron diffraction profiles of the mixture of Ba_2YRuO_6 and 5% by weight of Y123 at different heat treatment steps.

not found to fit these two peaks. The amount of Y_2O_3 , CuO , and BaCuO_2 should be 0.85%, 0.6%, and 3.5% by weight if all the Y123 decomposed, and the amount of BaCuO_2 is large enough to be easily found by neutron diffraction. The magnetization data of the sample after sintering at 1450°C in the Ar/O_2 mixture are similar to that of Cu-doped Ba_2YRuO_6 ; that is, the sample shows superconductivity at 84K. This is a pronounced decrease from the 92K onset temperature of Y123 seen in the mixed sample. Efforts to synthesize Ba_2YRuO_6 mixed with Y123 lead to the incorporation of most of the dopant atoms into the O_6 host.

5.4 CONCLUSIONS

The crystal structure of Cu-doped Ba_2YRuO_6 is a 1:1 B site ordered double perovskite cubic structure with space group $\text{Fm}\bar{3}\text{m}$. Long range antiferromagnetic ordering of the Ru sublattice with a Type I magnetic structure appears when the temperature is below 38K. Above 38K, incommensurate antiferromagnetic ordering of Cu appears. This disappears when the temperature is above 85K, the same temperature as the superconducting ordering. The incommensurate peak is not observed in the undoped Ba_2YRuO_6 . The decomposition of Cu-doped Ba_2YRuO_6 into the undoped Ba_2YRuO_6 and Y123 superconductor is not seen, and efforts to synthesize Ba_2YRuO_6 mixed with Y123 lead to the formation of additional Ba_2YRuO_6 phase with Cu as a dopant.

Chapter 6 SUMMARY

The solid oxide fuel cell (SOFC) is a fuel cell using solid oxides, such as YSZ and CGO, as its electrolyte. It can convert chemical energy into electrical energy directly without combustion. The SOFCs can operate successfully in the 900-1000 °C range with pipeline natural gas to generate kilowatts of power. Recent research interest is focused on SOFCs operated at the intermediate temperature (IT) range (600-800 °C). In this temperature range, the metal alloys, such as stainless steel, can be used as interconnects, reducing the cost of SOFCs greatly.

According to the principle of the SOFC, the cathode should meet the following requirements: 1) a mixed electrical and oxygen ion conductor, 2) chemically stable in an oxidizing environment, 3) chemically compatible with the electrolyte and 4) a similar thermal expansion coefficient as the electrolyte to avoid separation or cracking. ABO_3 perovskites are good candidates for the cathode of SOFCs. The ideal structure of the perovskite is cubic with space group $\text{Pm}\bar{3}\text{m}$. The large cation A, which can be an alkali, alkali earth, or rare earth ion, occupies the A site, and the small cation B, which is a transition metal ion, occupies the B site. Since the two sites are very different in size, the occupancies of these two sites are determined primarily by ionic size rather than valency. Thus, it is possible to substitute selectively for either the A or B ion by introducing other cations with the same or different valency, but similar size. This gives us a chance to alter the properties of a given oxide.

Table 6.1: The properties of perovskite candidates used in SOFCs. σ is the conductivity, δ is the oxygen vacancy concentration, and TEC is the thermal expansion coefficient.

	$\sigma(\text{Scm}^{-1})$ /Temperature	Temp. ($\delta > 0$)	TEC ($10^{-6}/^{\circ}\text{C}$)	Stability in air	reaction with eletrolyte	
					YSZ	CGO
L6SF	$\sim 100/750^{\circ}\text{C}^{(31)}$	655°C	12.5	$>1500^{\circ}\text{C}$	slight ⁽¹¹⁾	None ⁽³²⁾
L8SF	$\sim 32/750^{\circ}\text{C}^{(31)}$	1000°C	14.9	$>1500^{\circ}\text{C}$	None ⁽³²⁾	None ⁽³²⁾
L6SFC	$\sim 325/550^{\circ}\text{C}^{(33)}$	$600^{\circ}\text{C}^{(33)}$	$15.3^{(33)}$	$>1200^{\circ}\text{C}$	strong ⁽⁵⁹⁾	None ⁽³²⁾
L8SFC	$\sim 175/800^{\circ}\text{C}^{(33)}$	700°C	$15.4^{(33)}$	$>1200^{\circ}\text{C}$	slight ⁽³²⁾	None ⁽³²⁾
$\text{LaFe}_{0.4}\text{Ni}_{0.6}\text{O}_3$	$\sim 580/800^{\circ}\text{C}^{(39)}$	1200°C	$11.4^{(39)}$	$<1300^{\circ}\text{C}$	strong ⁽⁶²⁾	Unknown
LSFT	$\sim 3.2/800^{\circ}\text{C}^{(55)}$	700°C	16.0	$>1500^{\circ}\text{C}$	slight ⁽⁵⁵⁾	Unknown

Table 6.1 shows that the L6SF is a good candidate as the cathode of SOFCs operated in the intermediate temperature range. The substitution of La^{+3} by Sr^{+2} at A sites produces a mixed valence Fe ion state, which results in a high electrical conductivity, and/or large oxygen vacancy concentration, which enhances the oxygen ion conductivity. It is chemically stable in air up to 1500°C since the sample quenched from 1500°C is single phase. At high temperature with air flowing, L6SF will absorb oxygen at $303\text{-}655^{\circ}\text{C}$ and then lose oxygen when the temperature is above 655°C . The reactivity between CGO and L6SF is not detectable when the temperature is below 1200°C , and its TEC is $12.5 \times 10^{-6}/^{\circ}\text{C}$, which is close to the TEC of CGO.

L6SFC and L8SFC are other candidates for the cathode of SOFCs operated in the intermediate temperature range. 20 atm % substitution of Fe by Co can increase the electronic conductivity and oxygen vacancy concentration at the intermediate temperature range. These are chemically stable in air up to 1200°C . Unfortunately, their TECs are high and they can react with the YSZ electrolyte. A CGO layer is needed

between the L6SFC cathode and the YSZ electrolyte in order to reduce the reaction between them. L6SFC can be used as cathode of the SOFCs using CGO as its electrolyte, since it can produce oxygen vacancies around 600°C. There is no reaction between L6SFC and CGO at high temperature.

$\text{LaNi}_{0.6}\text{Fe}_{0.4}\text{O}_3$ has high electronic conductivity of 580 Scm^{-1} at 800°C,⁽³⁹⁾ which is more than 3 times higher than that of LSM (180 Scm^{-1}). The average TEC of $\text{LaNi}_{0.6}\text{Fe}_{0.4}\text{O}_3$ from 300-1000°C is $11.4 \times 10^{-6}/^\circ\text{C}$, which is closer to the TEC of YSZ than that of LSM, and it is chemically stable in air below 1300 °C. But its oxygen vacancy concentration is low in the intermediate temperature range. Therefore, some substitution of La^{3+} by Sr^{2+} should be introduced to produce oxygen vacancies at an intermediate temperature.

LSFT is chemically stable in air up to 1500 °C, and oxygen vacancies begin to appear when the temperature is above 700 °C. But it has low electronic conductivity, high TEC, and a reaction between LSFT and YSZ since its Sr content is high. It is not suitable for use in SOFCs, but it can potentially be used as an oxygen separation membrane.

Cubic Ba_2YRuO_6 is a magnetically ordered insulating material with Neel temperature of 37-39 K. Hole-doping by partial substitution of Ru by lower valence Cu yields a superconductor, $\text{Ba}_2\text{YRu}_{1-x}\text{Cu}_x\text{O}_6$, with a typical transition temperature around 85K. Our neutron diffraction study shows that the crystal structure of Cu doped Ba_2YRuO_6 has a 1:1 B site ordered double perovskite cubic structure with space group $\text{Fm}\bar{3}\text{m}$. Phase separation of Y123 from Cu doped Ba_2YRuO_6 is not observed, and Cu

doped Ba_2YRuO_6 phase is stable at high temperature. Hence, the observed diamagnetism and vanishing resistivity must be attributed to the Cu doped Ba_2YRuO_6 phase. The disappearance of the Y123 phase in the mixture of Ba_2YRuO_6 and 5% Y123 by weight is seen after the same heat treatment schedule as employed for the synthesis of Cu doped Ba_2YRuO_6 , and the Cu atoms are incorporated into Ba_2YRuO_6 as a dopant. Long range antiferromagnetic ordering of the Ru sublattice, with type I magnetic structure, appears when the temperature is below 38K, and an incommensurate antiferromagnetic ordering of Cu appears above 38K and disappears above 85K, the same temperature as the superconducting ordering.

REFERENCES

1. K. Kamata, T. Nakajima, T. Hayashi, and T. Nakamura, "Nonstoichiometric Behavior and Phase Stability of Rare-Earth Manganites at 1200°C: (1). LaMnO_3 ," *Mater. Res. Bull.*, 13, 49-54 (1978).
2. J. Mizusaki, H. Tagawa, K. Naraya, and T. Sasamoto, "Nonstoichiometry and Thermochemical Stability of the perovskite-Type $\text{La}_{1-x}\text{Sr}_x\text{MnO}_{3-\delta}$," *Solid State Ionics*, 49, 111-18 (1991).
3. J. H. Kuo, H. U. Anderson, and D. M. Sparlin, "Oxidation-Reduction Behavior of Undoped and Sr-Doped LaMnO_3 Nonstoichiometry and defect Structure," *J. Solid State Chem.*, 83, 52-60 (1989).
4. J. H. Kuo, H. U. Anderson, and D. M. Sparlin, "Oxidation-Reduction Behavior of Undoped and Sr-Doped LaMnO_3 : Defect Structure, Electrical Conductivity, and Thermoelectric Power,," *J. Solid State Chem.*, 87, 55-63 (1990).
5. J. B. Goodenough, "Theory of the Role of Covalence in the perovskite-Type Manganites $[\text{La},\text{M}(\text{II})]\text{MnO}_3$," *Phys. Rev.*, 100, 564-73 (1955).
6. S. Srilomsak, D. P. Schilling, H. U. Anderson, "Thermal Expansion Studies on Cathode and Interconnect Oxides"; pp. 129-40 in *Proceedings of the First International Symposium on Solid Oxide Fuel Cells*. Edited by S. C. Singhai. The Electrochemical Society, Pennington, NJ, 1989.
7. A. Hammouche, E. Siebert, and A. Hammou, "Crystallographic, Thermal, and Electrochemical Properties of the System $\text{La}_{1-x}\text{Sr}_x\text{MnO}_3$ for High-Temperature Solid Electrolyte Fuel Cells," *Mater. Res. Bull.*, 24, 367-80 (1989).
8. Reiichi Chiba, Fumikatsu Yoshimura, Yoji Sakurai, "An investigation of $\text{LaNi}_{1-x}\text{Fe}_x\text{O}_3$ as a cathode material for solid oxide fuel cells," *Solid State Ionics*, 124 281-288, (1999).

9. H. Taimatsu, K. Wada, and H. Kaneko, "Mechanism of Reaction between Lanthanum Manganite and Yttria-stabilized Zirconia," *J. Am. Ceram. Soc.*, 75, 401-405 (1992).
10. O. Yamamoto, Y. Takeda, R. Kanno, and T. Kojima, "Stability of Perovskite Oxide Electrode with Stabilized Zirconia"; pp. 242-53 in *Proceedings of the First International Symposium on Solid Oxide Fuel Cells*. Edited by S. C. Singhal. The Electrochemical Society, Pennington, NJ, 1989.
11. O. Yamamoto, Y. Takeda, R. Kanno, and M. Noda, "Perovskite-Type oxides as Oxygen Electrodes for High-Temperature Oxide Fuel Cells," *Solid State Ionics*, 22, 241-46 (1987).
12. Siemens-Westinghouse. Milestones of SOFC Technology.
<http://www.siemenswestinghouse.com/en/fuelcells/history/milestones/index.cfm>
13. US DOE. <http://www.seca.doe.gov>
14. Wu, M. K.; Chen, D. Y.; Chien, F. Z.; Sheen, S. R.; Ling, D. C.; Tai, C. Y.; Tseng, G. Y.; Chen, D. H.; Zhang, F. C. "Anomalous magnetic and superconducting properties in a Ru-based double perovskite," *Z. Phys. B* 102, 37-41 (1997).
15. D. Y. Chen, F. Z. Chien, D. C. Ling, J. L. Tseng, S. R. Sheen, M. J. Wang, and M. K. Wu, "Superconductivity in Ru-based Double Perovskite-The Possible Existence of a New Superconducting Pairing State," *Physica C* 282-287, 73-76 (1997).
16. Howard A. Blackstead, John D. Dow, Paul J. McGinn, and David B. Pulling, "Confirmation of Superconductivity in $\text{Sr}_2\text{YRu}_{1-u}\text{Cu}_u\text{O}_6$," *Journal of Superconductivity: Incorporating Novel Magnetism*, Vol. 13, No. 6, 2000.
17. Blackstead, H. A.; Dow, John D.; Harshman, D. R.; DeMarco, M. J.; Wu, M. K.; Chen, D. Y.; Chien, F. Z.; Pulling, D. B.; Kossler, W. J.; Greer, A. J.; Stronach, C. E.; Koster, E.; Hitti, B.; Haka, M.; Toorongian, S.. "Magnetism and superconductivity in $\text{Sr}_2\text{YRu}_{1-u}\text{Cu}_u\text{O}_6$ and magnetism in $\text{Ba}_2\text{GdRu}_{1-u}\text{Cu}_u\text{O}_6$," *The European Physical Journal B*, 15, 649-656 (2000).
18. Fresia, E. J.; Katz, Lewis; Ward, Roland. "Cation substitution in perovskite-like phases." *Journal of the American Chemical Society* (1959), 81 4783-5.

19. A. M. Glazer. "The Classification of Tilted Octahedra in Perovskites." *Acta Cryst.* B28, 3384-3392 (1972).
20. A. M. Glazer. "Simple Ways of Determining Perovskite Structures," *Acta Cryst.* A31, 756-762 (1975).
21. Anderson, M. T., Greenwood, K. B., Taylor, G. A. & Poeppelmeir, K. R. "B-cation arrangements in double perovskites," *Prog. Solid State Chem.* **22**, 197-233. (1993).
22. Patrick M. Woodward, "Octahedral Tilting in perovskites. I. Geometrical Considerations," *Acta Cryst.* B53, 32-43 (1997).
23. W. R. Grove, *Philos. Mag.*, 14, 127, (1937).
24. E. Baur, and H. Preis, *Z. Elektrochem.*, 43, 727 (1937).
25. J. Koryta, *Principles of Electrochemistry*, Wiley (1993).
26. G. L. Squires, *Introduction to The Theory of Thermal Neutron Scattering*, Cambridge University Press, 1978.
27. G. E. Bacon, *Neutron Diffraction*, Clarendon Press Oxford, 1975.
28. H. M. Rietveld, "Profile refinement method for nuclear and magnetic structures." *J. Appl. Crystallogr.* 2 65-71 (1969).
29. G. Caglioti, A. Paoletti, and F. P. Ricci, "Choice of collimators for a crystal spectrometer for neutron diffraction." *Nucl. Instrum.* 3, 223-228, (1958).
30. W. A. Dollase, "Correction of intensities for preferred orientation in powder diffractometry: application of the March model" *J. Appl. Crystallogr.*, 19, 267-72, (1986).
31. Patrakeevev, M. V.; Bahteeva, J. A.; Mitberg, E. B.; Leonidov, I. A.; Kozhevnikov, V. L.; Poeppelmeier, K. R. "Electron/hole and ion transport in $\text{La}_{1-x}\text{Sr}_x\text{FeO}_{3-\delta}$ " *Journal of Solid State Chemistry* 172(2003) 219-231.

32. Ralph, James M.; Rossignol, Cecile; Kumar, Romesh, "Cathode Materials for Reduced-Temperature SOFCs." *Journal of the Electrochemical Society*, 150 (11) A1518-A1522 (2003).
33. Tai, L.-W.; Nasrallah, M. M.; Anderson, H. U.; Sparlin, D. M.; Sehlin, S. R. "Structure and electrical properties of $\text{La}_{1-x}\text{Sr}_x\text{Co}_{1-y}\text{Fe}_y\text{O}_3$. Part 1. The system $\text{La}_{0.8}\text{Sr}_{0.2}\text{Co}_{1-y}\text{Fe}_y\text{O}_3$ " *Solid State Ionics* 76 259-271, (1995)
34. Sun, L.; Brisard, G., *Fuel Cell and Hydrogen Technologies, Proceedings of the International Symposium on Fuel Cell and Hydrogen Technologies, 1st, Calgary, AB, Canada, Aug. 21-24, (2005), 85-96.*
35. Mizusaki, Junichiro; Sasamoto, Tadashi; Cannon, W. Roger; Bowen, H. Kent., "Electronic conductivity, Seebeck coefficient, and defect structure of lanthanum strontium iron oxide ($\text{La}_{1-x}\text{Sr}_x\text{FeO}_3$) ($x = 0.1, 0.25$)". *Journal of the American Ceramic Society*. Vol. 66, No. 4, 247-252. (1983)
36. Mizusaki, Junichiro; Yoshihiro, Masafumi; Yamauchi, Shigeru; Fueki, Kazuo. *Fac. Eng.*, "Nonstoichiometry and defect structure of the perovskite-type oxides $\text{La}_{1-x}\text{Sr}_x\text{FeO}_{3-\delta}$ " *Journal of Solid State Chemistry*. 58, 257-266. (1985)
37. N. G. Eror and H. U. Anderson, in "Better ceramics through chemistry II", edited by C J. Briuker, D E. Clark, and D R. Ulrich (Materials Research Society, 1986). Pp571-577.
38. Yang, J. B.; Yelon, W. B.; James, W. J.; Chu, Z.; Kornecki, M.; Xie, Y. X.; Zhou, X. D.; Anderson, H. U.; Joshi, Amish G.; Malik, S. K., "Crystal structure, magnetic properties, and Mossbauer studies of $\text{La}_{0.6}\text{Sr}_{0.4}\text{FeO}_{3-\delta}$ prepared by quenching in different atmospheres". *Physical Review*. B66 184415-1-184415-9. (2002)
39. Chiba, Reiichi; Yoshimura, Fumikatsu; Sakurai, Yoji., "An investigation of $\text{LaNi}_{1-x}\text{Fe}_x\text{O}_3$ as a cathode material for solid oxide fuel cells." *Solid State Ionics*. 124, 281-288. (1999).
40. Simner, S.; Anderson, M.; Bonnett, J.; Stevenson, J., "Enhanced low temperature sintering of (Sr,Cu)-doped lanthanum ferrite SOFC cathodes." *Solid State Ionics* (2004), 175(1-4), 79-81.

41. Chick, L. A.; Pederson, L. R.; Maupin, G. D.; Bates, J. L.; Thomas, L. E.; Exarhos, G. J., "Glycine-nitrate combustion synthesis of oxide ceramic powders". Mater. Lett., 10, 6 (1990).
42. <http://abulafia.mt.ic.ac.uk/shannon/ptable.php>
43. Drennan, J.; Tavares, C. P.; Steele, B. C. H. R. Sch. Mines, Imp. Coll., "An electron microscope investigation of phases in the system lanthanum-nickel-oxygen". Matter. Res. Bull. 17 621 (1982).
44. Barnabe, A.; Gaudon, M.; Bernard, C.; Laberty, C.; Durand, B., "Low temperature synthesis and structural characterization of over-stoichiometric $\text{LaMnO}_{3+\delta}$ perovskites". Materials Research Bulletin 39 (2004) 725-735.
45. G. H. Jonker, "Magnetic compounds with perovskite structure. IV. Conducting and nonconducting compounds". Physica 22 707 (1956).
46. D. B. Currie and M. T. Weller, "Structure of lanthanum copper oxide (LaCuO_3) by powder neutron diffraction". Acta Cryst. (1991). C47, 696-698.
47. Falcon, H.; Martinez-Lope, M. J.; Alonso, J. A.; Fierro, J. L. G., "Defect $\text{LaCuO}_{3-\delta}$ ($\delta=0.05-0.45$) perovskites. Bulk and surface structures and their relevance in CO oxidation". Applied Catalysis B: Environmental 26 (2002) 131-142.
48. Van Berkel, F. P. F.; Christie, G. M.; van Heuveln, F. H.; Huijsmans, J. P. P., "Electrolytes for low temperature solid oxide fuel cells". Proc. 4th Int. Symp. SOFC's, Vol. 95-1, The Electrochem. Soc., 1995, P1062.
49. Sahibzada, M.; Steele, B. C. H.; Zheng, K.; Rudkin, R. A.; Metcalfe, I. S., "Development of solid oxide fuel cells based on a $\text{Ce}(\text{Gd})\text{O}_{2-x}$ electrolyte film for intermediate temperature operation". Catalysis Today (1997), 38(4), 459-466.
50. Steele, B. C. H.; Zheng, K.; Rudkin, R. A.; Kiratzis, N.; Christie, M., "Properties and applications of $\text{Ce}(\text{Gd})\text{O}_{2-x}$ electrolytes in the temperature range 500-700°C". Proceedings - Electrochemical Society (1995), 95-1(Solid Oxide Fuel Cells (SOFC-IV)), 1028-38.

51. Tai, L.-W.; Nasrallah, M. M.; Anderson, H. U.; Sparlin, D. M.; Sehlin, S. R., "Structure and electrical properties of $\text{La}_{1-x}\text{Sr}_x\text{Co}_{1-y}\text{Fe}_y\text{O}_3$. Part 2. The system $\text{La}_{1-x}\text{Sr}_x\text{Co}_{0.2}\text{Fe}_{0.8}\text{O}_3$ ". *Solid State Ionics* 76 (1995) 273.
52. B. C. H. Steele, "Interfacial reactions associated with ceramic ion transport membranes". *Solid State Ionics*, 75 (1995) 157.
53. G. Ch. Kostogloudis, and Ch. Ftilcos. "Properties of A-site-deficient $\text{La}_{0.6}\text{Sr}_{0.4}\text{Co}_{0.2}\text{Fe}_{0.8}\text{O}_{3-\delta}$ -based perovskite oxides". *Solid State Ionics*. 126 (1999) 143-151.
54. Craciun, R.; Park, S.; Gorte, R. J.; Vohs, J. M.; Wang, C.; Worrell, W. L., "A novel method for preparing anode cermets for solid oxide fuel cells". *Journal of the Electrochemical Society* (1999), 146(11), 4019-4022.
55. Kim, H.; Lu, C.; Worrell, W. L.; Vohs, J. M.; Gorte, R. J., "Cu-Ni cermet anodes for direct oxidation of methane in solid-oxide fuel cells". *Journal of the Electrochemical Society*, 149 (3) A247-A250 (2002).
56. Fagg, D. P.; Waerenborgh, J. C.; Kharton, V. V.; Frade, J. R., "Redox behavior and transport properties of $\text{La}_{0.5-x}\text{Sr}_{0.5-x}\text{Fe}_{0.4}\text{Ti}_{0.6}\text{O}_{3-d}$ ($0 < x < 0.1$) validated by Mossbauer spectroscopy". *Solid State Ionics* 146 (2002) 87-93.
57. Fagg, D. P.; Kharton, V. V.; Frade, J. R.; Ferreira, A. A. L., "Stability and mixed ionic-electronic conductivity of $(\text{Sr},\text{La})(\text{Ti},\text{Fe})\text{O}_{3-d}$ perovskites". *Solid State Ionics* 156 (2003) 45-57.
58. Galstyan, Eduard; Xue, Yuyi; Iliev, Milko; Sun, Yanyi; Chu, Ching-Wu, "Origin of the superconductivity in the Y-Sr-Ru-O and Y-Sr-Cu-O systems". *Physics Review B: Condensed Matter and Materials Physics* (2007), 76(1), 014501/1-014501/5.
59. Kindermann, L.; Das, D.; Nickel, H.; Hilpert, K., "Chemical compatibility of the LaFeO_3 base perovskites $(\text{La}_{0.6}\text{Sr}_{0.4})_z\text{Fe}_{0.8}\text{M}_{0.2}\text{O}_{3-d}$ ($z = 1, 0.9$; $\text{M} = \text{Cr}, \text{Mn}, \text{Co}, \text{Ni}$) with yttria stabilized zirconia". *Solid State Ionics* (1996), 89(3,4), 215-220.
60. M. Nakamura, Y. Yamada, and Y. Shiohara, "Crystal growth of $\text{YBa}_2\text{Cu}_3\text{O}_{7-x}$ by the SRL-CP method under low oxygen partial pressure atmosphere". *J. Mater. Res.* 9, 1946 (1994).

61. Parkinson, Neil G.; Hatton, Peter D.; Howard, Judith A. K.; Ritter, Clemens; Chien, Fan Z.; Wu, Maw-Kuen, "Crystal and magnetic structures of $A_2YRu_{1-x}Cu_xO_6$ with $A = Sr, Ba$ and $x = 0.05$ to 0.15 ". *Journal of Materials Chemistry*. 13 (2003) 1468-1474.
62. Blackstead, H. A.; Yelon, W. B.; Kornecki, M.; Smylie, M. P.; McGinn, P. J.; Yang, J. B.; James, W. J.; Cai, Q., "The decomposition of $YBa_2Cu_3O_{7-d}$ doped into Ba_2YRuO_6 ". *Journal of Applied Physics* 103 (2008) 033904.

VITA

Qingsheng Cai was born November, 1966 at Tonggu city, Jiangxi, China. He attended college and received his B.S. in Physics from Tsinghua University, Beijing, China. After two years work as a Research Assistant at the Department of Automation, Tsinghua University, he continued his graduate study at Physics Department, Tsinghua University, and received his M.S. in Physics in 1994. He was employed as an Assistant professor at the Institute of Nuclear Energy Technology, Tsinghua University. His work was focus on Neutron Radiography, γ -pinhole camera, and physical design of a neutron beam with MCNP program for the realization of Born Neutron Capture Therapy (BNCT) in Tsinghua University shielding experimental reactor. He then went to University of Missouri-Columbia to pursue his Ph.D. in Physics. He is married to Li Liu, and has a sweet daughter, Rebecca.